

Ministry of Higher Education & Scientific Research
Ninevah University
College of Electronics Engineering
Communication Engineering Department



Investigation of the Performance Improvement of the Optical Wireless Connection

By

Roua Muwafaq Younus

M.Sc. Dissertation

In

Communication Engineering

Supervised by

Asst. Prof. Dr. Mahmod. A. Al_Zubaidy

Dr. Safwan Hafeedh Younus

2022 A.D.

1444 A.H.

Ministry of Higher Education & Scientific Research
Ninevah University
College of Electronics Engineering
Communication Engineering Department



Investigation of the Performance Improvement of the Optical Wireless Connection

A Dissertation Submitted by

Roua Muwafaq Younus

To

The Council of College of Electronic Engineering

University of Ninevah

In Partial Fulfillment of the Requirements

For the Degree of Master of Sciences

In

Communication Engineering

Supervised by

Asst. Prof. Dr. Mahmud. A. Al_Zubaidy

Dr. Safwan Hafeedh Younus

2022 A.C.

1444 A.H

ABSTRACT

Due to the development of modern technologies and applications that require high data transmission, the need has arisen to move to the high-frequency spectrum like optical wireless communication (OWC). The OWC provides various benefits, such as limitless and unlicensed bandwidth. But the OWC systems have several drawbacks, such as background noise and multi-path propagation that cause the pulse to spread and cause inter-symbol interference (ISI), all of which lead to a decline in the system's performance.

This dissertation proposed two systems to address these issues and create an efficient indoor wireless system. To lessen the effects of multi-path propagation and ambient noise, the first proposed system alters the field of view (FOV) of the single detector. This is investigated by writing a code in the MATLAB program. The effects of each adjustment containing 100 random receiver (RX) locations were displayed. A cumulative distribution function (CDF) was utilized to show how well the suggested system works. As the FOV is reduced, the impact of ISI decreases by decreasing the delay-spread from 2.297 ns for $\text{FOV} = 90^\circ$, which covers 60% of the entire locations, to reaching 0.637 ns when the FOV is set to 10° . Signal to noise ratio (S/N) is improved and equal to 4.91 decibels (dB) for a FOV of 90° , covering 80% of the total locations, and 16 dB for a FOV of 10° .

The second method, however, uses a multi-detector angle diversity receiver (ADR) to lessen the impact of ambient noise. S/N rises as a result, going from -9.4 dB for a conventional diffuse system (CDS) to 3.677 dB when ADR is utilized. Elevation angle optimization is performed, and a narrow FOV is also used for more improvement in the system performance. Also, 232 MHz is the 3-dB channel bandwidth that can be reached. Making adjustments in the code of a single detector to be more suitable for the second

proposed system and adding some of the complexity to the system architecture comes at the sacrifice for improving system performance.

TABLE OF CONTENTS

Subject		Page
ABSTRACT		I
TABLE OF CONTENTS		III
LIST OF FIGURES		VIII
LIST OF TABLES		XIII
LIST OF ABBREVIATIONS		XIV
LIST OF SYMBOLS		XVIII
CHAPTER ONE- INTRODUCTION		
1.1	Background of Optical Wireless Communication	1
1.2	Literature Review	2
1.3	The Scope and Main Contributions	10
1.4	The Dissertation Roadmap	10
CHAPTER TWO -THEORY OF OWC SYSTEMS		
2.1	Introduction	12
2.2	Fundamentals of OWC System	12
2.3	Comparison Between OWC and RF	13
2.4	Classification of OWC System	15

2.4.1	Outdoor OWC System	16
2.4.2	Indoor OWC System	16
2.5	IR Communication System	18
2.6	Indoor OWC System Components	19
2.6.1	Transmitter	20
2.6.2	Receiver	21
2.7	Modulation	25
2.7.1	On-Off Keying Modulation	26
2.7.2	IM/DD Channel	27
2.8	Challenges of Indoor Links	28
2.8.1	Multi-path Characteristics of the Channel for Diffused Radiation	29
2.8.2	Optical Eye Safety Requirements	30
2.8.3	Photodetector High Capacitance	30
2.8.4	Interference from Ambient Light Sources	31
2.9	Angle Diversity Receiver	32
2.10	Model for Multi-path Propagation	33
2.10.1	Calculation of Received Optical Power Using Ray Tracing	35

2.11	Impulse Response	40
2.12	R.M.S Delay-spread	41
2.13	Ambient Light Calculations	42
2.14	S/N and BER Calculations	44
2.15	Path Loss and Channel Bandwidth	45
2.16	Calculation of the (Received Power, 3dB Channel Bandwidth, and S/N) for ADR	46
CHAPTER THREE- CHANNEL MODELING OF AN INDOOR OWC SYSTEM (SINGLE DETECTOR)		
3.1	Introduction	50
3.2	The Outcomes of the Validation Simulation	50
3.3	The Model of the Proposed OWC Single Detector System	53
3.4	Matlab Simulation Flowcharts of the Single Detector Model	55
3.4.1	Calculation of Total Received Power	56
3.4.2	Flowcharts for Calculate delay-spread and Path Loss	65
3.4.3	Flowchart for Calculating Channel Bandwidth	67
3.4.4	Calculation of Noise Power	68
3.4.5	S/N and BER Calculation Flowcharts	75

3.5	Results of the Proposed System	78
3.5.1	Impulse Response	78
3.5.2	R.M.S Delay-Spread	80
3.5.3	S/N Analysis	81
3.5.4	Bit Error Rate	82
3.5.5	Channel Bandwidth and Path Loss	83
CHAPTER FOUR - ANGLE DIVERSITY RECEIVER (MULTI DETECTORS) FOR INDOOR OWC SYSTEM		
4.1	Introduction	85
4.2	The Proposed System Configuration	85
4.3	Calculations in ADR	88
4.3.1	Flowcharts for Calculating Impulse Response	88
4.3.2	Flowcharts for delay-spread and Path Loss Calculation	90
4.3.3	Flowchart for Calculating 3-dB Channel Bandwidth	92
4.3.4	Flowcharts for S/N and BER Calculation	94
4.4	Simulation Results and Discussion	96
4.4.1	Impulse Response	97
4.4.2	R.M.S Delay-Spread	99
4.4.3	S/N Performance Analysis	101

4.4.4	Bit Error Rate	103
4.4.5	Path Loss	105
4.4.6	3-dB Channel Bandwidth	107
4.5	Comparison With Previous Works	108
CHAPTER FIVE - CONCLUSIONS AND FUTURE WORK		
5.1	Research Work's Conclusions	110
5.2	Areas of Further Investigation	111
REFERENCES		112

LIST OF FIGURES

Figure	Title	Page
CHAPTER ONE – INTRODUCTION		
1.1	Part of electromagnetic spectrum show optical spectrum.	2
CHAPTER TWO – THEORY OF OWC SYSTEMS		
2.1	The frequency and wavelength ranges for each band are displayed on a portion of the electromagnetic spectrum.	14
2.2	Classification of OWC systems.	17
2.3	Block diagram of OWC system.	20
2.4	Types of concentrator: (a) A hemispherical concentrator with long pass filter; (b) A hemispherical concentrator with a band-pass filter; and (c) A compound parabolic concentrator.	22
2.5	Types of preamplifiers: (a) High-impedance and low-impedance preamplifiers; and (b) Trans-impedance amplifier.	25
2.6	OWC system's IM/DD channel block diagram.	28
2.7	Noise sources' spectral power densities, both natural and artificial.	32
2.8	Ray tracing for first and second-order reflection for diffuse design.	36

2.9	Ray tracing for first-order reflection.	38
2.10	Ray tracing for second-order reflection.	40
2.11	Ray tracing of lamps' direct path, first and second order reflections.	44
2.12	Angle of receiving analysis for angle diversity.	47
CHAPTER THREE – CHANNEL MODELING OF AN INDOOR OWC SYSTEM (SINGLE DETECTOR)		
3.1	Distribution of lamps for room dimension (5m, 5m, 3m).	55
3.2	Flowchart of calculating first and second order reflection received power and produce impulse response.	56
3.3	Flowchart of calculating first-order reflection received power from the ceiling.	58
3.4	Flowchart of calculating first-order reflection received power from the first wall.	59
3.5	Flowchart of second order reflection (first reflection from the ceiling and second reflection from the four wall).	62
3.6	Flowchart of second order reflection (first reflection from the first wall and second reflection from the three walls and ceiling).	64
3.7	Flowchart for calculating the delay-spread .	65
3.8	Flowchart for calculating path loss.	66

3.9	Flowchart for calculating channel bandwidth.	67
3.10	Flowchart for calculating direct path noise power.	69
3.11	Flowchart to calculate the noise power of the first reflection from the first wall.	71
3.12	Flowchart to calculate the noise power of the first reflection from the first wall and second reflection from ceiling.	74
3.13	Flowchart of the S/N.	76
3.14	Flowchart of the BER.	77
3.15	(a) Impulse response when the TX and RX positioned in the middle of the room; (b) Zooming of the impulse response of (a).	79
3.16	(a) Impulse response when the TX positioned in the middle of the room and RX placed in the corner; (b) Zooming of the impulse response of (a).	79
3.17	CDF of the delay-spread .	80
3.18	CDF of the S/N.	82
3.19	CDF of the BER.	83
3.20	CDF of the channel bandwidth.	83
3.21	CDF of the path loss.	84

CHAPTER FOUR - ANGLE DIVERSITY RECEIVER (MULTI DETECTOR) FOR INDOOR OWC SYSTEM		
4.1	Dimension of the modelled room.	86
4.2	Structure of the angle diversity receiver.	87
4.3	Flowchart for calculating the impulse response.	89
4.4	Delay-spread flowchart.	90
4.5	Flowchart for calculating path loss.	91
4.6	Flowchart for calculating 3-dB bandwidth.	93
4.7	Flowchart for calculating S/N.	95
4.8	Flowchart for calculating BER.	96
4.9	Impulse response when the TX in the center of the room and RX in the corner.	97
4.10	Impulse response when the TX and RX in the center of the room.	98
4.11	Comparison of delay-spread between CDS and ADR when the sender is placed at (2.5m,2.5m,1m) and reception is traveling along the x-axis at y=1m.	99
4.12	Comparison of delay-spread between CDS and ADR when the sender is placed at (2.5m,2.5m,1m) and reception is traveling along the x-axis at y=2m.	100

4.13	Comparison of S/N between CDS and ADR when the sender is placed at (2.5m,2.5m,1m) and reception is traveling along the x-axis at y=1m.	102
4.14	Comparison of S/N between CDS and ADR when the sender is placed at (2.5m,2.5m,1m) and reception is traveling along the x-axis at y=2m.	103
4.15	Comparison of path loss between CDS and ADR when the sender is placed at (2.5m,2.5m,1m) and reception traveling along the x-axis at y=1m.	105
4.16	Comparison of path loss between CDS and ADR when the sender is placed at (2.5m,2.5m,1m) and reception traveling along the x-axis at y=2m.	106
4.17	Comparison of 3-dB bandwidth between CDS and ADR when the sender is placed at (2.5m,2.5m,1m) and reception traveling along the x-axis at y=1m.	107
4.18	Comparison of 3-dB bandwidth between CDS and ADR when the sender is placed at (2.5m,2.5m,1m) and reception traveling along the x-axis at y=2m.	108

LIST OF TABLES

Table	Title of Table	Page
CHAPTER TWO – THEORY OF OWC SYSTEMS		
2.1	Comparison between RF and OWC system.	15
CHAPTER THREE – CHANNEL MODELING OF AN INDOOR OWC SYSTEM (SINGLE DETECTOR)		
3.1	Comparison between our validation results and previous works.	51
CHAPTER FOUR- ANGLE DIVERSITY RECEIVER (MULTI DETECTORS) FOR INDOOR OWC SYSTEM		
4.1	BER and S/N for both CDS and ADR when $y=1m$.	104
4.2	BER and S/N for both CDS and ADR when $y=2m$.	104
4.3	Comparison between our work and previous works.	109

LIST OF ABBREVIATIONS

Abbreviation	Name
ADR	Angle diversity receiver
ADT	Angle diversity transmitter
APA	Beam angle and beam power adaptation
APA-LSMT	Beam angle and beam power adaptation, a line-strip multi-beam transmitter
APD	Avalanche photodetector
BDPA	Beam delay and power adaptation
BDPA-LSMT	Beam delay and power adaptation, a line-strip multi-beam transmitter
BER	Bit error rate
BW	Bandwidth
CADR	Conventional angle-diversity receiver
CCI	Co-channel interference
CDF	Cumulative distribution function
CDS	Conventional diffuse system
CHS	Conventional hybrid system
CPC	Compound parabolic concentrator

D.C.	Direct current
dB	Decibel
DD	Direct detection
EGC	Equal gain combining
FCGH	Fast computer generated holograms
FDAPA	Fast delay , angle, and power adaptive
FOV	Field of view
FSO	Free-space optical
GSC	Generalized selection combining
ICI	Inter-cell interference
IEC	International electro-technical commission
IM	Intensity modulation
IM/DD	Intensity modulation/direct detection
IR	Infrared
ISI	Inter-symbol interference
LAN	Local area network
LD	Laser diode
LD-VLC	Laser diode-visible light communication

LED _s	Light-emitting diodes
LOS	Line of sight
LSMT	Line-strip multi-beam transmitter
MRC	Maximum ratio combining
NIR	Near-infrared
N-LOS	Non-line of sight
NOMA	Non-orthogonal multiple access
O.O.K	On-off keying
O.O.K NRZ	On-off keying -non-return-to-zero
O.O.K RZ	On-off keying return-to-zero
OWC	Optical wireless communication
PAR38	Philips PAR 38 economic
PFDR	Pyramidal fly-eye diversity Receiver
PIN	Positive-intrinsic-negative
PN	Positive-negative
PN/PIN	Positive-negative/Positive-intrinsic-negative
R.M.S	Root mean square
receangle	Variable save the inverse value of the received angle in Matlab code

RF	Radiofrequency
RX	Receiver
RYGB	Red-yellow-green-blue
S/N	Signal to noise ratio
SADR	Sectored angle-diversity Receiver
SBC	Select the best combining
SINR	Signal to interference noise ratio
SOR	Self-orienting Receiver
TIA	Trans-impedance amplifier
TX	Transmitter
UV	Ultraviolet
VL	Visible light
VLC	Visible light communication

LIST OF SYMBOLS

Symbol	Name
\hat{n}_{lamp}	Normal of the lamp
\hat{n}_r	Normal of the Receiver
\hat{n}_t	Normal of the Transmitter
\hat{n}_1	Normal of the reflective element 1
\hat{n}_2	Normal of the reflective element 2
A_{eff}^{bare}	Bare effective signal-collection area
ϕ_1	Incident angle with respect to the Transmitter's normal
ϕ_2	The angle between the incident ray from the Transmitter R_1 and the normal of the reflective element 1
μ	Mean delay
$A_{eff}(\delta)$	Effective signal-collection area
A_r	Photodetector area
Az	Azimuth angle
B	Un-modulated carrier amplitude
$Bandwidth_{coh,50\%}$	Channel coherence bandwidth
$BW_{receiver}$	Receiver bandwidth

c	Speed of light
C	Capacitance of the photodetector
C_t	Total input capacitance
dA	Area of the surface element
dA_1	Area of the surface element of first-order reflection
dA_2	Area of the surface element of second-order reflection
dA_j	Area of the surface element of first and second-order reflection
dp_n	Power emitted into a solid-angle element
dp_r	Received power at the detector
D_{spr}	Root mean square delay-spread
d_{thick}	Detector thickness
E	Energy
El	Elevation angle
EP	The distance between the point and the reflective element
ER	The distance between the receiver and the reflecting element
$erfc$	Error function complementary

ε_o	Permittivity of air
ε_r	Permittivity of silicon
f	Frequency
$G_c(\delta)$	The gain of concentrator
H	Total number of the second reflecting element
$H(0)$	Channel DC gain
$H(f)$	Channel frequency response
$H(f_{3-dB})$	3-dB channel bandwidth
$h(t)$	Impulse response
h_b	Planck's constant
h_{psa}	Half-power semi-angle
i	It is a counter in MATLAB code
$I(t)$	Received photocurrent at the output of the detector at a certain location
I_{photo}	Instantaneous photocurrent
k	The total number of detectors in an angle diversity receiver
M	The total number of first and second reflecting surfaces
$m(t)$	Modulating digital signal

n	Mode number that determines the shape of the radiated beam
$n(t)$	Background light noise
N_{con}	Internal refractive index
n_{elem}	Mode number that determines the shape of the radiated beam of reflecting element
n_{elem1}	Mode number for the first reflective element
n_{elem2}	Mode number for the second reflective element
n_{lamp}	Mode number of lamp
$P_{instant}$	Instantaneous optical power
P_{d_noise}	Direct received noise powers from lamps
p_{lamp}	The optical power emitted by the spot light source
PR	The distance between the receiver and a common point
P_{r_noise}	Received noise powers from the reflecting elements
P_{r_noise1}	Received noise powers from the first reflecting elements
P_{r_noise2}	Received noise powers from the second reflecting elements
P_{r1}	The received optical power by the first-order reflection

P_{r2}	The received optical power by the second-order reflection
p_{rj}	Received power for first and second order reflection
p_{rt}	Total received power
P_{s0}	Powers received associated with logic 0
P_{s1}	Power received associated with logic 1
P_{sj}	Power received associated with logic 1 and 0
p_{source}	Average transmitted optical power
P_{t_noise}	Total received noise power
q	Electronic charge
$Q(t)$	O.O.K wave
R	Photodetector responsivity
R_1	Distance between the reflective element 1 and the transmitter
r_1	Location of the first reflection element
R_2	Distance between the receiver and the reflective element 1
r_2	Location of the second reflection element
R_3	Distance between the reflective element 1 and the reflective element 2

R_4	Distance between the receiver and the reflective element 2
R_{dir}	Direct link distance between the receiver and the transmitter
R_f	Feedback resistance
R_l	Load resistor
r_r	Location of the receiver
r_t	Location of the transmitter
S	Total number of the first reflecting element
t	Absolute time
t_{bin}	Time bin
$T_f(\delta)$	Transmission factor of filter
t_j	Time delay associated with received optical power
v	Number of lamp
V	Total number of lamps
w_c	analog carrier radian frequency
x, y, z	Coordinate of the room
x_1, y_1, z_1	Location of the first reflecting element (in MATLAB code)

x_2, y_2, z_2	Location of the second reflecting element (in MATLAB code)
x_E, y_E, z_E	Coordinate of the reflecting element
x_p, y_p, z_p	Coordinate of the point
x_r, y_r, z_r	Coordinate of the receiver
x_t, y_t, z_t	Coordinate of the transmitter
$y(t)$	Received intensity
α_1	The angle between the reflected ray R_3 and the normal of the reflective element 1
α_2	The angle between the incident ray R_3 and the normal of the reflective element 2
β_2	The angle between reflected ray R_4 and the normal of the reflective element 2
β_1	The angle between the reflected ray R_2 and the normal of the reflective element 1
Γ	Reflection coefficient
Γ_1	Reflection coefficient of first surface element
Γ_2	Reflection coefficient of second surface element
δ	The angle between the incident ray and the normal of the receiver

λ	Wavelength
Ψ_c	Concentrator's FOV (semi-angle)
η	Quantum efficiency
σ_{bn}	Background shot noise component
σ_{pr}	Preamplifier shot noise component
σ_{s0}	Shot noise component associated with the received signal logic 0
σ_{s1}	Shot noise component associated with the received signal logic 1
$\chi(t)$	Transmitted instantaneous optical power

CHAPTER ONE

INTRODUCTION

1.1 Background of Optical Wireless Communication

When information is transferred between two devices without the use of a wire or cable, it is known as "wireless communication". Radio Frequency (RF) and optical wireless communication (OWC) are the two transmission methods for wireless communications [1]. Due to the restricted radio spectrum available, traditional radio communication systems suffer from limited channel capacity and transmission rates, while the data rates that customers are requesting continue to grow exponentially [2]. OWC is fast becoming an attractive alternative medium to RF communication and wired optical communication [3].

OWC refers to optical transmission in which guided visible light (VL), infrared (IR), or ultraviolet (UV) spectrum are utilized as propagation medium [4]. The wavelength of IR is 1 mm - 780 nm, VL is 780 nm - 380 nm, and UV is 10 nm - 380 nm, as illustrated in figure (1.1). OWC provides an enormous uncontrolled bandwidth that is orders of magnitude greater than RF and can give data rates that are compatible with optical fiber communications in the IR spectrum [5]. Other benefits of OWC include intrinsic security (since IR radiation cannot pass through walls), immunity from interference from identical systems running in adjacent rooms, and immunity from electromagnetic interference [6].

OWC system has the ability to give several hundreds of Mbps data rate because of its wide range and unlicensed bandwidth [7]. Numerous studies demonstrate that OWC can carry data in indoor systems at speeds of

up to 25 Gb/s [8]–[11] and more than 26 GHz of visible light communication (VLC) channel bandwidths are attained [12]. In IR communication, the channel bandwidth can be reached up to 15GHz and the data rate is 15 Gb/s [13]–[15]. OWC systems do have significant shortcomings, though [16]. Shot noise is brought on by strong ambient lighting [17]. Additionally, eye and skin safety laws place limitations on the maximum permitted optical transmission power. Inter-symbol interference (ISI) occurs as a result of multi-path dispersion on OWC links caused by non-direct line of sight (LOS) systems [18]. This dissertation will attempt to mitigate these problems and enhance system performance by several methods.

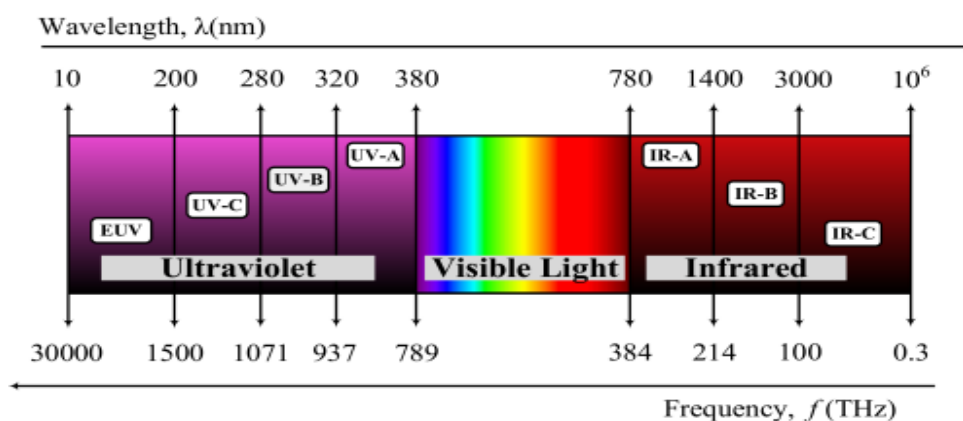


Figure (1.1): Part of electromagnetic spectrum show optical spectrum [3].

1.2 Literature Review

The historical forms of OWC include signaling using smoke, beacon fires, torches, and sunlight. The Ancient Greeks and Romans were credited with being the first to employ light for communication, utilizing their polished shields to reflect sunlight to convey simple messages during fights [19]. Heliographs were usually utilized for military communication in the late 19th century. These systems use a pair of mirrors to focus a controlled beam of light usually sunlight during the day and another bright source, like

a kerosene flame at night, to a station located a distance away. Alexander Graham Bell carried out the first experiment involving the transmission of a signal through the atmosphere in 1880 [20], where solar beams were used to carry voice data over a distance of 200 meters [21].

In the following paragraphs, many previous works are demonstrated.

In (2000), Koorosh Akhavan, Mohsen Kavehrad, and Svetla Jivkova Center, examined the properties of an IR link made up of a multiple-branch receiver with a narrow-field of view (FOV) and a multi-beam transmitter (TX) [22]. In this case, the design objective was to eliminate the impact of ISI in order to use power-efficient signaling techniques like pulse-position modulation at very high data rates. It was demonstrated that bit rates up to a few hundred megabits per second may be accomplished with greater than 99% probability while employing transmitted power levels much below one watt, with an average bit error rate (BER) not exceeding 10^{-9} .

Al-Ghamdi, A. G. and Elmirghani, J. M. H. (2002) [23], [24], explored both pyramidal fly-eye diversity receivers (PFDRs) with varied FOVs and a conventional hybrid system (CHS) with a single detector under various receiver (RX) FOVs. The performance of the CHS was shown to be more significantly impacted by background noise and multi-path dispersion than a PFDR system through FOV adjustment of both the CHS and the PFDR. Additionally, the multi-path dispersion induced pulse spread was greatly reduced, and improved signal to noise ratio (S/N) results were presented to show that the modified PFDR antenna outperforms the CHS.

In 2002 and 2003, Abdullah G. Al-Ghamdi, and Jaafar M. H. Elmirghani, used PFDR with variable FOV to reduce the impact of multi-path propagation and interference from artificial light. Additionally, an evaluation was done on the impact of adjusting the FOV on the effectiveness

of the PFDR in OWC systems. According to simulation data, the performance of such systems was significantly better than that of conventional diffuse systems (CDS), and a significant improvement can be obtained by using PFDR with an optimum FOV. Additionally, the analytical likelihood of error results were provided to show how improved PFDR outperforms CDS [25]–[27].

A. G. Al-Ghamdi and Jaafar M. H. Elmirghani (2004), evaluated and compared the effectiveness of a multi-beam TX indoor optical wireless spot-diffusing system while taking into account the effects of multi-path dispersion and ambient light noise. The results show that employing a line-strip multi-beam transmitter (LSMT) with a three angle diversity receiver (ADR) over the CDS improves S/N. LSMT was explored with single and ADR configurations and was compared with various spot-diffusing methods. According to the findings, using LSMS with a three-direction diversity receiver improves performance by roughly 20 decibel (dB) in terms of S/N compared to a diffuse traditional system, and by 26 dB when combining techniques were employed. The proposed designs' root mean square (R.M.S) delay -spread performance at various places was also assessed and contrasted [28].

A. G. Al-Ghamdi and J. M. H. Elmirghani, again (2004), introduced and evaluated multi-beam TXs in conjunction with ADR. By combining the benefits of both LOS and diffuse OWC links, this arrangement overcomes their disadvantages. The LSMT configuration showed a notable improvement, including a significant decrease in noise power level, a strong received signal because of a reduction in TX-RX separation (since the diffusing spots were now numerous), decreased delay-spread , and an increased S/N (~20 dB) [29]–[31].

Research on TX motion and diversity RXs, as well as how they affect CDS and LSMT system performance, was presented by A. G. Al-Ghamdi and Jaafar M. H. Elmirghani in (2004) [32]. Simulation results demonstrate that by combining an LSMT with 7-ADR under these circumstances, high received signal power can be produced. At the worst communication link when there is ambient noise corruption, LSMT offers S/N gains over the traditional non-directed diffuse system. Additionally, the LSMT and diversity detection response to path loss were evaluated, and it was determined that this response resulted in a path loss reduction of more than 6 dB over the CDS.

In [33], the system's performance was assessed under four different multi-line spot diffusing geometries and compared with that of the CDS and a single line of diffusing spots by J. Alattar and J. Elmirghani in (2005). Background noise and multi-path propagation effects were taken into consideration when analyzing the performance. Through the application of a diversity selection method, a three-branch square-based pyramidal diversity RX was developed to enhance reception. It included an analysis and a comparison of the outcomes for signal delay-spread and S/N.

For a wireless indoor optical channel, the benefit of combining a seven-branch ADR with spot diffusing transmission was demonstrated by Jamal M. Alattar and Jaafar M. H. Elmirghani in (2006) [34]. The effectiveness of the channel was assessed in terms of S/N, and the results were computed and shown for several RX sites. All five spots diffusing geometries have demonstrated higher S/N levels than the scenario when a three-detectors RX was utilized, with an S/N improvement of up to 2 dB.

In (2008), J. M. Alattar and J. M. H. Elmirghani, examined two spots diffusing geometries. These layouts relied on a multi-detectors ADR, together with four multiple beam clusters on the walls and ceiling, to

distribute the optical power transmitted. Based on the computed S/Ns, a transmit power modification strategy was employed to further increase the RX location's S/N. With diversity detection, the performance was assessed for both stationary and mobile TXs, and it was compared to that of the single line strip optical wireless system [35].

In (2010), Jamal M. Alattar and Jaafar M. H. Elmirghani, used multiple seven-segment maximum ratio combining (MRC) ADRs and a power adaptive multi-beam spot-diffusing transmitter [36]. It was anticipated that there would be a feedback link between the transceivers, allowing each RX to broadcast the updated beam transmit power weights to the multi-beam TX in order to get the greatest signal quality at each individual RX location. Consideration was given to two cases involving three and five RXs. The system's performance was assessed in terms of S/N and contrasted with the single RX scenario with and without power adaptation in four distinct placements for the three RX cases in the room.

In (2011), Mohammed T. Alresheedi and Jaafar M.H Elmirghani, an ADR and beam delay and power adaptation, a line-strip multi-beam transmitter arrangement (BDPA-LSMT) was used [37]. The final objective was to boost the received optical power under multi-path dispersion, background noise, and mobility while enhancing S/N. An ADR was used in conjunction with BDPA to cause a considerable decrease in delay-spread from 2.4 ns CDS to roughly 0.11 ns. The simulation outcomes show that the suggested BDPA-LSMT provides a roughly 13 dB S/N gain over an LSMT at a 30 Mbps transmission rate.

Mohammed T. Alresheedi and d Jaafar M.H. Elmirghani, (2011) [38], reduced the degradation caused by ambient light noise, multi-path dispersion, and mobility using beam angle and beam power adaptation in an LSMT configuration (APA-LSMT) in conjunction with ADR. The S/N

results show that ADR and APA can mitigate multi-path dispersion, mobility, and ambient noise impacts. Three techniques: ADR, beam angle, and beam power adaptations were introduced to achieve the improvement. The channel bandwidth was greatly increased from 36 MHz (CDS) to approximately 7.2 GHz by using these techniques.

In (2014), Z. Chen, N. Serafimovski, and H. Haas, investigated the advantages of ADR in an indoor cellular OWC network [39]. According to the findings, the ADR greatly surpasses the single-photodetector RX in terms of both area spectral efficiency and signal to interference noise ratio (SINR). The ADR using the MRC scheme, in particular, performs best, with a SINR improvement of over 40 dB when compared to a single-photodetector RX.

The impact of changing the TX's semi-beam divergence angle on the impulse response, mean delay, and R.M.S delay was examined by Ram Kumar Sharma, Hemani Kausha, and Prabhat Kumar Sharma, in (2015) [40] while maintaining a fixed TX location and power.

Ahmed Taha Hussein and Jaafar M.H. Elmirghani, in (2015), the laser diode-visible light communication (LD-VLC) system's delay-spread was reduced by 91% when an ADR was used with it [41], from 0.65 ns to 0.053 ns. This led to a 32-fold increase in channel bandwidth from 114 MHz to 3.7 GHz. At 5 Gb/s, the ADR LD-VLC system achieves a BER of better than 10^{-6} when employing the on-off keying (O.O.K) modulation format. This allows for complete mobility inside the test zone despite multi-path propagation.

In (2016), J. Ding, C. L. I, and Z. Xu, impact of actual source radiation patterns on channel characteristics, including Nichia and Lumileds Philips light-emitting diodes (LEDs), was thoroughly examined [42]. When compared to the Lambertian pattern, differences in impulse and frequency

responses, spatial distributions of R.M.S delay-spread, and optical path loss, depending on various patterns, were easily discernible from simulation.

B. Mendoza, S. Rodríguez, R. Pérez-Jiménez, A. Ayala, and O. González, in (2016), examined three non-imaging ADRs [43] as input sensors for nodes in an indoor IR wireless sensor network. The RXs under consideration were the self-orienting receiver (SOR), the sectored angle-diversity receiver (SADR), and the conventional angle-diversity receiver (CADR). The major constraints for sensor nodes in an indoor IR wireless sensor network were the least processing capacity and the shortest transmission power needs, and the simulation results demonstrate that employing a CADR in combination with the equal gain combining (EGC) technique produces the best S/N.

In (2016), A. T. Hussein, M. T. Alresheedi, and Jaafar M.H. Elmighani, proposed fast computer-generated holograms (FCGHs) to improve the adaptation process. To lessen the effects of ISI and multi-path dispersion, an ADR and a delay adaptation approach were employed. With VLC channel bandwidths of more than 26 GHz, significant improvements in the S/N were made, resulting in a compact impulse response and a VLC system that could reach higher data speeds with total mobility in what was thought to be a realistic interior environment [12].

In (2017), R. ghahramani Negar Sendani, modeled and investigated how the FOV's RX affected indoor VLC [44]. In VLC, the effect of FOV on the received optical power, the room's distribution of S/N, and BER performance was demonstrated. This outcome can be used by architects for their light systems, RX positions in the space, or airbuses.

According to [45], R. Sharma, M. Aggarwal, and S. Ahuja, in (2018), represented the indoor OWC system by an IR TX with a laser diode (LD)

and a positive-negative/positive-intrinsic-negative (PN/PIN) detector RX. In extremely noisy environments, RX mobility was investigated for a variety of communication parameters. The effects of RX mobility on system variables such as R.M.S delay-spread, S/N, channel capacity, and average BER have been demonstrated.

O. Z. Aletri, M. T. Alresheedi, and J. M. H. Elmirghani (2019), suggested a VLC system using an angle diversity transmitter (ADT) [46]. ADT used two different types of red-yellow-green-blue (RYGB) LDs units: RYGB LDs light units (for lighting and communication) and RYGB LDs light units (for illumination). The delay-spread and S/N were also calculated while a four-branch ADR was employed. The proposed system was examined in comparison to a typical VLC system. The delay-spread and S/N were significantly improved, and it supports operation at large data rates up to 22.8 Gb/s.

A four-branch ADR RX was proposed by M. K. Aljohani *et al.*, (2020) [47] as a means of increasing the data rate of a non-orthogonal multiple access (NOMA) system. The simulation results indicate that, compared to a system with a large-FOV RX, using an ADR improves the NOMA system's data rate by an average of 35%.

M. E. Hosney, H. A. I. Selmy, and K. M. F. Elsayed, (2020), eliminated co-channel interference (CCI) by reducing the FOV of an ADR, which interferes with indoor VLC [48]. In order to achieve low BER for the proposed VLC multiple input multiple output system at various room placements, the FOV and ADR's tilting angles were tuned. The ideal FOV for each ADR's tilting angle was demonstrated through simulation results. Additionally, at the most interfering location and optimal tilting angle of 30°, satisfactory BER was obtained.

M. Román Caizares, P. Palacios Játiva, C. A. Azurdia-Meza, S. Montejo-Sánchez, and S. Céspedes, investigated and compared the applications and benefits of various combining strategies to provide variety at the optical RX in a multi-cell indoor VLC system in (2022) [49]. On the RX side, select the best combining (SBC), EGC, generalized selection combining (GSC), and MRC combining schemes were investigated and put into practice. The findings show that in terms of SINR and user data rate, the ADR applied with the MRC scheme performs better than the SBC, EGC, and GSC schemes. This was because, in the face of inter-cell interference (ICI), MRC weights both the interference and the received signals, enhancing the quality of the combined signal in the ADR.

1.3 The Scope and Main Contributions

The work's main objectives are as follows:

1. To look at the potential of developing indoor OWC systems that handle the limitations imposed by the OWC environment in order to model the appropriate TX and RX configurations.
2. To investigate if altering the FOV angle could improve the received power, S/N, and delay-spread, hence improving system performance.
3. To study how implementing ADR can lessen the effects of background noise to improve system performance.
4. To examine how utilizing ADR might increase the transmission data rate and lower BER.

1.4 The Dissertation Roadmap

In chapter two, a broad overview of OWC systems is presented, along with OWC connection classifications, a comparison of RF and OWC, an IR communication system, an indoor OWC system topology, and the benefits and difficulties of this kind of communication are shown. All the equations

that are needed in the calculation of the first and second proposed systems are displayed.

In Chapter three, the model of the first proposed system and the flowcharts that are needed to calculate the parameters are given. The cumulative distribution function (CDF) results for various FOVs are discussed.

In chapter four, second proposed communications system, which consists of an ADR and diffuse TX, is described. The flowcharts of calculating are displayed. Additionally, a comparison is drawn between the proposed system and the CDS system when the RX is travelling along $x=1$ and 2 m.

Finally, chapter five includes indications of conclusions and potential study topics.

CHAPTER TWO

THEORY OF OWC SYSTEMS

2.1 Introduction

The TX and RX parts, the OWC connection types (indoor and outdoor), and indoor OWC links (LOS, N-LOS, diffuse, and other), were all covered in this chapter. It offered a comparison between RF and OWC media. Background noise, optical safety restrictions, and other design considerations were all covered for indoor OWC systems. The advantages of ADR are presented. The O.O.K modulation method is also covered in this chapter. Finally, the first and second proposed systems' calculation-related equations are all displayed.

2.2 Fundamentals of OWC System

OWCs use three separate electromagnetic spectrum bands: IR, VL, and UV [3]. The wavelength of the electromagnetic waves is decreased by moving to higher optical frequencies [3]. The frequency f , is related to wavelength λ , by [50]:

$$f = c/\lambda \quad (2-1)$$

where c is the speed of light. The wavelength of the light has an inverse relationship with its capacity to enhance mean kinetic energy. The equation below explains how light and energy E are related [51].

$$E = h_b f/\lambda \quad (2-2)$$

where h_b is the Planck constant. For a given exposure time, the potential increase in kinetic energy and temperature are both greater for shorter wavelengths [51]. The optical bands each have particular benefits and

drawbacks. Various wireless technologies are being developed based on these optical wavelengths.

In terms of communication, near-infrared (NIR) and VL display qualitatively similar behavior because to their virtually identical wavelengths. Despite this, IR can be employed in situations where illumination is not required because it is invisible to people. UV can offer NLOS communications over medium and long distances and high-data-rate LOS connectivity over short and long distances [4].

2.3 Comparison Between OWC and RF

Wireless communication has unquestionably become an indispensable tool in our daily lives. RF technologies are used in the majority of existing wireless communication systems to transmit data [52]. The RF band spans the electromagnetic spectrum from 30 kHz to 300 GHz as shown figure (2.1), and its usage is closely regulated by local and international organizations. Sub-bands are usually leased solely to operators, such as cellular phone companies, television broadcasters, and point-to-point microwave lines. The demand for RF spectrum is outstripping availability as the need for data-intensive wireless applications and services grows, resulting in spectrum congestion. The time has come to seriously investigate the higher regions of the electromagnetic spectrum for wireless communications, given the spectrum congestion at both the network access and backhaul levels. By doing so, we enter the optical band, which contains the sub-bands of IR, VL, and UV [19]. OWC is identical to RF wireless, except instead of radio waves, light is used, and antennas are substituted by free-space optical transceivers. Despite this superficial resemblance between OWC and RF links [53], when contrasted to RF systems, OWC systems provide a number of advantages, which include [2] immunity against interference from other RF wireless devices, with limitless and unrestricted bandwidth. OWC linkages allow for

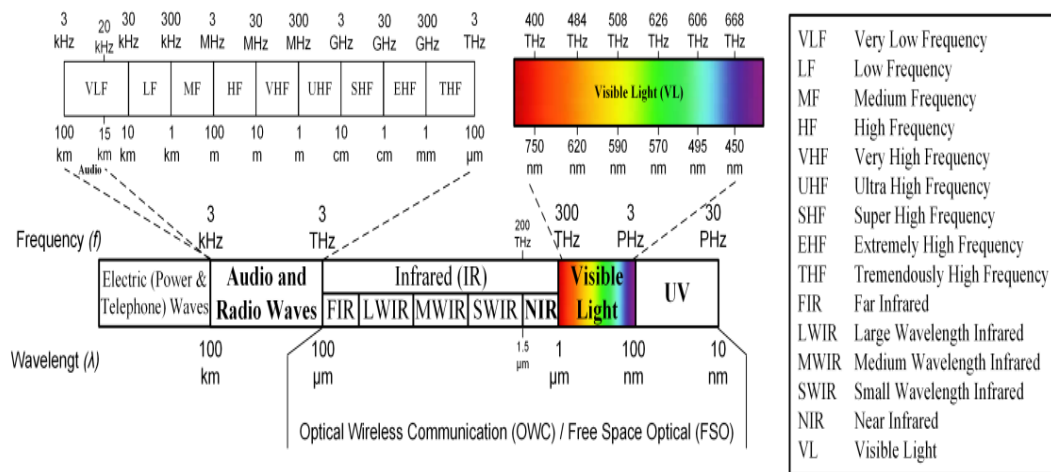


Figure (2.1): The frequency and wavelength ranges for each band are displayed on a portion of the electromagnetic spectrum [60].

frequency reuse in neighboring rooms as well as the utilization of low-cost optoelectronic devices like LEDs and silicon detectors, which are compact and power-efficient [17]. However, shot noise caused by bright ambient light, multi-path dispersion associated with non-direct LOS communication, the need for a backbone network to connect OWC access points in different rooms because optical signals do not pass through walls, and transmission power that is limited by eye and skin safety regulations are all disadvantages of OWC links [54]. Table (2.1) compares RF with OWC [55].

Table (2.1): Comparison between RF and OWC system.

Parameters	Radiofrequency	Optical wireless communication
Licensing	Licensed	Un-licensed
Health-safety	Required	Required for lasers as source
Noise/ Interference	Electromagnetic radiations from other channels, electrical noise	Ambient light
Security	Limited	High
Power consumption (short range)	High	Low
Multi-path fading	Medium	Low
S/N	High	Low
Path loss	Depends on RF signal amplitude	Depends on optical signal power

2.4 Classification of OWC System

Depending on how far apart the TX and RX are, wireless optical transmission can be divided into different categories. As a result, long and short-distance systems, two classes of wireless optical systems, have been recognized. Outdoor wireless optical uses long-distance systems. While short-range communications devices can be used in both outdoor and indoor

settings [1]. In this dissertation, the investigation is limited only to the indoor OWC system.

2.4.1 Outdoor OWC System

There are two types of outdoor OWC: long-range free space links and short-range links [56]. Outdoor OWC, also known as free-space optical (FSO) communications, is a LOS method of transmitting optical signals through the air channel. An FSO system has exceptional directivity and can be used for links over very long distances (more than 20 km), as the laser beam is naturally narrow. Compared to RF devices, FSO devices are more lightweight and energy-efficient. An FSO system might be an alternate solution when an optical fiber system is prohibitively expensive or difficult to install (for example, in mountainous or natural disaster-prone areas) (10–20 km). The last-mile issue (less than 10 km) is likewise thought to be solved by an FSO system [57].

The information signal from the source is modulated on the optical carrier and allowed to propagate toward the RX through the atmospheric channel or free space as opposed to guided optical fibers [20].

The atmospheric attenuation brought on by the absorption, scattering, and shimmer of the optical signals in the atmosphere is one of the major obstacles to deploying outdoor short-range optical wireless networks. Because of the presence of carbon dioxide and water vapor, optical signals are absorbed. When fog, haze, rain, snow, and other obstructions are present, scattering causes some of the light coming from a source to divert away from the intended RX. A number of elements, such as light refraction, atmospheric turbulence, air density, cloud cover, and wind, contribute to shimmer [56].

2.4.2 Indoor OWC System

The amount of directionality of the RX and TX, which is dependent on the source beam-angle and detector FOV [58], as well as the presence of a direct channel between the RX and the TX, are used to characterize OWC connections [2], [59]. Figure (2.2) shows several link categorization algorithms. LOS and non-LOS (N-LOS) are the two most popular connection options for indoor systems. LOS connections offer a direct channel between the TX and the RX, reducing multi-path dispersion and increasing the communication system's power efficiency. LOS linkages, on the other hand, are susceptible to shadowing. In contrast, reflections from surfaces such as the ceiling and walls and other are necessary for N-LOS links. They provide reliable connections and shadow protection, but they are badly harmed by multi-path dispersion, which causes ISI and pulse spread.

Directed, hybrid, and non-directed linkages can be found in both LOS and N-LOS systems. Between the TX and the RX, directed links for LOS

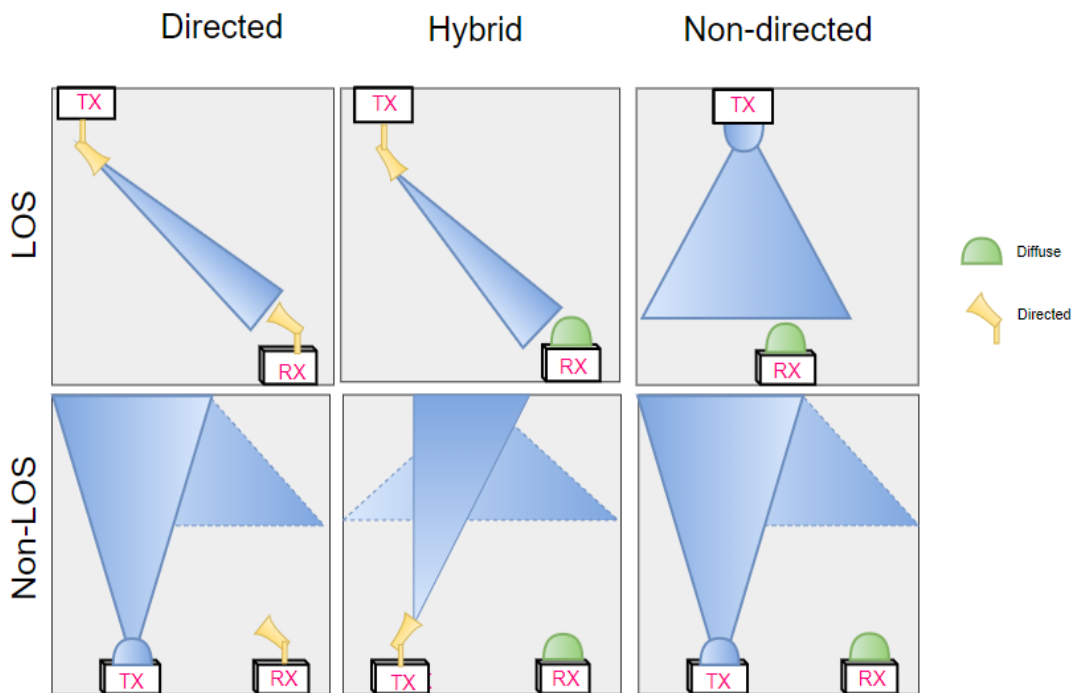


Figure (2.2): Classification of OWC systems [58].

communication use a small radiation pattern as well as a narrow-FOV. This scenario eliminates ambient noise and minimizes path loss while increasing power efficiency. From the standpoint of mobility, the N-LOS non-directed scenario is the most suitable for indoor systems; nevertheless, it suffers from dispersion, which might restrict the possible data throughput, and it is also constrained by the low power gathered [2].

The term "diffuse link," also known as a non-directed/N-LOS link, is used frequently [60]. The CDS is a popular diffuse system. CDS uses a wide-FOV RX and a wide-radiation-pattern TX. The signal received from the TX is reflected multiple times before it reaches the RX while the sender and RX are pointed at the ceiling [2]. The degree of directionality at the TX and RX varies in hybrid links [60]. With a non-directed LOS connection, the TX and detector's FOVs are both sufficiently wide to guarantee coverage of the whole interior space. Unlike directed LOS, these linkages don't need precise alignment or pointing. For a given link distance and transmission power, the received irradiance is decreased in this instance [20].

2.5 IR Communication System

The portion of the electromagnetic spectrum between microwaves and VL is known as IR radiation. The IR area is the wavelength range between approximately 750nm and 1mm. According to its wavelength, the IR region is further classified into three categories: far-IR (1 mm to 10 μm), mid-IR (10 to 2.5 μm), and NIR (2,500 to 750 nm). The radio wave's wavelength is longer than the IR wavelength. However, the wavelengths of IR and VL are close together, and they behave similarly. Both are diffusely reflected from light-colored things, absorbed by dark objects, and directly reflected from glossy surfaces [61].

Because low-cost semiconductor sources (such as lasers or LEDs) are readily available in the NIR range of the spectrum, from 750 to 1000 nm, they are frequently used. Additionally, silicon-based low-cost, high bandwidth, and large area photodetectors which are necessary for reception can operate in this range [62].

Large bandwidths of transmission, as well as resistant to interference from nearby electrical equipment are two additional benefits of IR transmission over RF transmission. Additionally, IR systems are perfect for indoor environments because to their low transmission ranges and high data speeds [63].

Because IR offers various advantages over VL, including high bandwidth, light dimming, and flicker, which is not a problem in IR systems, in addition to the problem of the multi-path dispersion and background noise, as a result IR is utilized in our proposed systems.

2.6 Indoor OWC System Components

An OWC system, like any other wireless communication system, is made up of three parts: a TX circuit, a RX circuit, and the channel that connects them [61]. Figure (2.3) depicts the components of a typical indoor OWC system. A light source, free space as a propagation medium, and a light detector are the components of a simple OWC system. Electronic circuitry modulates the light source and receives information in the form of digital or analog signals. The source output is directed into free space using an optical system (to regulate the radiated radiation, for example, to guarantee that the TX is eye-safe). The received signal travels via an optical system (e.g., an optical filter that rejects optical noise, a lens system or concentrator that concentrates light on the detector), and the resultant photo-current is amplified before reaching the signal processing circuits [64].

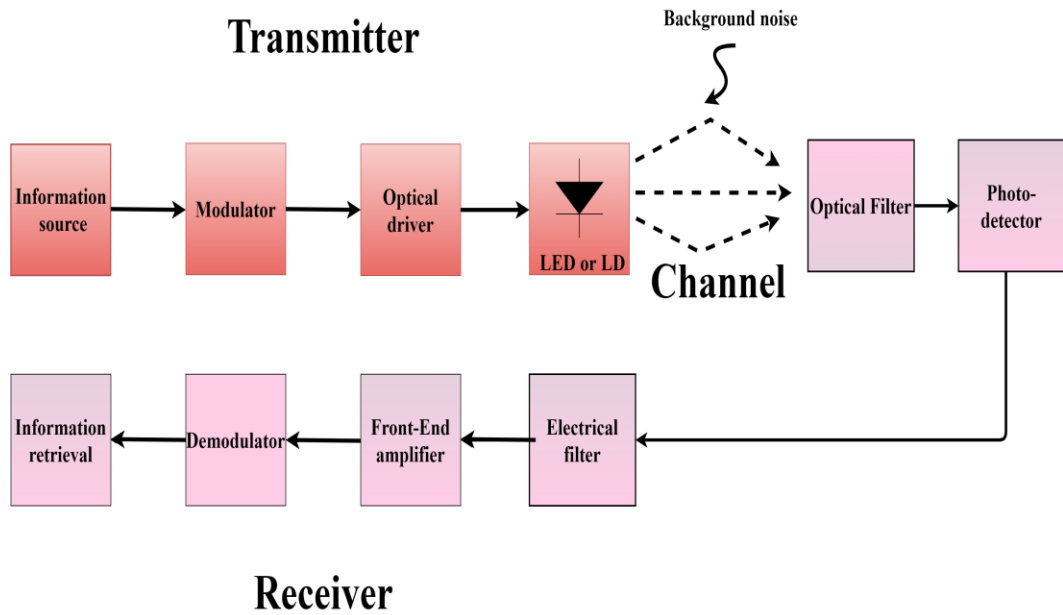


Figure (2.3): Block diagram of OWC system [45].

2.6.1 Transmitter

An electrical signal that has been modulated with the data to be conveyed is applied to a solid-state semiconductor-based source, such as an LD or LED, and the source's intensity is changed in response to the signal. Depending on the electrical driving circuits and demands of the communication's modulation scheme, the electrical to optical transfer function can be either linear or nonlinear [62].

The decision between LEDs and LDs is made depending on the requirements and configuration in which they will be employed [65]. Because they offer greater optical power outputs, larger modulation bandwidths, and linear electrical to optical signal conversion properties, LDs are preferred over LEDs for indoor OWC TXs. When using advanced modulation systems such as multi-subcarrier modulation or multilevel signaling, signal conversion linearity is very critical. However, because of safety concerns (eye safety), LDs cannot be utilized directly in indoor OWC

systems, where radiation can readily penetrate the human eye. LDs are extremely directed radiation sources that may deliver a significant amount of power to a tiny region of the retina, causing lifelong blindness [66]. It must be in some way dispersed in order to be considered eye-safe [67]. LEDs, on the other hand, are large-area emitters that may safely run at greater power. In addition, they are less costly and more dependable. As a result, LEDs are the light source of choice for most indoor applications [66].

2.6.2 Receiver

The RX is made up of an optical concentrator, a detector, and a preamplifier [68]. Filters and compound parabolic concentrators (CPC) can be used before the photodetector to increase signal reception quality [69]. In order to enhance the effective area of the detector, optical wireless RXs usually use an optical concentrator. Optical filtering is also commonly employed to reduce out-of-band background radiation [67].

2.6.2.1 Optical Concentrators:

Path loss may be reduced in OWC systems by utilizing photodetectors with a wide collection area at the RX end. Unfortunately, [70], because of the large capacitance, the RX bandwidth is reduced and the thermal noise is increased. As a result, an optical concentrator should be used to expand the RX's actual gathering area [71]. Concentrators can be non-imaging or imaging. However, non-imaging concentrators are preferred for most indoor applications, figure (2.4) shows the types of concentrators. The non-imaging concentrator hemispherical lens is very critical. When utilizing long-pass filtering, it is possible to place a planar long-pass filter in between the hemisphere and the detector, as shown in figure (2.4a). The band-pass filter is deposited onto the outer surface of the hemispherical concentrator when band-pass filtering is used, as illustrated in figure (2.4b). Another non-

imaging concentrator the CPC as shown in figure (2.4c) is commonly used in IR systems and enhances the collection efficiency of OWC RXs. It has a substantially greater gain than the hemisphere, but at the cost of a restricted FOV [70]. A bare detector, obtains an actual signal-gathering area of

$$A_{eff}^{bare}(\delta) = A_r \cos \delta \text{rect}\left(\frac{\delta}{FOV}\right) \quad , \quad \text{rect}(x) = \begin{cases} 1, & |x| \leq 1 \\ 0, & |x| > 1 \end{cases} \quad (2-3)$$

where FOV is the RX FOV (semi-angle from the surface normal), δ is the incidence angle relative to the RX axis, and A_r is the actual area of the RX.

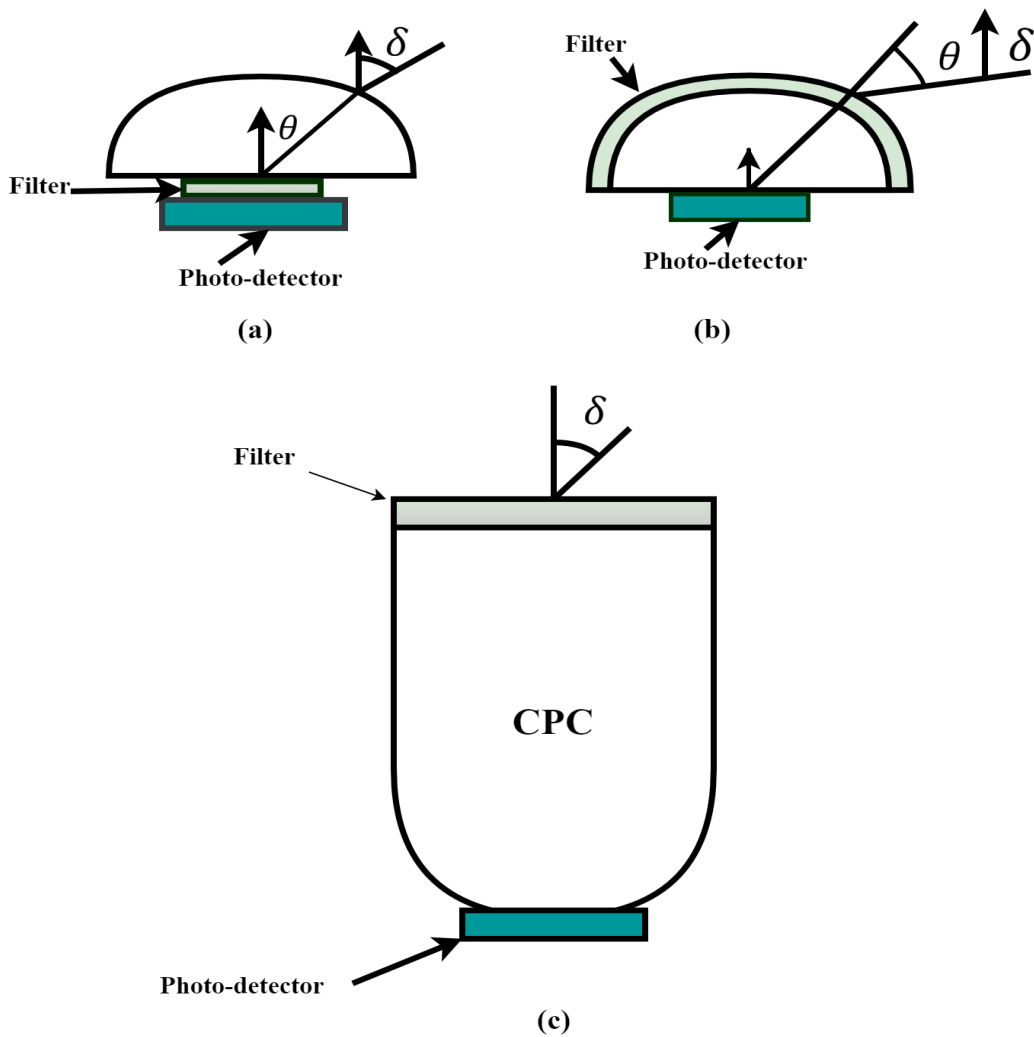


Figure (2.4): Types of concentrator: (a) A hemispherical concentrator with long pass filter; (b) A hemispherical concentrator with a band-pass filter; and (c) A compound parabolic concentrator [70].

The effective signal-collection area grows when a concentrator and filter are added:

$$A_{eff}(\delta) = A_r T_f(\delta) G_c(\delta) \cos \delta \text{ rect} \left(\frac{\delta}{\Psi_c} \right) \quad (2-4)$$

the concentrator gain is $G_c(\delta)$, $T_f(\delta)$ is the transmission filter, and the concentrator FOV is Ψ_c (half-angle) [43], [72]. Non-imaging concentrators usually have a trade-off between gain and FOV [73]. The internal refractive index N_{con} of an idealized non-imaging concentrator, $G_c(\delta)$ is given by [37]:

$$G_c(\delta) = \begin{cases} \frac{N_{con}^2}{\sin^2(\Psi_c)}, & 0 \leq \delta \leq \Psi_c \\ 0 & \delta > \Psi_c \end{cases} \quad (2-5)$$

the acceptable semi-angle for the CPC is $\Psi_c < 90^\circ$ and $N_{con} = 1.7$ [15]. The gain inside the FOV grows when the FOV is reduced, as shown in the above equation. The concentrator's gain approaches zero when the receiving angle is greater than the acceptance semi-angle [37].

2.6.2.2 Detectors

Photodiodes, also known as detectors, perform the optical to electrical conversion. The detectors provide an output photocurrent $I(t)$ that is relative to the amount received intensity $y(t)$ [55]. The positive-intrinsic-negative (PIN) photodiode and the avalanche photodetector (APD) are two possibilities for the detector. APDs employ the avalanche effect to provide low noise gain, making them ideal for applications with less background radiation. The gain of an APD, is actually harmful to performance in OWC systems when shot noise owing to strong ambient light is the major noise source [67]. APDs, on the other hand, are more pricey and have a temperature-dependent gain [60]. As a result, PIN photodiodes are preferred over APDs due to their ability to operate with a low-bias voltage, cheaper cost, and tolerance to large temperature changes [74].

When a photodiode receives an instantaneous optical power ($P_{instant}$), it immediately produces a photocurrent (I_{photo}) can be used to describe the photodiode's fundamental steady-state behavior. It is possible to write the instantaneous photocurrent as [75]:

$$I_{photo} = R P_{instant} \quad (2-6)$$

R stands for photodiode responsivity (A/W). In link modeling, a significant metric is a responsivity, this is an illustration of the optoelectronic transition from the optical to the electrical realm. The following is a model of the responsivity [52]:

$$R = \frac{q\lambda\eta}{h_b c} \quad (2-7)$$

where q is the charge of electron. The likelihood that an incoming photon produces an electron-hole pair is represented by the device's internal quantum efficiency, which is given as η . The normal range of responses for characteristic silicon photodiodes is 0.5-0.75 A/W [75].

2.6.2.3 Preamplifiers

Trans-impedance, high-impedance, and low-impedance preamplifiers are the three types of optical RX preamplifiers as shown in figure (2.5). Depending on whether the load resistor (R_l) is small or big, the preamplifier will be low or high impedance. R_l is selected modest (usually 50 Ω) for a low-impedance RX such that the RX bandwidth $1 / (2\pi \times R_l \times C_t)$ is suitable for the signal bandwidth. C_t denotes the total input capacitance, which includes the photodetector capacitance as well as the amplifier's input capacitance. The disadvantage of this strategy is that it has a lower sensitivity; also, for tiny R_l , the thermal noise associated with R_l might be

rather considerable. The same arrangement is used in a high-impedance RX, but R_i is increased to reduce the effects of thermal noise. The RX bandwidth, on the other hand, is lower than the signal bandwidth, necessitating an equalization step after the preamplifier. However, the RX's dynamic range is lowered during the equalization stage. Because of their broad functioning without considerably sacrificing noise performance, the trans-impedance preamplifier has become quite popular for OWC applications. They also have an excellent dynamic range. A trans-impedance preamplifier with a substantial feedback resistance R_f as shown in figure (2.5b) and an inverting amplifier [70].

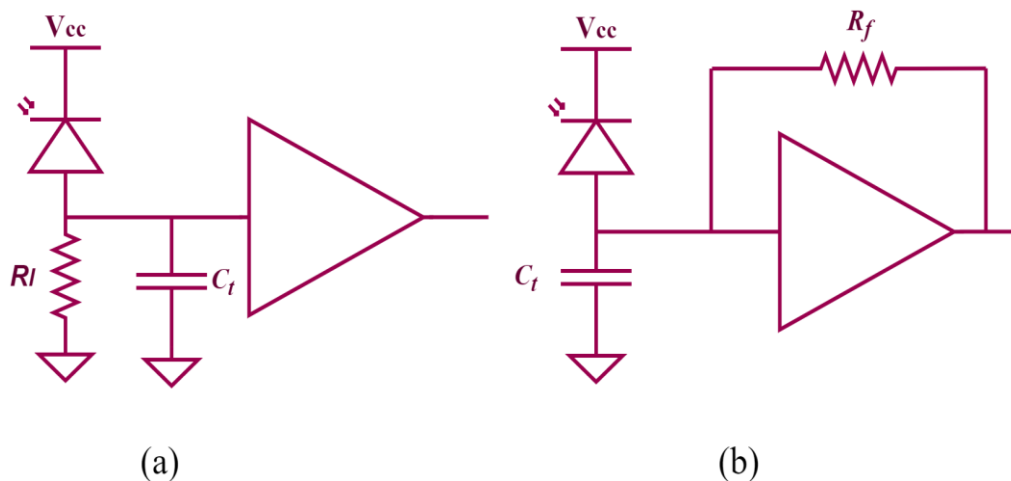


Figure (2.5): Types of preamplifiers: (a) High-impedance and low-impedance preamplifiers; and (b) Trans-impedance amplifier[70].

2.7 Modulation

RX performance at low frequencies, typically below 100 kHz, is dominated by noise and interference from ambient light. Because of this, base-band data transmission is not thought to be sufficient to provide stable signal delivery. Therefore, to alter the spectrum beyond a few hundred hertz, some form of modulation must be used [67]. Where the modulation is a

technique for altering the properties of the wave that will be delivered by placing the message signal over a high frequency signal [76]. There are numerous modulation schemes that are appropriate for OWC systems, each with unique benefits and drawbacks [67].

In OWC systems, the first stage involves encoding the data as a waveform or waveforms, and the second stage involves modulating these waveforms onto the carrier's instantaneous power. The two transmission techniques that are most frequently utilized in OWC systems are intensity modulation (IM) and direct detection (DD) [2]. The best modulation methods for IM/DD in indoor optical wireless systems, such as O.O.K, are analyzed in the next section, along with descriptions of IM/DD channels.

2.7.1 On-Off Keying Modulation

The small modulation bandwidth of light sources is the main obstacle standing in the way of indoor OWC having a high transmission rate. In the indoor OWC system, a variety of modulation methods have been employed. The choice of which to use is determined by the desired application and channel setup [72].

Pulse amplitude modulation with only two levels is known as O.O.K modulation. Due to LDs and LEDs' rapid on/off capabilities, O.O.K is an appropriate OWC modulation technique that is simple to apply in such systems [2]. Bit '1', which may take up all or part of the bit period, is indicated by the presence of an optical pulse. The absence of a pulse, on the other hand, denotes bit '0'. Both situations allow the pulse to fill either the whole bit length, as in the case of O.O.K-non-return-to-zero (O.O.K-NRZ), or only a portion of the bit period, as in the case of O.O.K-return-to-zero (O.O.K-RZ) [77], resulting in improved power usage over O.O.K-NRZ at the cost of a higher bandwidth demand [67].

In O.O.K, a binary information signal directly modifies the amplitude of an analog carrier. O.O.K is mathematically shown as:

$$Q(t) = [1 + m(t)] \times \left[\frac{B}{2} \cos(\omega_c t) \right] \quad (2-8)$$

where $Q(t)$ is O.O.K wave, $m(t)$ is the modulating digital information signal, $B/2$ is un-modulated carrier amplitude, and ω_c is analog carrier radian frequency.

2.7.2 IM/DD Channel

In general, IM/DD is used to create simple and inexpensive optical carrier modulation and demodulation [64]. In IM/DD, the light intensity is modulated as an information-carrying signal, and information is retrieved at the RX side by measuring the received light intensity [78]. That is, only the optical wave's intensity is recognized; neither its frequency nor phase are specified [64]. Depending on how much optical power is incident, the photodetector produces a current [2]. Numerous millions of light signals with extremely short wavelengths are typically present in the usual detector region, allowing spatial diversity and preventing fading [12]. This process results in a real-valued, positive modulating signal (current). This is a key distinction from RF coherent communications, in which the modulated signal has complex-valued modulation. Additionally, due to operational, safety, and lighting considerations, the modulated signal in IM/DD may be peak-constrained and/or average-constrained [78]. Using IM/DD, the channel's impulse response $h(t)$ can be utilized to measure multi-path propagation in an indoor OWC channel [15].

$$I(t) = R x(t) \otimes h(t) + n(t) \quad (2-9)$$

where t is the absolute time, $x(t)$ is the transmitted instantaneous optical power, \otimes denotes convolution, and $I(t)$ is the received photocurrent at a certain location. Lastly, $n(t)$ represents the background light noise as shown

in figure (2.6). In OWC IM/DD, background shot noise can be modeled as Gaussian, white, and is independent of $x(t)$ [15]. In equation (2.9), it's worth noting that $x(t)$ stands for power instead of amplitude. As a result, the signal must be non-negative, and eye safety laws restrict the maximum optical transmission power that can be employed [67].

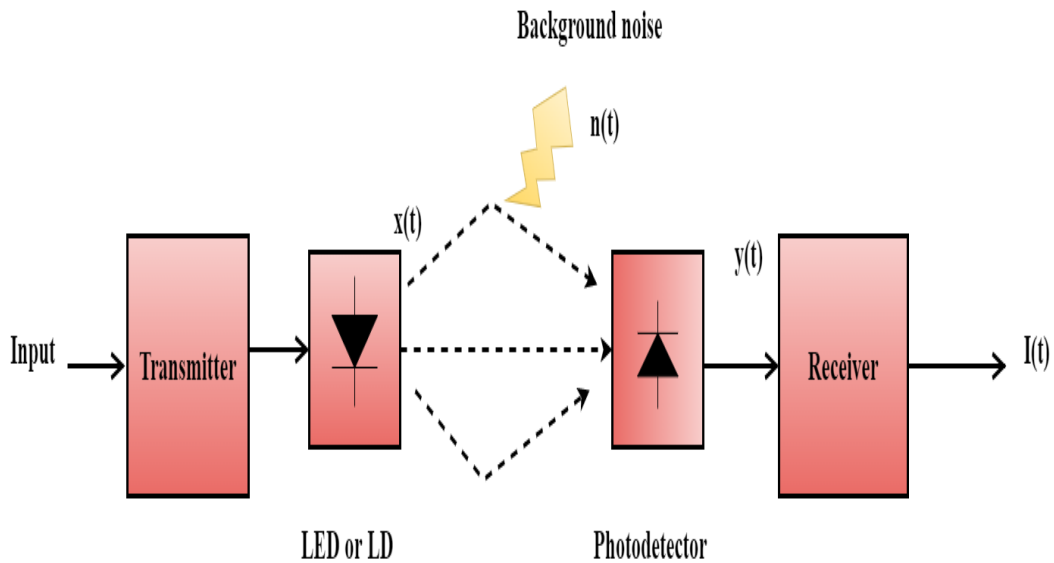


Figure (2.6): OWC system's IM/DD channel block diagram [99].

2.8 Challenges of Indoor Links

Indoor OWC systems, in comparison to outdoor OWC systems, have shorter ranges and are not affected by environmental factors such as fog, rain, snow, or mist. The loss of the indoor link is solely due to a lack of free space. Direct-LOS and diffuse configuration are the two indoor optical wireless transmission strategies. Direct-LOS systems have greater transmission rates and better power efficiency, as well as lower multi-path dispersion and path loss. The disadvantage of this arrangement is that it suffers from shadowing and concern for eye safety, resulting in a reduction in average TX power and hence a reduction in total power efficiency.

The diffuse structure is resistant to shadowing and simple to utilize, allowing for more mobility. The diffused system, on the other hand, has a higher path loss and so needs greater TX power levels and a wider photo-detecting area at the RXs. It also experiences multi-path dispersion, which occurs when the transmitted signal travels through numerous paths to the RX as a result of reflections off the walls, ceiling, and other objects. ISI is caused by diffused systems' multi-path propagation, which becomes essential at larger data rates.

Ambient light, which is a mixture of incandescent light, fluorescent light, and sunshine, is a noisy component of indoor OWC systems, making it a critical issue in reaching better S/N at the RX [56].

Background noise, multi-path dispersion, photo-detector high capacitance, and optical safety standards are all factors in OWC systems. In this subsections, these constraints are briefly explored.

2.8.1 Multi-path Characteristics of the Channel for Diffused Radiation

The diffused linkages rely on light that is reflected from the walls, ceiling, or any other diffusely reflecting object. Due to such reflections, the optical signal from the TX to the RX experiences temporal dispersion. This results in ISI, which is the main big obstacle to transmission speed [40]. The transmitted pulse spreads due to multi-path propagation, resulting in smaller pulse amplitudes and a wider delay-spread. This limits the maximum transmission rate, which is determined by the size of the room and the reflection coefficients within it [79].

Several innovative strategies have been developed in order to overcome this. One of these is the use of an ADR [80]. Several photodetectors with a limited FOV are used in ADR. In order to capture light,

each photodetector is directed in a separate direction with varying azimuth (Az) and elevation (El) angles [37].

2.8.2 Optical Eye Safety Requirements

If used incorrectly, optical wireless devices, like their radio equivalents [81], can cause harm to the eyes and/or skin. However, due to the eye's capacity to concentrate and focus optical energy, the damage to the eye is more severe. The amount of radiation risk is determined by a variety of factors, including beam characteristics, operational wavelength, exposure intensity, exposure time, and distance from the eye [2]. Depending on the wavelength and whether the source is an LED or laser, source size may also have an impact on the risk. Diffuse big area sources are generally safer because their power cannot be focused as sharply onto the retina as a point source, however this is not always the case. The quantity of optical power that should be transmitted by the TX is limited by eye safety considerations, which limits the range of an OWC system. The international electro-technical commission (IEC) establishes eye safety regulations, and LDs are classed into classes 1, 2, 3A, and 3B according to their total radiated power. They specify that all TXs must still be class 1 eye safe at all times, and that the launch power for systems using laser sources must not exceed 0.5 mW [66].

2.8.3 Photodetector High Capacitance

IM/DD is used by a number of OWC systems. The DD RX's S/N is proportionate to the square of the optical power received. Furthermore, eye safety restrictions and electricity utilization limit the transmitted power. Due to these constraints, to gather the most power and enhance S/N, a photodetector with a big photosensitive region should be employed. Regrettably, a big photosensitive area leads to excessive capacitance (as the

photodetector capacitance is proportional to the area of the photodetector). Large detector capacitance decreases the available RX bandwidth because of the capacitance serving as a low-pass filter at an amplifier's input. Instead of using a single photodetector, a group of photodetectors is used to minimize the impacts of excessive capacitance while also maximizing the gathered power [2]. To expand the RX's actual area of collection, it is preferable to use an optical concentrator [71].

2.8.4 Interference from Ambient Light Sources

The OWC RXs detect both the targeted signal and ambient light-induced background noise [2]. Sunlight, incandescent lights, and fluorescent lamps are the three primary sources of ambient lighting [67] see figure (2.7). Even with the use of optical filtering, light from the sun, the sky, and incandescent bulbs is virtually unmodulated and can be picked up at average powers that are far higher than the intended signal. Shot noise, which is the main source of noise in most IR RXs, is caused by the direct current (D.C.) photocurrent that results [82]. Within the photodetectors' wavelength range, these sources produce a large amount of power and also add shot noise, and when their intensity is high, they can saturate the photodetector [30]. If disregarded, artificial ambient light sources generate a periodic interference signal that has the potential to reduce connection performance. Because of this, it is essential to understand ambient light sources in terms of both their optical power spectra and observed electrical spectra in order to create efficient strategies for reducing the interference they cause [83].

Diversity detection is an effective and easy strategy for reducing the damaging effects of multi-path dispersion and ambient light noise [84]. These RXs have the ability to spatially exclude unwanted signals, significantly lessening the effects of background light noise [85].

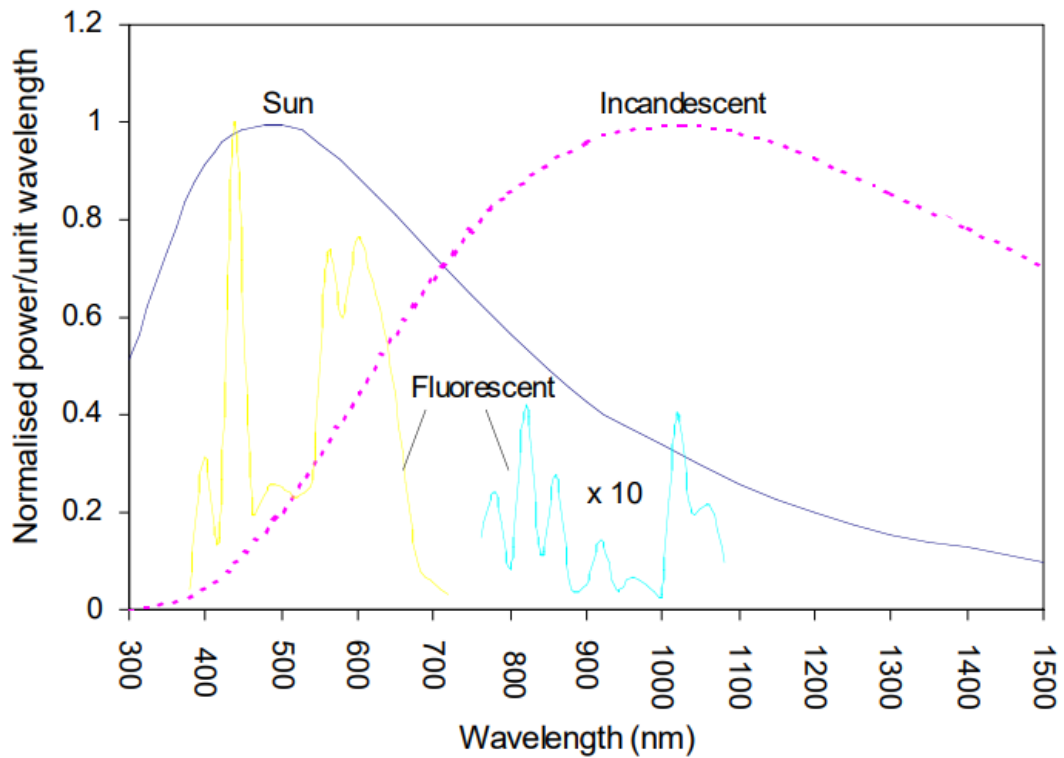


Figure (2.7): Noise sources' spectral power densities, both natural and artificial [2].

2.9 Angle Diversity Receiver

Diffuse system linkages depend on reflections from surfaces like the wall, ceiling, and other reflectors rather than TX-RX alignment. When compared to direct-LOS lines, diffuse communication links are influenced by multi-path dispersion (which produces pulse-spread and considerable ISI), as well as greater path losses [86]. The transmitted optical signal is significantly harmed by noise from directed sources (natural and artificial), potentially reducing the S/N [35].

Diversity detection is a suitable solution for combating background noise as well as multi-path dispersion since it can result in considerable performance improvements [29]. Direct noise rays are rejected, and reception is based on reflected components of the signal. Signal detection

has been found to increase by expanding the number of active branches on a RX [35]. Multiple detectors directed in various directions are used in the ADRs' design. The detectors' small-FOVs are optimized to contain the optical signal and reduce background noise. Each detector's received optical signal can be treated independently, and the selection or combining algorithms can be used to process it. Every branch has a distinct pointing direction that is established by two angles, Az and El [38].

There are a variety of different diversity schemes to examine. SBC, MRC, and EGC are three of the most popular strategies. They differ in how the signals are weighed and merged. SBC merely chooses the branch with the highest S/N out of all the others [28]. In contrast to the SBC strategy, MRC makes use of every branch. An adder circuit is used to mix the output signals from each branch. In order to increase the S/N, each input is added to the circuit with a weight (according to its S/N) [14]. EGC, on the other hand, is MRC in general but does not attempt to weight the signals; all of the weights at all of the diversity branches are the same. The EGC approach may be described using the same signal processing description as before [28].

2.10 Model for Multi-Path Propagation

The position of the TX, RX, and reflectors, as well as their patterns, affect the propagation properties of an internal optical wireless channel. The movement of both people and things has an impact on these features as well, but because this movement is slow compared to the speed of data transmission, the channel is thought to be fixed at specific TX and RX locations. The signal, in order to reach the recipient, takes different paths, and this leads to the spread of the signal, which in turn leads to the ISI of the signal, and as a result, the amount of data transmitted is limited. As the room dimensions' increase, the multi-path dispersion rises due to the increase in the distance of the ray takes to reach the recipient.

Gfeller, F.R., and Bapst, U. measured the reflections of a variety of substances employed in the indoor environment [87]. Based on the surface roughness and incidence angle, they observed that reflectivity ranged from 0.4 to 0.9, while reflectivity for white plaster walls ranged from 0.7 to 0.85 [87]. They also found that the power reflected off the walls or ceiling takes on a shape similar to a Lambertian pattern. Thus, in their study and this dissertation, the reflecting components were viewed as tiny emitters that distribute the received data along numerous paths from TX to RX, improving the diffuse channel's tolerance to shadowing.

The power emitted into a solid-angle element by the TX may be represented as [27]:

$$dp_n = \frac{n+1}{2\pi R_1^2} p_{source} dA \cos^n \phi_1 \cos \phi_2 \quad (2-10)$$

where $(n+1)/2$ guarantees that integrating throughout the surface of a hemisphere delivers the total average transmitted optical power (P_{source}) produced by the source, and ϕ_1 is the incidence angle in relation to the TX's normal, ϕ_2 denotes the angle formed by the incident ray (R_I) from the TX and the normal of the reflecting element, n is the mode number defining the radiated beam's shape, R_I is the separation between the reflecting component and the TX, and dA is the reflecting element's area. Accordingly, the half-power half-angle (h_{psa}) is connected to the transmitted beam's n mode number [30].

$$n = \frac{-\ln(2)}{\ln(\cos(h_{psa}))} \quad (2-11)$$

To focus the energy on a certain region of interest, n is greater for sources with a narrow beam, whereas a Lambertian source has a value of n equal to 1. Because all surfaces are assumed to be rough, n equal to '1' is a good choice [88].

Due to the surface elements reflecting the signal in different directions and in the shape of a Lambertian pattern, the received power at the detector is given by[27]:

$$dp_r = \frac{dp_n}{\pi R_2^2} A_r \Gamma \cos^{n_{elem}} \beta_1 \cos \delta \text{rect} \left(\frac{\delta}{FOV} \right) \quad (2-12)$$

R_2 is the distance separating the RX from the reflecting element, Γ is the reflection coefficient of the reflecting element, β_1 is the angle made by the reflected ray's normal and the reflective element's normal R_2 , and δ is the angle between the normal of the RX and the incident ray, A_r is the area of the detector, and n_{elem} is the mode number of the reflecting element. Finally, $\text{rect}(\delta/FOV)$ represents the condition that if the arriving ray is incident at an angle greater than the angle of the FOV, then the received power drops to zero.

2.10.1 Calculation of Received Optical Power Using Ray Tracing

Because of the multiplicity of propagation, the rays take several paths to reach the destination of the recipient, and this leads to a temporal dispersion, so the received power is calculated using the ray tracing algorithm. Optical rays that have been reflected by various reflectors are tracked to the detector or additional reflectors by following all possible pathways. The surfaces that reflect light in a room were split up into a number of equal-sized, square-shaped reflection elements to simulate the reflections. The size of the surface element determines how accurately the received optical signal power and impulse response shape are shaped. It has been suggested that the reflection components are small TXs that from their centers, dilute the incoming signals into Lambertian patterns with $n=1$ radiation lobe modes [30].

The first two reflections get the most of the sent optical power, while the reflections beyond the second-order are quite modest [37]. As a result,

reflections up to 2nd order were taken into account in the modeling of the optical wireless channel and illuminance noise sources in this dissertation. The ray tracing setup for a diffuse channel is seen in figure (2.8). Tracing every possible light path between the TX and RX will allow to determine the impulse response of the OWC channel.

When 1st order reflections (p_{r1}) and 2nd order reflections (p_{r2}) are taken into consideration, the entire received optical power (P_{rt}) at the RX may be represented as [27]:

$$P_{rt} = \sum_{j=1}^M (p_{rj}) \quad (2-13)$$

M is the total number of reflecting surfaces in the room for 1st and 2nd order reflections.

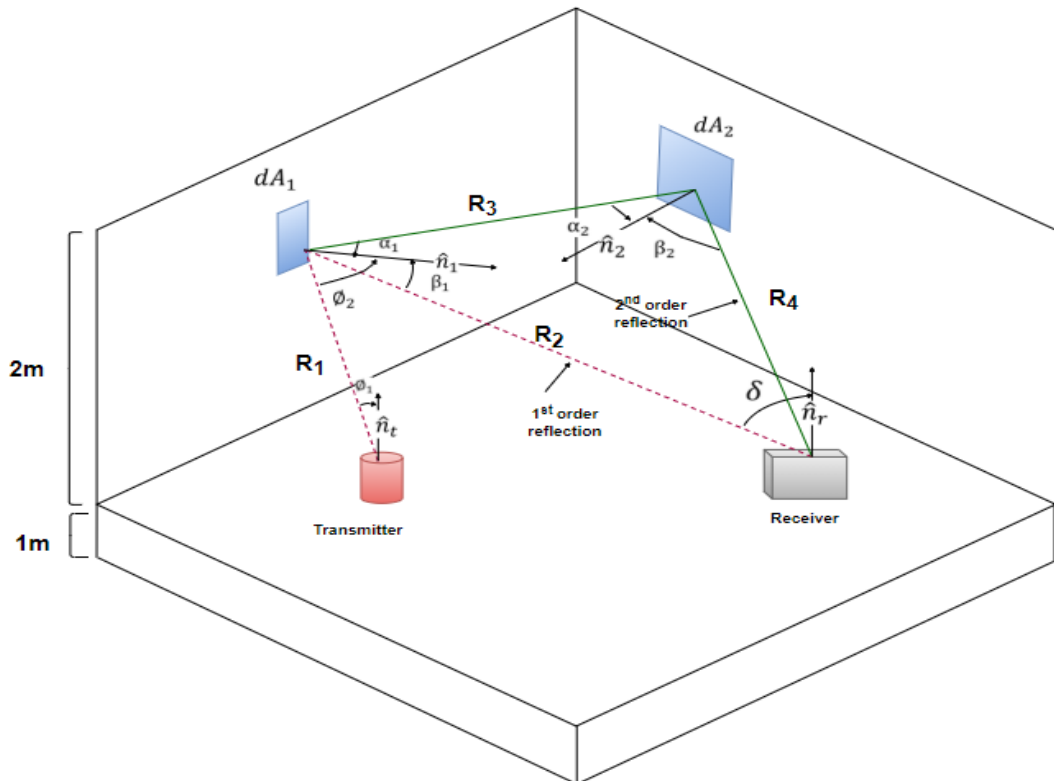


Figure (2.8): Ray tracing for first and second-order reflection for diffuse design.

2.10.1.1 Calculation of First-Order Reflection

Upon placement of the TX and RX on the communication floor, in this case, there is no direct communication between the TX and RX, so the signal is subject to several reflections to reach the RX. Based on the conclusions of Gfeller, F.R., and Bapst, U. [87] that plaster walls can be regarded as Lambertian reflectors because they have reflecting surfaces ($n=1$), using equation (2.10) twice, the optical received power of 1st order reflections (p_{r1}) can be calculated, Light first moves from the transmitting source TX to the reflecting surface, after which it moves from the latter to the receiving source RX [73], as presented in figure (2.9):

$$p_{r1} = \frac{n+1}{2\pi^2 R_1^2 R_2^2} p_{source} \Gamma_1 dA_1 A_{eff}(\delta) \cos^n \phi_1 \cos \phi_2 \cos^{n_{elem}} \beta_1 \quad (2-14)$$

The effective signal-collection area is $A_{eff}(\delta)$, which can be found in equation (2.4). After substituting into equation (2.14), the received power becomes:

$$p_{r1} = \frac{n+1}{2\pi^2 R_1^2 R_2^2} p_{source} \Gamma_1 dA_1 A_r T_f(\delta) G_c(\delta) \cos^n \phi_1 \cos \phi_2 \cos^{n_{elem1}} \beta_1 \cos \delta \text{rect}\left(\frac{\delta}{\Psi_c}\right) \quad (2-15)$$

dA_1 is the area of the first reflecting element, Γ_1 represents the reflection coefficient of the first reflecting element, n_{elem1} is the mode number for the first reflective element, the concentrator gain is $G_c(\delta)$, and $T_f(\delta)$ is the filter transmission (where it isn't take into account in this dissertation).

As illustrated in figure (2.9), four angles are required by equation (2.15), and they can be computed as [75]:

$$\begin{aligned} \cos(\phi_1) &= \frac{\hat{n}_t \cdot (r_1 - r_t)}{R_1} & \cos(\phi_2) &= \frac{\hat{n}_1 \cdot (r_t - r_1)}{R_1} \\ \cos(\beta_1) &= \frac{\hat{n}_1 \cdot (r_r - r_1)}{R_2} & \cos(\delta) &= \frac{\hat{n}_r \cdot (r_1 - r_r)}{R_2} \end{aligned} \quad (2-16)$$

where r_t , r_l , and r_r represent the location of the TX, reflection element, and RX, respectively. While \hat{n}_t , \hat{n}_1 , and \hat{n}_r represent the normal for the TX, first reflection element, and RX respectively.

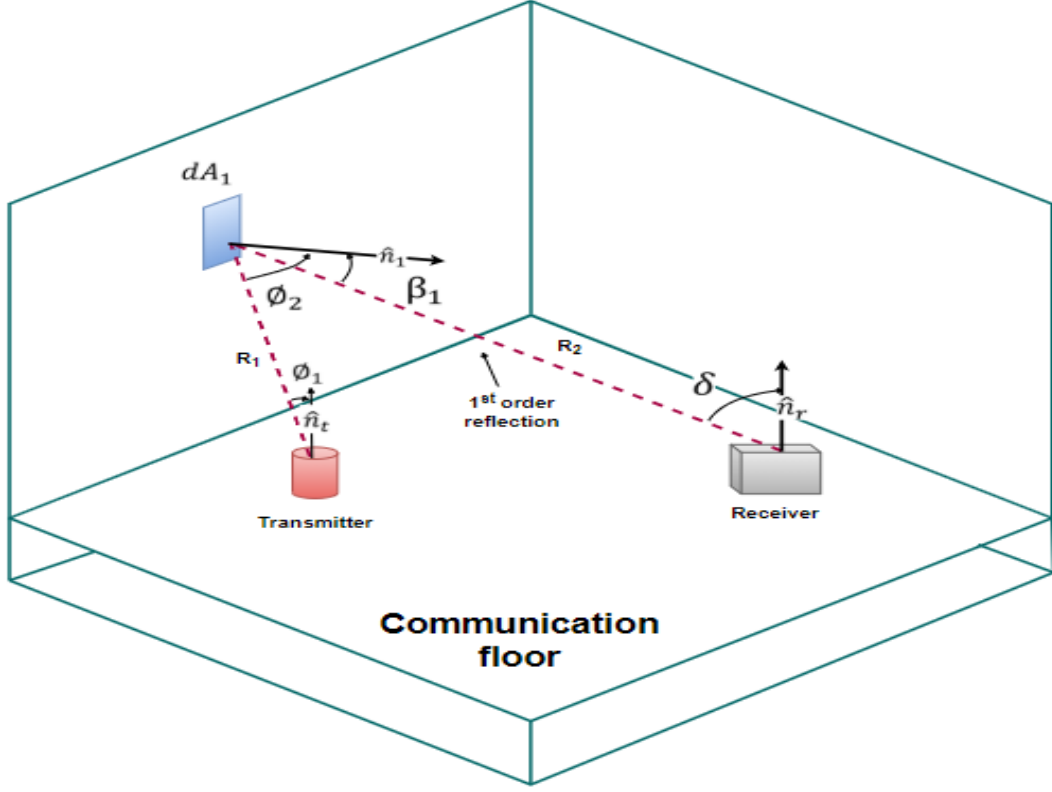


Figure (2.9): Ray tracing for first-order reflection.

2.10.1.2 Calculations of the Second-Order Reflection

In order to calculate the power received for the second reflection at the receiving end, it is calculated from the TX to the first reflecting element, from the first reflecting element to the second reflecting element, and finally from the second reflecting element to the RX, as shown in figure (2.10), where we get [33]:

$$p_{r2} = \frac{n+1}{2\pi^3 R_1^2 R_2^2 R_3^2 R_4^2} p_{source} \Gamma_1 \Gamma_2 dA_1 dA_2 A_{eff}(\delta) \cos^n \phi_1 \cos \phi_2 \cos^{n_{elem1}} \alpha_1 \cos \alpha_2 \cos^{n_{elem2}} \beta_2 \cos \delta \text{rect}\left(\frac{\delta}{FOV}\right) \quad (2-17)$$

where R_3 between the first and second reflecting elements is the separation distance, R_4 between the second reflecting element and RX is the separation distance, the second reflecting surface's reflection coefficient is Γ_2 , dA_2 square-shaped second reflecting element's surface area, n_{elem2} is the 2nd mode number of the reflecting surface, α_1 is the angle formed by the first reflective element's normal and the reflected ray R_3 , α_2 is the angle formed by the second reflective element's normal and the incident ray R_3 , β_2 is the angle between the normal of the second reflective element and reflected ray R_4 , and δ is the angle between the normal of the RX and the incident ray.

Second-order reflection requires six angles [75], which may be calculated similarly to 1st-order reflection by scanning the ray from TX to RX as shown in figure (2.10):

$$\begin{aligned}
\cos(\phi_1) &= \frac{\hat{n}_t \cdot (r_1 - r_t)}{R_1} & \cos(\phi_2) &= \frac{\hat{n}_1 \cdot (r_t - r_1)}{R_1} \\
\cos(\alpha_1) &= \frac{\hat{n}_1 \cdot (r_2 - r_1)}{R_3} & \cos(\alpha_2) &= \frac{\hat{n}_2 \cdot (r_1 - r_2)}{R_3} \\
\cos(\beta_2) &= \frac{\hat{n}_2 \cdot (r_r - r_2)}{R_4} & \cos(\delta) &= \frac{\hat{n}_r \cdot (r_2 - r_r)}{R_4} \tag{2-18}
\end{aligned}$$

where \hat{n}_2 and r_2 represent the normal of the 2nd reflection element and represent the location of the second reflection element respectively.

Finally, the distances R_{dir} , R_1 , R_2 , R_3 , and R_4 may be determined using the formula below [75]:

$$\begin{aligned}
R_{dir} &= \sqrt{(x_r - x_t)^2 + (y_r - y_t)^2 + (z_r - z_t)^2} \\
R_1 &= \sqrt{(x_1 - x_t)^2 + (y_1 - y_t)^2 + (z_1 - z_t)^2} \\
R_2 &= \sqrt{(x_r - x_1)^2 + (y_r - y_1)^2 + (z_r - z_1)^2} \\
R_3 &= \sqrt{(x_2 - x_1)^2 + (y_2 - y_1)^2 + (z_2 - z_1)^2}
\end{aligned}$$

$$R_4 = \sqrt{(x_r - x_2)^2 + (y_r - y_2)^2 + (z_r - z_2)^2} \quad (2-19)$$

where R_{dir} used for direct link between TX and RX, R_1 and R_2 are used for calculating the distance from the sender to the RX for first-order reflection, and R_1 , R_3 , and R_4 are used for calculating the distance from the sender to the RX for second-order reflection

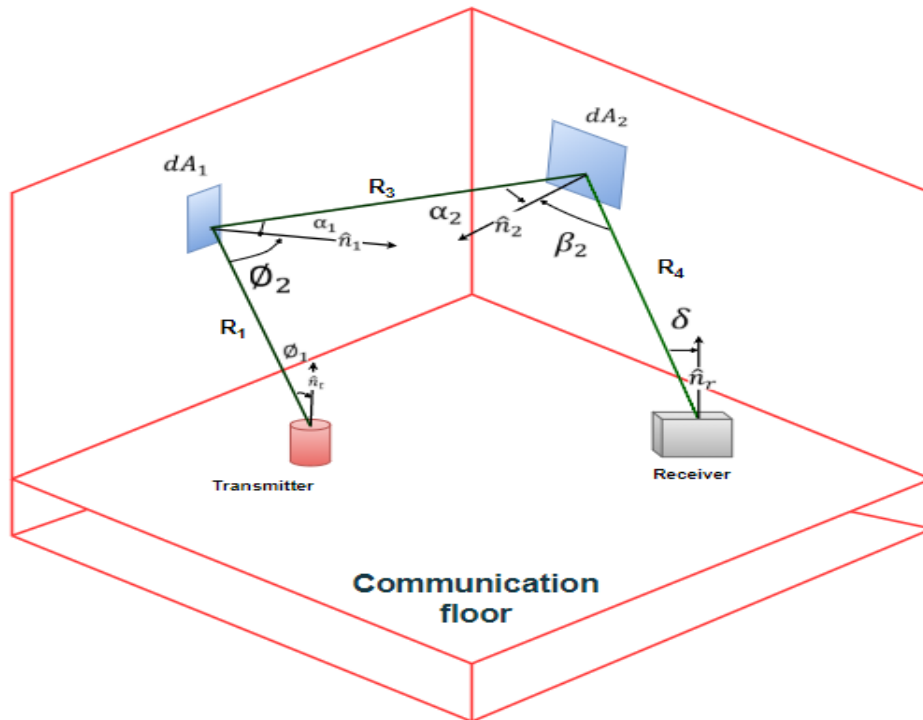


Figure (2.10): Ray tracing for second-order reflection.

2.11 Impulse Response

The received optical power from multi-path reflection can be specified using the channel impulse response. A simulation identical to that described by Barry et al. [88] was used to calculate the impulse response owing to the varied reflections. The impulse response is practically continuous, but the reflective elements are divided into small square shapes in order to obtain a reasonable delay in the calculation and, at the same time, acceptable accuracy. Thus, depending on how long it takes each ray to arrive at the RX, the impulse response shows the received optical power as it arrives to the

RX in "time bins" of varying lengths of time. The time bin value was synchronized to the length of time needed for light to go between close-by reflecting elements by gradually tracing rays from the centers of various reflective elements. Consequently, a reasonable suggestion for the time bin width is made [33]:

$$t_{bin} = \frac{\sqrt{dA}}{c} \quad (2-20)$$

For a certain TX-RX position, rays received at identical time intervals are combined and stored. The calculation is very accurate when the dA is close to zero, but at the expense of a delay in the calculations, which takes a long time.

The impulse response of the indoor optical wireless channel may be thoroughly examined. The impulse response may be used to derive a variety of metrics, including R.M.S delay-spread, path loss, and S/N, the latter of which requires the reception and ambient background noise to be determined.

2.12 R.M.S Delay-Spread

When the TX and RX are both positioned on the communication surface, in this case, direct communication is absent between the TX and RX, so the ray takes many paths to reach the receiving point, and this leads to the spread of the pulse, which leads to ISI [89]. Because some rays take a long path and others take a short path to reach the reception, so each ray has a different effect in spread of the signal, so the R.M.S is taken to calculate the delay-spread , where it given by [90]:

$$D_{spr} = \sqrt{\frac{\sum (t_j - \mu)^2 pr_j^2}{\sum pr_j^2}} \quad \mu = \frac{\sum t_j pr_j^2}{\sum pr_j^2} \quad (2-21)$$

where t_j represents the temporal delay connected to the received optical power (which depicts the impulse response behavior within a time bin period) and μ denotes the mean delay. When the position of the TX, reflecting surfaces, and RX are constant, the delay-spread is predictable fixed. As the impulse response is calculated, the delay-spread is established for each site. Actually, if the reflective objects in the space change, such fans moving or people entering and leaving, the R.M.S delay-spread for a given TX and RX position may change. These impacts are not taken into account in this dissertation.

2.13 Ambient Light Calculations

The speed restrictions of optoelectronic devices (LEDs and PIN photodiodes), high path loss, multi-path dispersion, shot noise caused by natural light on the receiving photodetector, and artificial light interference are all factors that affect how well wireless IR systems function.

Shot noise is produced by both natural and artificial ambient light, and it is frequently the dominating noise source. Daylight, incandescent light (such as halogen and tungsten filament lamps), and fluorescent light sources are the main sources of ambient light in an interior setting. Within silicon photodetectors' wavelength range, these sources produce a sizable quantity of power, as well as add shot noise, and when their intensity is sufficient, they can saturate the photodetector. Although ambient light can be significantly brighter than the data signal being delivered, various methods (like optical filters) can be utilized to diminish its impact [30]. A Lambertian source can be used to represent ambient light, such as incandescent bulb lighting.

As a result, the background light level produced by such a source at the RX may be represented as [29]:

$$P_{t_noise,v} = (p_{d_noise} + p_{r_noise})_v \quad (2-22)$$

where P_{d_noise} represents direct power noise from lamps, the total optical power received from reflecting components (first and second order reflection) across the room is P_{r_noise} , and v is the number of lamp.

The received noise power equations in first and second-order reflection, as seen in figure (2.11), can be written with the help of the received power equations for the signal given in section sub subsections (2.10.1.1) and (2.10.1.2) with some differences as written [30]:

$$p_{r_noise1} = \frac{n_{lamp}+1}{2\pi^2 R_1^2 R_2^2} p_{lamp} \Gamma_1 dA_1 A_r G_c(\delta) \cos^{n_{lamp}} \phi_1 \cos \phi_2 \cos^{n_{elem1}} \beta_1 \cos \delta \text{rect}(\delta/FOV) \quad (2-23)$$

$$p_{r_noise2} = \frac{n_{lamp}+1}{2\pi^3 R_1^2 R_3^2 R_4^2} p_{lamp} \Gamma_1 \Gamma_2 dA_1 dA_2 A_r G_c(\delta) \cos^{n_{lamp}} \phi_1 \cos \phi_2 \cos^{n_{element1}} \alpha_1 \cos \alpha_2 \cos^{n_{element2}} \beta_2 \cos \delta \text{rect}(\delta/FOV) \quad (2-24)$$

while the noise power received from the direct road can be calculated as follows:

$$p_{d_noise} = \frac{n_{lamp}+1}{2\pi R_{dir}^2} p_{lamp} A_r G_c(\delta) \cos^{n_{lamp}}(\phi_1) \cos(\delta) \text{rect}(\delta/FOV) \quad (2-25)$$

where p_{lamp} is the power emitted by the lamp, n_{lamp} is the mode number of the lamp, and R_{dir} is the separation distance between the lamp and the RX. The sum of noise power hitting the detector from all spotlight sources (direct noise power, first and second order reflection noise power) is the overall noise power reaching the RX at a certain point, and it may be written as:

$$P_{t_noise} = \sum_{v=1}^V (p_{d_noise})_v + \sum_{v=1}^V \sum_{s=1}^S (p_{r_noise1})_v + \sum_{v=1}^V \sum_{h=1}^H (p_{r_noise2})_v \quad (2-26)$$

where V represents the over-all number of lamps, S is the overall number of the first reflecting surfaces, and H is the total number of the second-order reflective surfaces. The calculations of the angles for 1st and 2nd-order reflection are the same as the calculations given in section (2.10), except that the TX here is the lamp, not the LED, so the normal vector is \hat{n}_{lamp} for transmitted angle ϕ_1 .

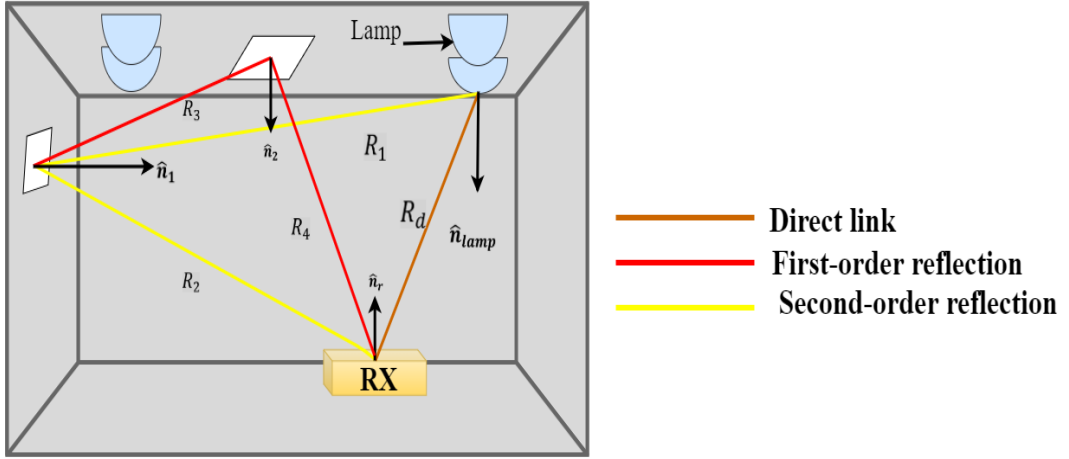


Figure (2.11): Ray tracing of lamps' direct path, first and second order reflections.

2.14 S/N and BER Calculations

The best method for evaluating the performance of the OWC system is the S/N, which takes noise and signal dispersion into consideration. The S/N connected with a received signal may be determined in O.O.K by taking into account the following factors: P_{s1} and P_{s0} (the powers corresponding to logic levels 1 and 0). ISI is determined by these powers (P_{s1} and P_{s0}), which determine eye opening during a sample instant. The S/N is calculated as follows [38]:

$$S/N = \left(\frac{R \times (p_{s1} - p_{s0})}{\sqrt{\sigma_{pr}^2 + \sigma_{bn}^2 + \sigma_{s1}^2} + \sqrt{\sigma_{pr}^2 + \sigma_{bn}^2 + \sigma_{s0}^2}} \right)^2 \quad (2-27)$$

where $R=0.5$ A/W [29], the shot noises σ_{sl} and σ_{s0} are related to the received signals P_{sl} and P_{s0} , respectively. The background shot noise element σ_{bn} may be calculated using its related power level $p_{t-noise}$ as [91]:

$$\sigma_{bn} = \sqrt{2 \times q \times p_{t-noise} \times R \times BW_{receiver}} \quad (2-28)$$

where $p_{t-noise}$, and $BW_{receiver}$ represent the received background power and RX bandwidth respectively. σ_{pr} represents the preamplifier noise. σ_{pre} can be found by using following equation [92]:

$$\sigma_{pre} = \text{noise current spectral density} \times \sqrt{BW_{receiver}} \quad (2-29)$$

The noise related to the received power (p_{sl} and p_{s0}) can be measured from [91]:

$$\sigma_{sj} = \sqrt{2 \times q \times p_{sj} \times R \times BW_{receiver}} \quad (2-30)$$

where σ_{sj} is the shot noise connected to the signal that was received (p_{sj}), j is associated with logic levels '1' and '0'.

The number of bits in error divided by the total number of bits received at the RX is known as the BER [55]. To find it apply the following law [86]:

$$BER = \frac{1}{2} \operatorname{erfc} \left(\sqrt{\frac{S/N}{2}} \right) \quad (2-31)$$

where S/N is expressed as a ratio rather than in decibels.

2.15 Path Loss and Channel Bandwidth

The integration of the channel impulse response $h(t)$ taking into account reflections from the walls, ceiling, and other objects is known as optical path loss, and it is one of the key characteristics that can be used to measure the signal quality [32]. The path loss can be given by [3]:

$$Path_{loss} = -10 \log_{10} \left(\int_{-\infty}^{\infty} h(t) \right) \quad (2-32)$$

Consequently, poor system performance is caused by an increase in optical power path loss coupled with an increase in delay-spread[93].

Coherence bandwidth of the channel can be calculating by using [3]

$$Bandwidth_{coh,50\%} = \frac{1}{5 \times D_{spr}} \quad (2-33)$$

The decorrelation percentage is indicated here as 50%. OWCs channels don't undergo multi-path fading, but if the LED modulation bandwidth is more than the channel coherence bandwidth, the channel might be classified as a frequency selective channel because of dispersion [3].

2.16 Calculation of the (Received Power, 3dB Channel Bandwidth, and S/N) for ADR

The CDS (wide beam TX with a wide-FOV RX) system uses a single detector that faces upwards and is placed on the communication floor, but this is not the case for ADR; it has many detectors, each of which is oriented in a given direction and inclined at a particular angle; as a result, the RX's normal is not straight, forcing adjustments to the reception angle computation. In the ADR, the reception angle δ must be calculated using the analysis in [26], taking into account the Az and El angles as well as the reflecting elements. In order to determine δ for any detector oriented at (x_r, y_r, z_r) over the communication floor, a point was established on the (1m) above the detector (x_p, y_p, z_p) , as shown in figure (2.12). A triangle can be created by joining the point, the detector's midpoint, and the midpoint of a reflecting element. As a result, the angle of reception from a surface element onto an ADR is defined by [26]:

$$|\overrightarrow{EP}|^2 = |\overrightarrow{PR}|^2 + |\overrightarrow{ER}|^2 - 2|\overrightarrow{PR}| |\overrightarrow{ER}| \cos(\delta) \quad (2-34)$$

the separation distance between the RX and a common point is represented by $|PR|$, the separation distance between the RX and the reflecting element is represented by $|ER|$, and the reflective element's separation from the point is depicted by the symbol $|EP|$.

The following equations can be used to find these distances [26]:

$$|\overline{PR}|^2 = 1 + \left(\frac{1}{\tan(El)}\right)^2 \quad (2-35)$$

$$|\overline{ER}|^2 = (x_r - x_E)^2 + (y_r - y_E)^2 + (z_r - z_E)^2 \quad (2-36)$$

$$|\overline{EP}|^2 = (x_p - x_E)^2 + (y_p - y_E)^2 + (z_p - z_E)^2 \quad (2-37)$$

$$x_p = x_r + \frac{\cos(Az)}{\tan(El)} \quad (2-38)$$

$$y_p = y_r + \frac{\sin(Az)}{\tan(El)} \quad (2-39)$$

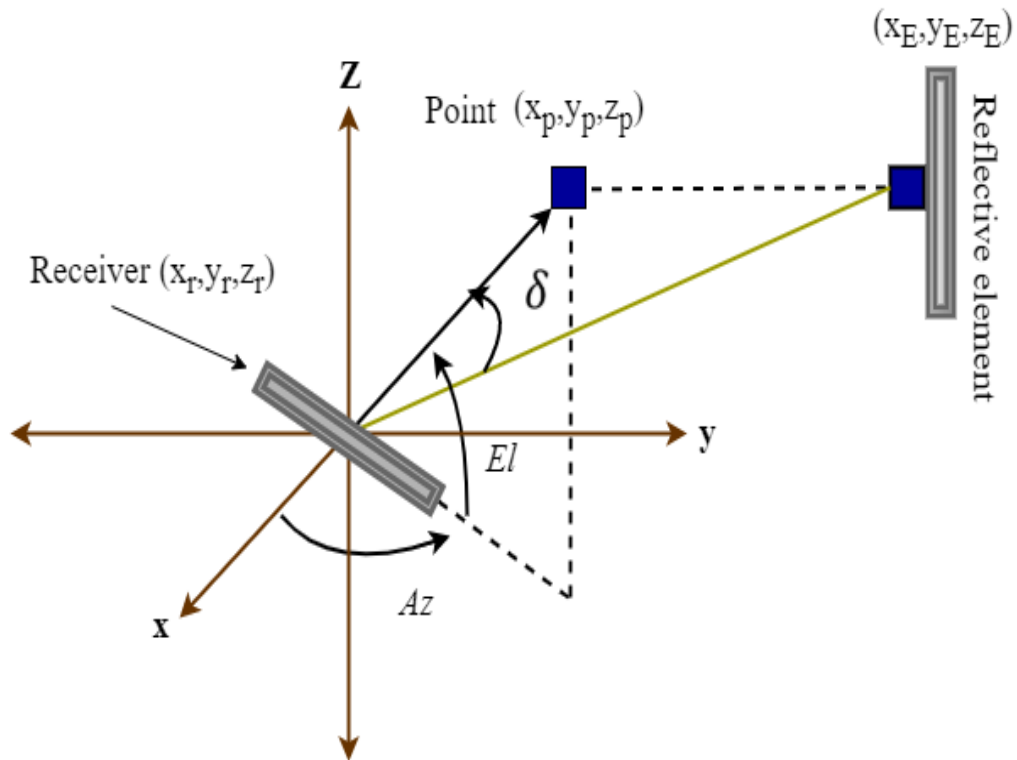


Figure (2.12): Angle of receiving analysis for angle diversity.

$$z_p = z_r + 1 \quad (2-40)$$

with substituting (2.38) - (2.40) in (4.37) produce:

$$|\overline{EP}|^2 = \left[\left(\frac{\cos(Az)}{\tan(El)} + x_r \right) - x_E \right]^2 + \left[\left(\frac{\sin(Az)}{\tan(El)} + y_r \right) - y_E \right]^2 + [(1 + z_r) - z_E]^2 \quad (2-41)$$

Reception angle after find $|PR|$, $|ER|$, and $|EP|$ is:

$$\cos(\delta) = \frac{|\overline{PR}|^2 + |\overline{ER}|^2 - |\overline{EP}|^2}{2 \cdot |\overline{PR}| |\overline{ER}|} \quad (2-42)$$

The power received for first-order reflection while utilizing ADR may be calculated by putting equation (2.42) in the reception angle δ for equation (2.15):

$$p_{r1} = \frac{n+1}{2\pi^2 R_1^2 R_2^2} p_{source} \Gamma_1 A_r dA_1 G_c(\delta) \cos^n \phi_1 \cos \phi_2 \cos^{n_{elem}} \beta_1 \frac{|\overline{PR}|^2 + |\overline{ER}|^2 - |\overline{EP}|^2}{2 \cdot |\overline{PR}| |\overline{ER}|} rect(\delta/FOV) \quad (2-43)$$

while the power obtained for second-order reflection when utilizing ADR may be calculated by adding (2.42) to the reception angle for equation (2.17):

$$p_{r2} = \frac{n+1}{2\pi^3 R_1^2 R_3^2 R_4^2} p_{source} \Gamma_1 \Gamma_2 dA_1 dA_2 A_r G_c(\delta) \cos^n \phi_1 \cos \phi_2 \cos^{n_{element1}} \alpha_1 \cos \alpha_2 \cos^{n_{element2}} \beta_2 \frac{|\overline{PR}|^2 + |\overline{ER}|^2 - |\overline{EP}|^2}{2 \cdot |\overline{PR}| |\overline{ER}|} rect(\delta/FOV) \quad (2-44)$$

In the frequency domain rather than the time domain, the influence of the multi-path effect on optical wireless channel bandwidth may be easily understood. The Fourier transform of the channel impulse response may be used to calculate the channel frequency response $H(f)$ as [42]:

$$H(f) = \int h(t)e^{-j2\pi ft} dt \quad (2-45)$$

The 3-dB channel bandwidth $H(f_{3-dB})$, is commonly used in practice as [42]:

$$|H(f_{3-dB})|^2 = \frac{1}{2} |H(0)|^2 \quad (2-46)$$

where the impulse response can be used to determine the channel DC gain $H(0)$.

$$H(0) = \int h(t)dt \quad (2-47)$$

The SBC scheme is taken into account in the ADR when calculating S/N. SBC is a simple diversity approach. The RX simply selects the branch with the highest S/N among the available branches. The S/N_{SBC} is presented by [29]:

$$S/N_{SBC=MAX_b} \left(\frac{R \times (p_{s1} - p_{s0})}{\sigma_1 + \sigma_0} \right)_b^2, \quad 1 \leq b \leq k \quad (2-48)$$

the overall number of detectors utilized in the angle diversity approach is denoted by k .

CHAPTER THREE

CHANNEL MODELING OF AN INDOOR OWC SYSTEM (SINGLE DETECTOR)

3.1 Introduction

In order to describe the internal OWC system, there are many things that must be prepared and taken into consideration before starting the calculation. First, define the type of the system, whether it is direct or non-direct, LOS or N-LOS. The channel that connects the TX to the RX is taken into consideration. Ambient noise from artificial sources and multi-path dispersion also must be modeled. Finally, a package of simulations for the aforementioned is required.

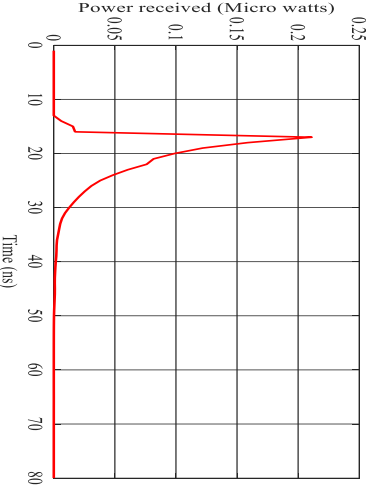
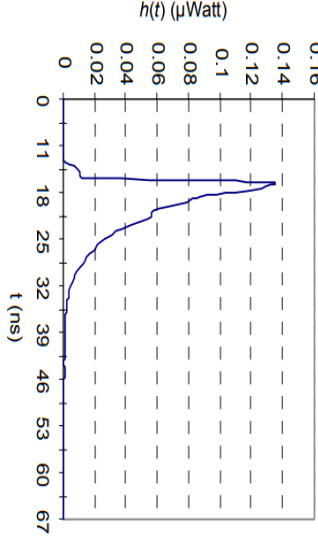
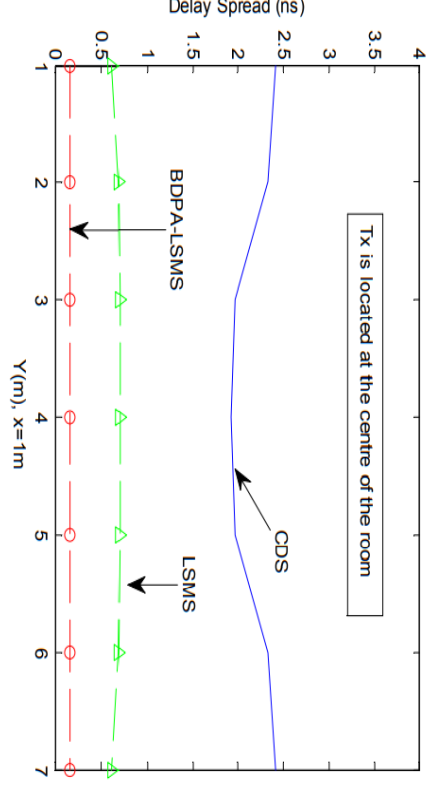
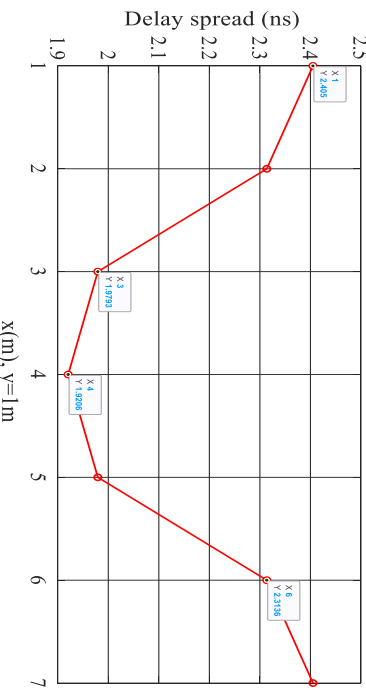
This chapter, investigated the first proposed system after validating the simulation result and ensuring the code is correct. The flowcharts and steps that need are to calculate the parameters are displayed. An investigation is performed by several parameters like delay-spread, path loss, S/N, BER, and channel bandwidth.

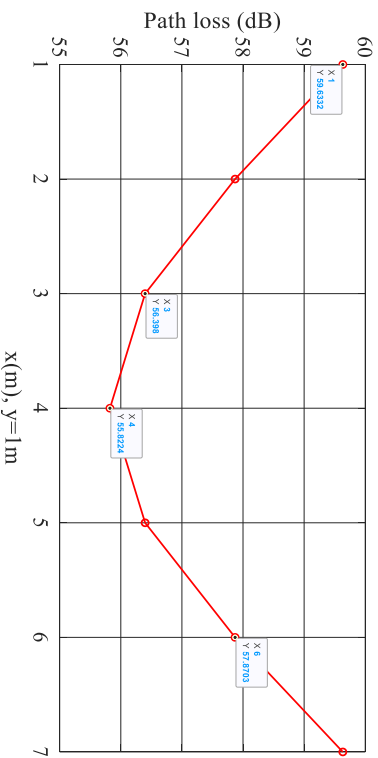
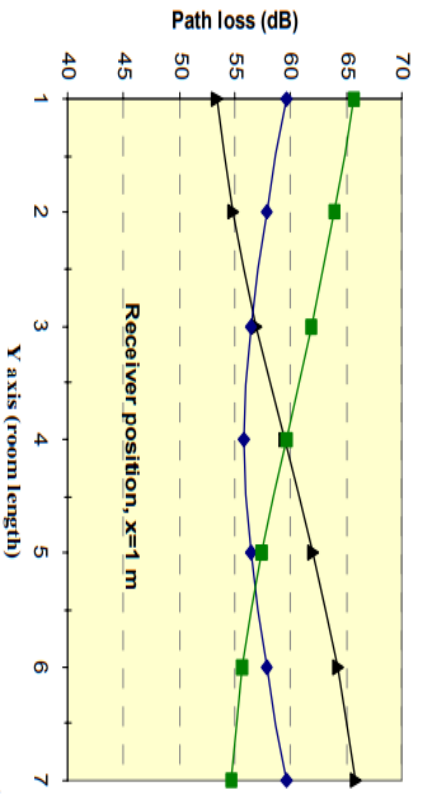
3.2 The Outcomes of the Validation Simulation

The CDS is evaluated for two primary reasons. The first reason is to make sure our simulator is operational and capable of evaluating new OWC systems. The second reason is to utilize existing setups as a starting point for developing new OWC configurations. The simulation's outcomes are presented as an impulse response, R.M.S delay-spread, path loss, and S/N.

Following table (3.1) represent comparison between our validation results and results of the other works.

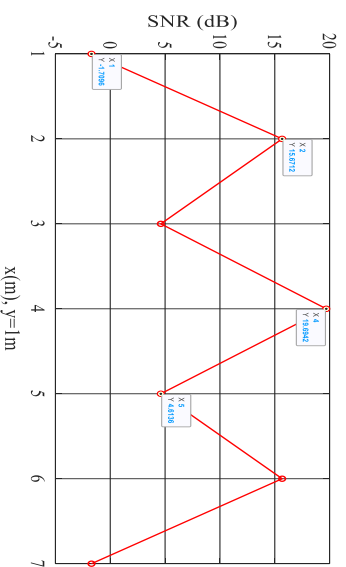
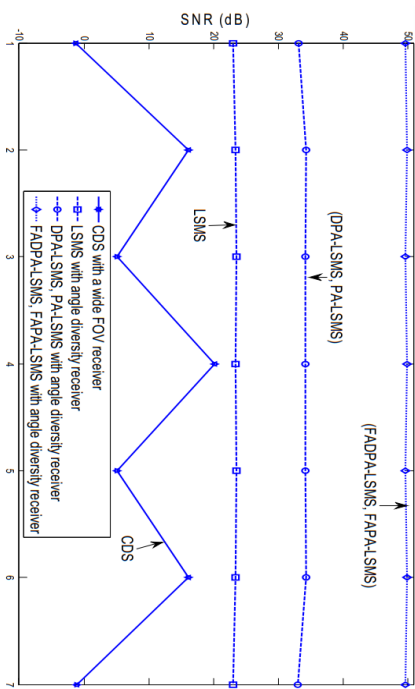
Table (3.1): Comparison between our validation results and previous works.

Ref.	Title	Our validation results	Results from sources	Results from sources
[29]	Impulse response when RX at the corner and TX in the center of the room.	 <p>Power received (Micro watts)</p> <p>Time (ns)</p>	 <p>$h(t)$ (μWatt)</p> <p>t (ns)</p>	 <p>Delay Spread (ns)</p> <p>Y(m), x=1m</p> <p>BDPA-LSMS</p> <p>CDS</p> <p>LSMS</p> <p>Tx is located at the centre of the room</p>
[37]	Delay-spread when TX is placed in the middle of the room and RX is moving along the x-axis at $y = 1$ m.	 <p>Delay spread (ns)</p> <p>x(m), y=1m</p>		



Path loss when TX in the middle of the room and RX moving along x-axis at $y=1$ m. (blue color is the indented path loss of the previous work).

[32]



S/N when RX is traveling along the x-axis at $y = 1$ m and TX is set in the center of the room.

[94]

The CDS system's R.M.S delay-spread , S/N, and path loss, results are quite similar to prior work published in [29], [32], [37], [94], but the impulse response shows a difference of 15% from the previous work. After the results were validated, we could make some changes in the code to be compatible with our own system.

3.3 The Model of the Proposed OWC Single Detector System

The code was adjusted according to the characteristics of our system for the empty square room size (length=5m, width= 5m, and height=3m), once the findings were discovered and compared to earlier work [29], [32], [37], [94]. The TX is positioned directed toward the ceiling on the communication floor (2.5m,2.5m,1m) with emitted power (1W) with a diffuse Lambertian pattern ($n=1$), so there is no direct link between the TX and RX and depend they only on the reflections to reach the rays to the RX. The Lambertian pattern ($n=1$) was used to maintain the integrity of the eyes and skin. Reflection up to 2nd order reflection is considered. The reflection coefficient of the walls and ceiling is $\Gamma = 80\%$. The reflections from the floor are neglected.

Because of the inverse link between the bandwidth of the RX and the photodetector's capacitance as stated in the following law, one of the parameters that has been adjusted is the photodetector area, where the sensitive area of the photodetector has been lowered in order to enhance the RX bandwidth [95]:

$$BW_{receiver} = \frac{1}{2\pi R_l C} \quad (3-1)$$

$$C = \frac{\epsilon_o \epsilon_r A_r}{d_{thick}} \quad (3-2)$$

where C , d_{thick} , ϵ_o , ϵ_r , and R_l are the capacitance of the photodetector, detector thickness, the permittivity of air, the permittivity of silicon, and resistance of

the load, respectively. The values of $d_{thick} = 100 \mu\text{m}$, $R_l = 50 \Omega$ [95], $\epsilon_r = 11.65$ [96], and choose the area of RX $A_r = 10 \text{ mm}^2$, after substituting these values into the equations above, we get that the maximum bandwidth of the RX is 308 MHz and the data rate that can be transmitted is 308 Mbit/sec, as in [9].

The FOV of the RX is narrowed in order to lessen the influence of ambient noise and delay-spread by rejecting the rays that fall at an angle greater than the FOV, but at the expense of reducing the received power. To increase the receiving power and increase the RX bandwidth (by decreasing the area of the RX), the concentrator is used to keep the detector area small while increasing the optical power received at the effective area by converting a group of rays that are incident on a wide area into a group that emerges from a smaller region and fits the photodetector area. The equations found in sub subsections (2.10.1.1) and (2.10.1.2) are used to find the received power at the receiving point, taking into account the concentrator gain, which can be found from equation (2.5). The R.M.S delay-spread can be found from the equation found in section (2.12).

To assess the system while taking into account ambient noise and mobility, four lamps are used; they are positioned 2m above the communication floor; the distance of the lamp from the wall is 1m; and the distance between the lamps is 3m. The lamp distribution along the x-axis at $y = 1\text{m}$ and $y = 4\text{m}$. The positions of these lamps are (1m, 1m, 3m), (4m, 1m, 3m), (1m, 4m, 3m), (1m, 4m, 3m), and (4m, 4m, 3m) as shown in figure (3.1). Equations given in section (2.13) can be used to calculate ambient noise. The preamplifier utilized in the suggestion system is a trans-impedance amplifier (TIA) and the thermal noise current of it is $2.5 \text{ pA}/\sqrt{\text{Hz}}$, S/N can be found with the help of equations found in section (2.14). The power of reflection from reflecting elements is Lambertian in nature.

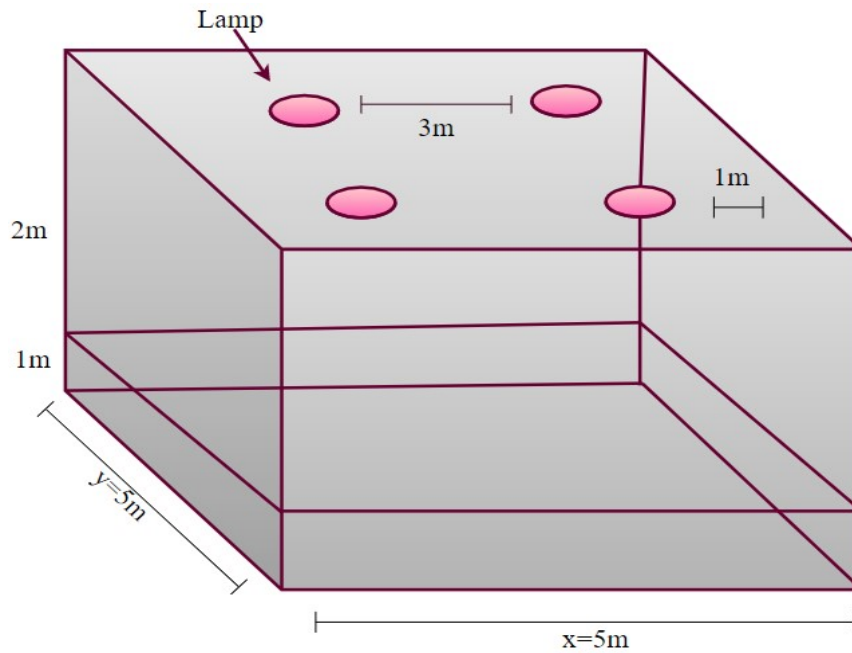


Figure (3.1): Distribution of lamps for room dimension (5m, 5m, 3m).

The reflecting elements are divided into a series of equal square shapes, where the size of the square-shape of the reflective elements for first-order reflection is $5\text{cm} \times 5\text{cm}$ (dA_1) and $20\text{cm} \times 20\text{cm}$ (dA_2) for second-order reflection. This division is chosen to have an acceptable time for simulation and a reasonable accuracy result. The FOV is optimized by changing it in steps to these values: (FOV=90°, FOV=60°, FOV=30°, and FOV=10°). The results of each change are shown in order to know which FOV boost the system's performance and lessen the impact of background and ambient noise. The following sections contains the flowcharts of the simulation.

3.4 MATLAB Simulation Flowcharts of the Single Detector Model

In this section will contain the steps and flowcharts of calculating the parameters of proposed system in the MATLAB program.

3.4.1 Calculation of Total Received Power

A public flowchart of the power received from the first-order reflection and second-order reflection is shown in figure (3.2). The calculation is divided into two parts: the first part calculates received power from first-order reflection, and the second part calculates received power from second-order reflection. Finally, the total impulse response is produced by combining the first and second order reflection impulse responses.

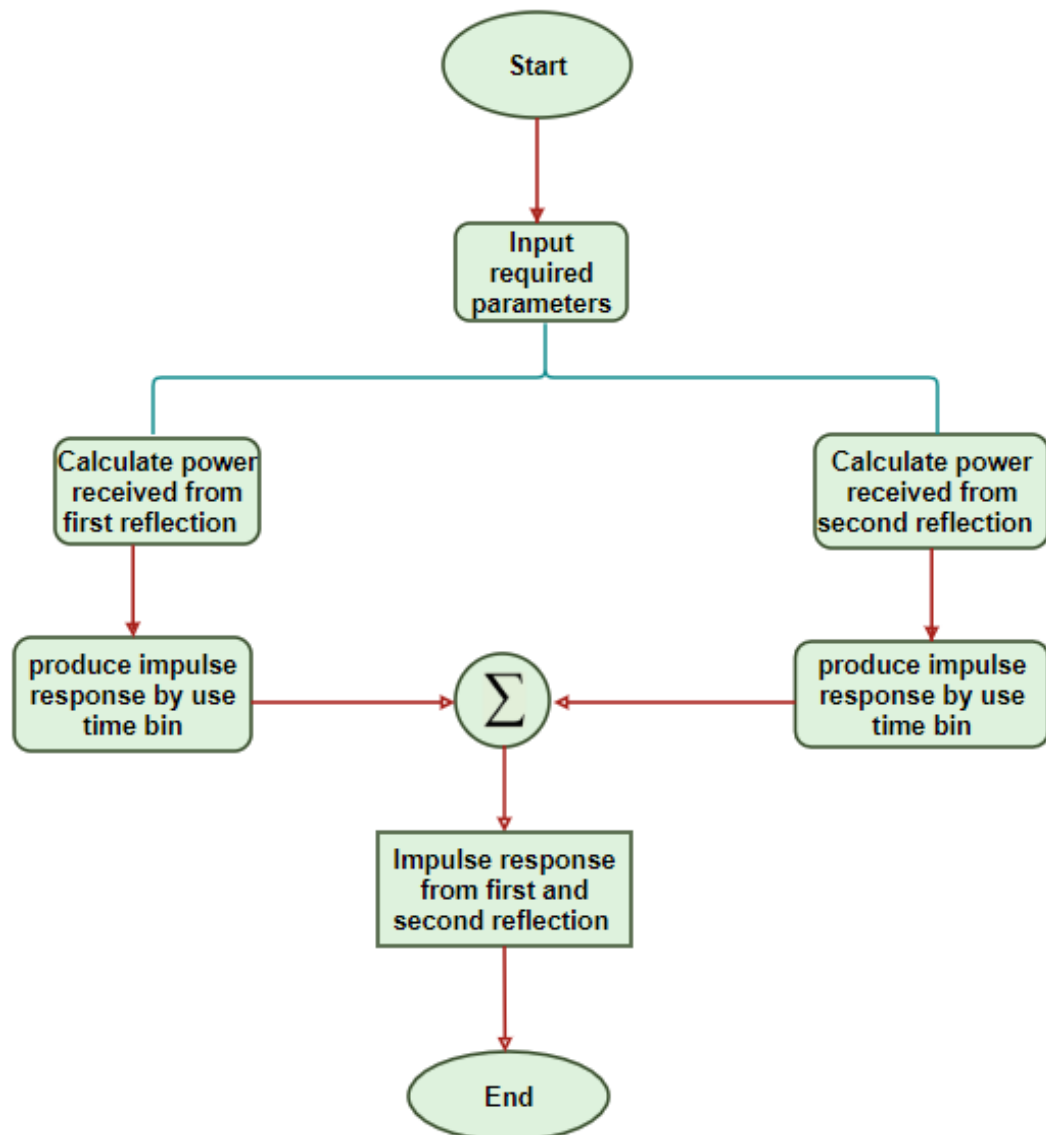


Figure (3.2): Flowchart of calculating first and second order reflection received power and produce impulse response.

3.4.1.1 Flowcharts of Calculating First Order Reflection

To calculate the received power from first reflection elements, follow these steps:

1. Define all the values that are present in equation (2.15), such as area of the first reflection element (dA_l), reflection coefficient for first reflection elements Γ_l , mode number n , area of the RX A_r , responsivity R , speed of light c , FOV, transmit power p_{source} , and that are needed in the calculation, like the location of the TX (x_t, y_t, z_t), and the location of the RX (x_r, y_r, z_r)
2. The initial value of x_1 and y_1 is 0.025m to take the center of the reflective element and the increment by 0.05m, while $z_1=3m$.
3. The position of the first reflection element is represented by x_l, y_l, z_l . Start calculating the received power reflected from the first location of the first reflected element (here is ceiling) as shown in figure (3.3).
4. Calculating R_l and R_2 .
5. Find all the angles $\phi_1, \phi_2, \beta_l, \delta$.
6. Calculate the inverse of the received angle δ ($\text{acos}(\delta)$) that is represented by (receangle).
7. Compare the value of (receangle) with FOV.
8. If the receangle is less than or equal to FOV, calculate the received power (by using equation 2.15) of first-order reflection at this location.
9. Save it in the store.
10. Calculate the required time to travel from the TX to the RX.
11. Save it in another store.
12. Repeat steps from 4 to 11 to trace all locations of the first row of the first reflecting element by incrementing y_1 by 0.05m for each move. Increment x_1 by 0.05m to start calculation of the received power of the second row and so on.

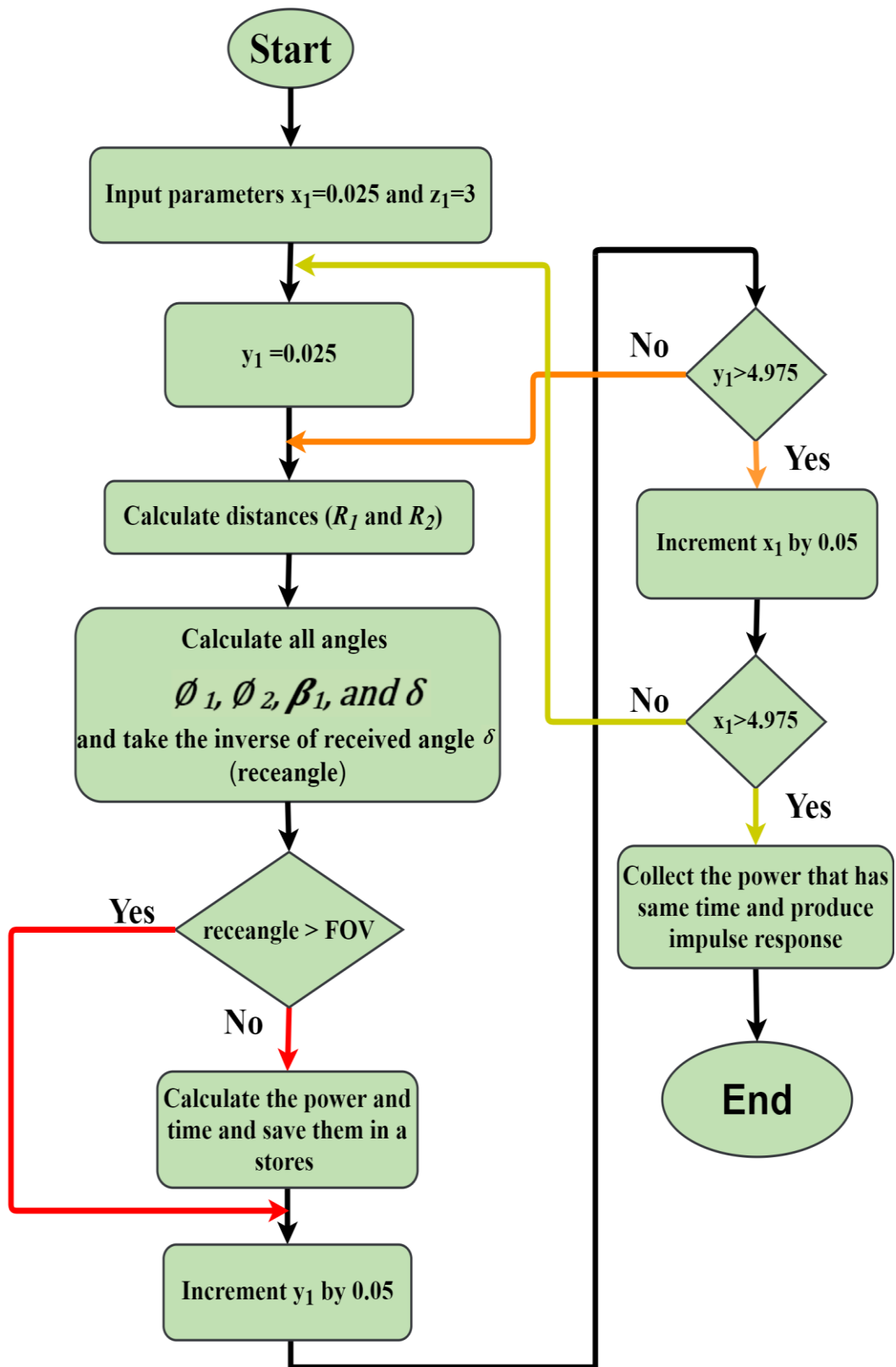


Figure (3.3): Flowchart of calculating first-order reflection received power from the ceiling.

13. After tracing all the points, collect the received power that contains the same time and produce an impulse response
14. Calculate the received power from the first wall by repeating all the steps from (2 to 13) and taking into account the change in the (for loop) as shown in figure (3.4). Where $y_1=0$ and x_1 and z_1 change in steps.
15. Repeat step 14 for the second wall and change y_1 from 0 to 5m.

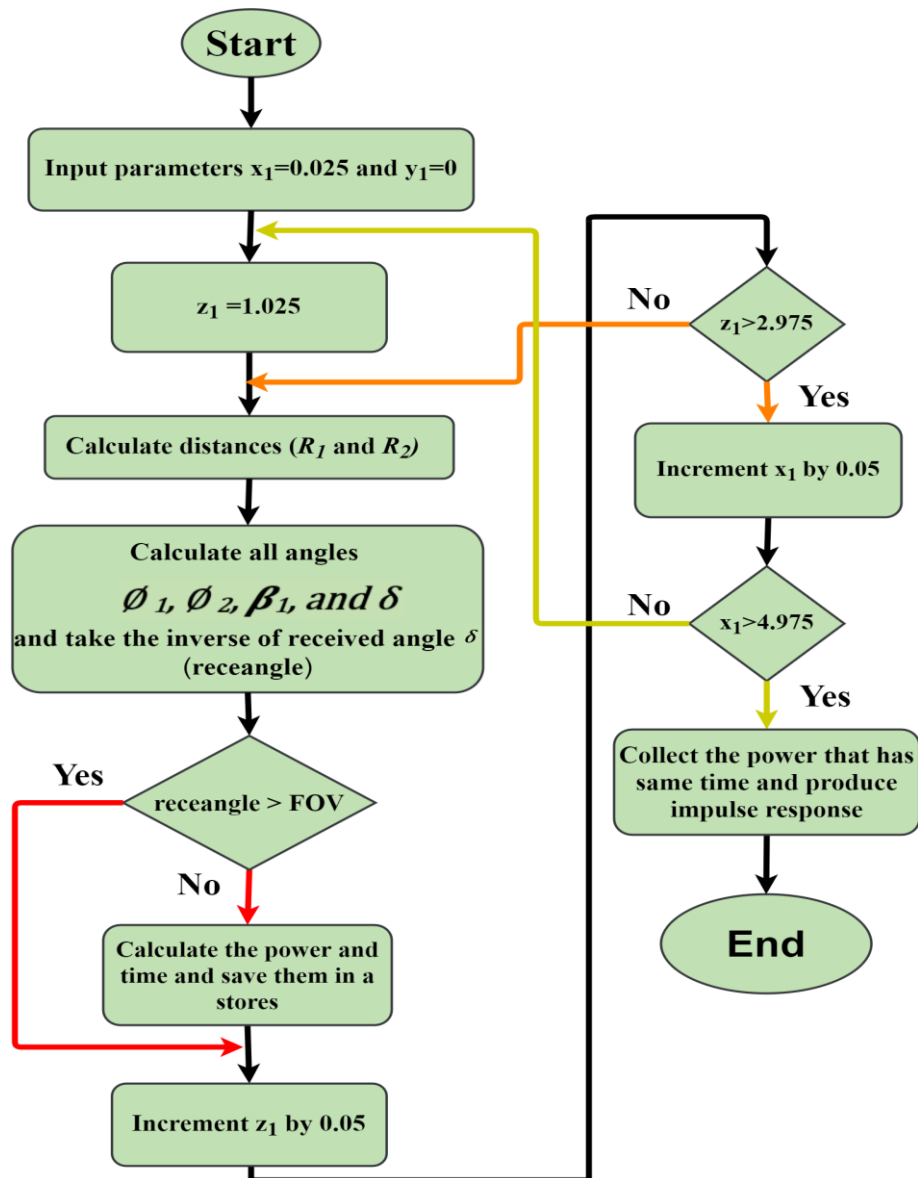


Figure (3.4): Flowchart of calculating first-order reflection received power from the first wall.

16. Repeat step 14 for the third wall and take into account the change in (for loop) where the y_1 is replaced instead of the x_1 , where the y_1 changes in steps and x_1 is constant and set to 0.
17. Repeat step 16 for the fourth wall and take into account the change in (for loop) where change x_1 from 0 to 5m.

3.4.1.2 Flowcharts of Calculating Second Order Reflection

After the calculation of the received power from the first reflection elements, we continue to calculate the received power reflected from the second reflection elements by following these steps.

1. Define all values that are required in equation (2.17) beside the definitions of first-order reflection, like dA_2 and Γ_2 to calculate the first reflection from the first reflecting element, then the rays reach the second reflecting element instead of reaching the RX. Finally, it reaches the RX. The location of the second reflective element is represented (x_2, y_2, z_2) .
2. To calculate the first reflection from the first reflecting elements (here the ceiling) and the second reflection (from the four walls), first, initialize x_1 and $y_1 = 0.05\text{m}$, $z_1 = 3\text{m}$. For calculating four walls, replace (x_1, y_1, z_1) with (x_2, y_2, z_2) . Where the initial value of x_2 is 0.1m, while z_2 is 1.1m, and the step of increment is 0.2m, $y_2 = 0$. From the flowchart shown in figure (3.5), we have four (for-loops); two for-loops to trace the first reflection elements (x_1, y_1, z_1) from the ceiling. and two to trace the second-order reflection elements (x_2, y_2, z_2) from the first wall.
3. First we start calculating the received power of the first location of the first reflection element and first location of the second reflective element.
4. calculating R_1, R_3 , and R_4 .

5. Find all angles $\phi_1, \phi_2, \alpha_1, \alpha_2, \beta_2, \delta$.
6. Calculate the inverse of received angle δ ($\arccos(\delta)$) that represented by (receangle).
7. Compare the value of (receangle) with FOV.
8. If the receangle is less than or equal to FOV, calculate the received power (by using equation 2.17).
9. Save it in the store.
10. Calculate the required time to travel from the TX to the RX.
11. Save it in another store.
12. Repeat steps from 4 to 11 to trace all locations of the second-order reflection for the first location of the first-order reflection by incrementing x_2 and z_2 by 0.2m as shown in figure (3.5).
13. Finishing all the calculations of the first location of the first reflection (ceiling) and the second reflection from four walls by repeating steps from 4 to 11 and taking the change of the x_2, y_2 and z_2 into account.
14. Moving to the second location (by incrementing y_1 by 0.05m and repeating steps from 4 to 13) until the complete first row at $x_1=0.025$ m.
15. Moving to the second row by incrementing x_1 by 0.05m and so on.
16. Complete all tracing of the first reflection from the ceiling and second order reflection from four walls by repeating the steps from 4 to 15, and collecting the received power that contains the same time and produces an impulse response.
17. Received power of the first reflection from the first wall and the second reflection from the ceiling and other three walls can be calculated by following the steps from 2 to 16 and taking the change displayed in figure (3.6) into consideration.

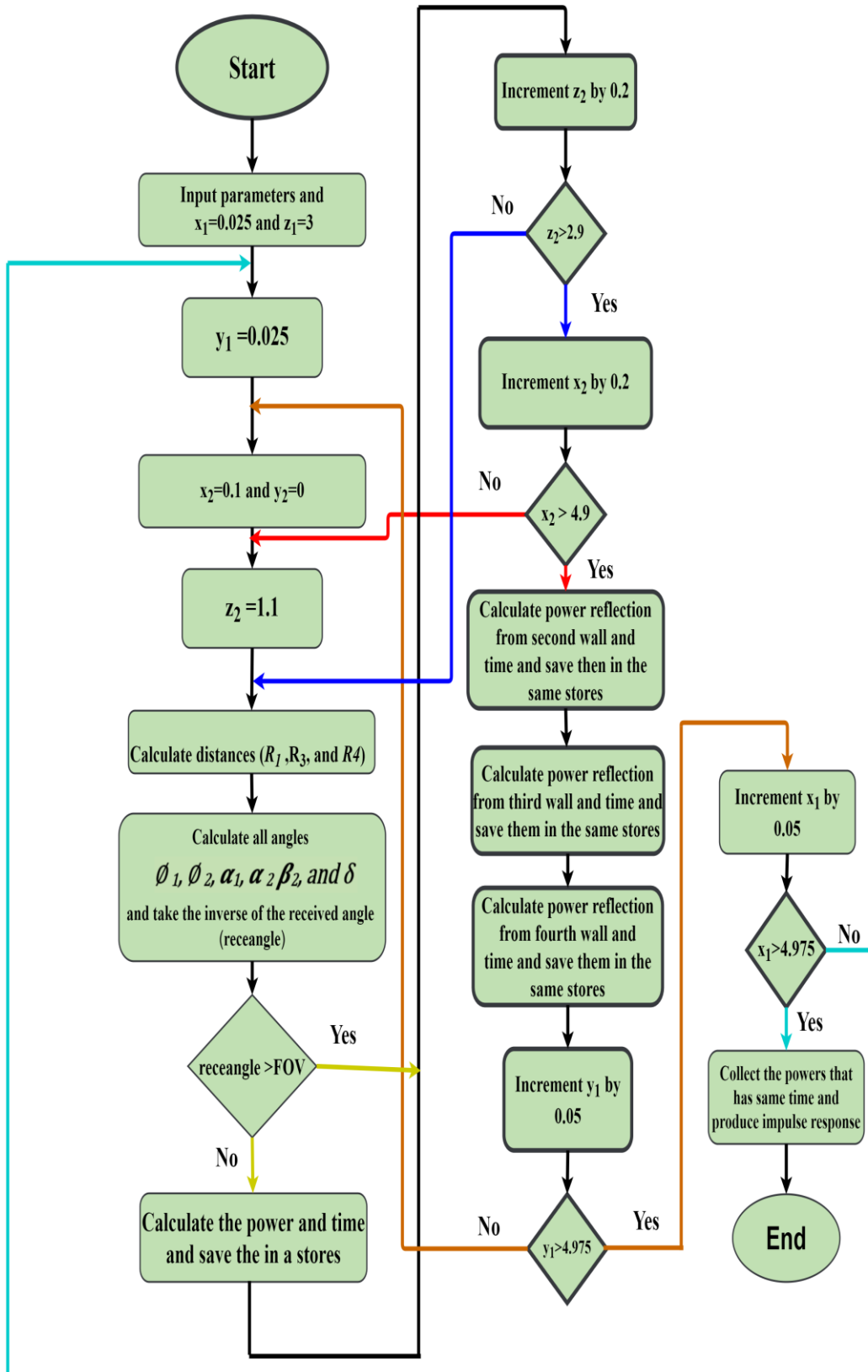


Figure (3.5): Flowchart of second order reflection (first reflection from the ceiling and second reflection from the four wall).

18. Received power of the first reflection from the second wall and the second reflection from the ceiling and other three walls can be calculated by following also the steps displayed in figure (3.6) and take into account change in the coordinate of reflective elements, here $y_1=5\text{m}$ instead of 0 and $y_2=0$ instead of 5m and following all the steps from 2 to 16.
19. While the calculation of received power of the first reflection from third wall and second reflection from other three walls and ceiling is the same steps shown in figure (3.6) but here y_1 is a change in steps and x_1 constant and equal to 0 and $x_2 =5\text{m}$ and following all the steps from 2 to 16.
20. Calculating the received power of the first reflection from the fourth wall and the second reflection from the other three walls and ceiling, but in this case, x_1 is equal to 5m and x_2 is equal to 0, and following all the steps from 2 to 16.
21. After complete calculation of second order reflection, collecting received power that have same time to produce impulse response for second-order reflection. Finally, collecting first and second-order reflections impulse response to produce total impulse response.
22. Note that this calculation is for one location of the RX and a specific value of FOV. In our case, where the RX has 100 locations, all the steps (first and second reflection) are repeated 100 times. These steps are also repeated when FOV is changed.

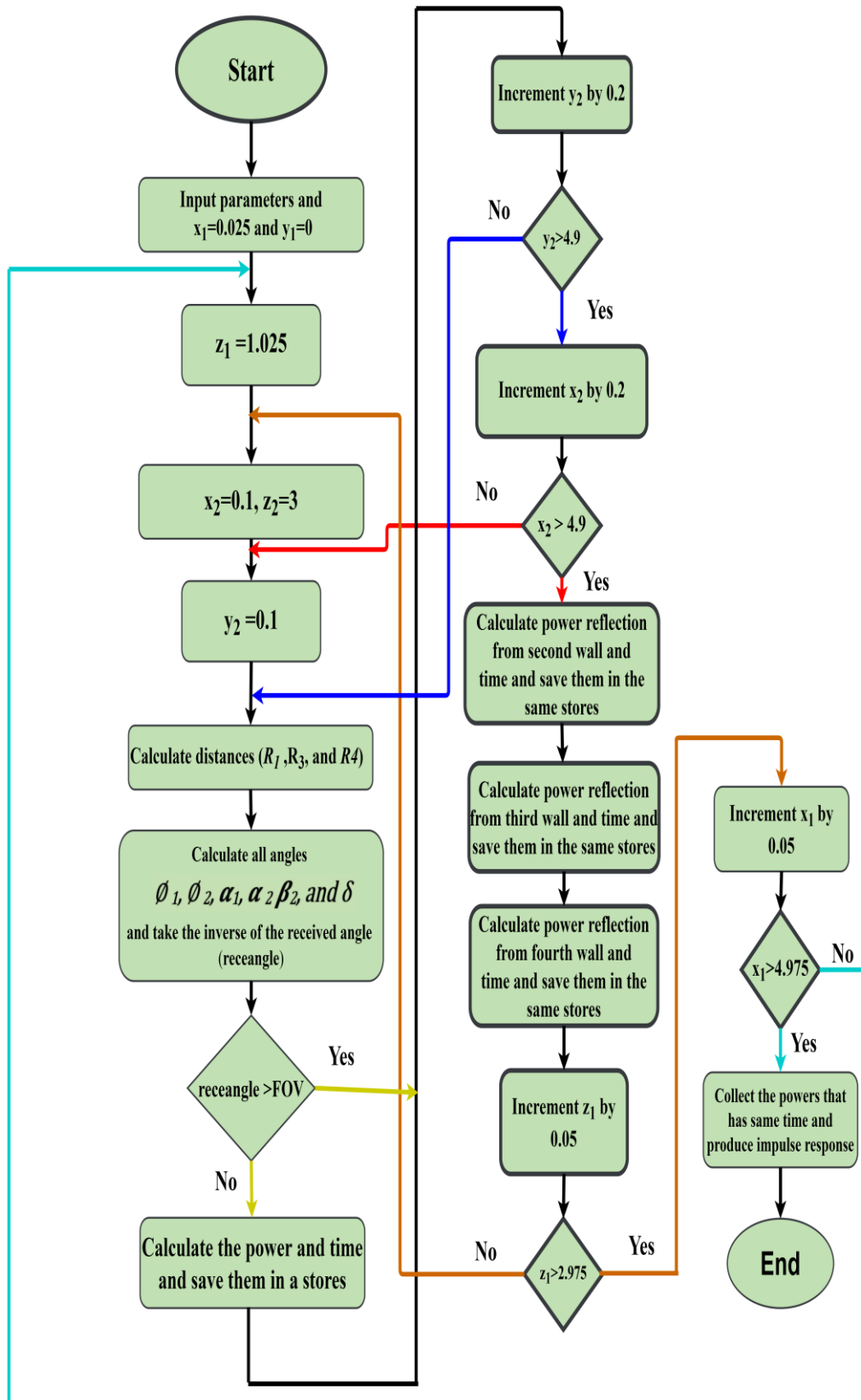


Figure (3.6): Flowchart of second order reflection (first reflection from the first wall and second reflection from the three walls and ceiling).

3.4.2 Flowcharts for Calculating Delay-Spread and Path loss

Figure (3.7) shows the steps of calculating delay-spread:

1. Repeat the steps in subsection (3.4.1) to produce an impulse response.
2. Calculate the delay-spread by using equation (2.21).
3. Save the value that was found in the store.
4. Repeat the steps (from 1 to 3) 100 times because we changed the location of the RX 100 times on the communication floor.

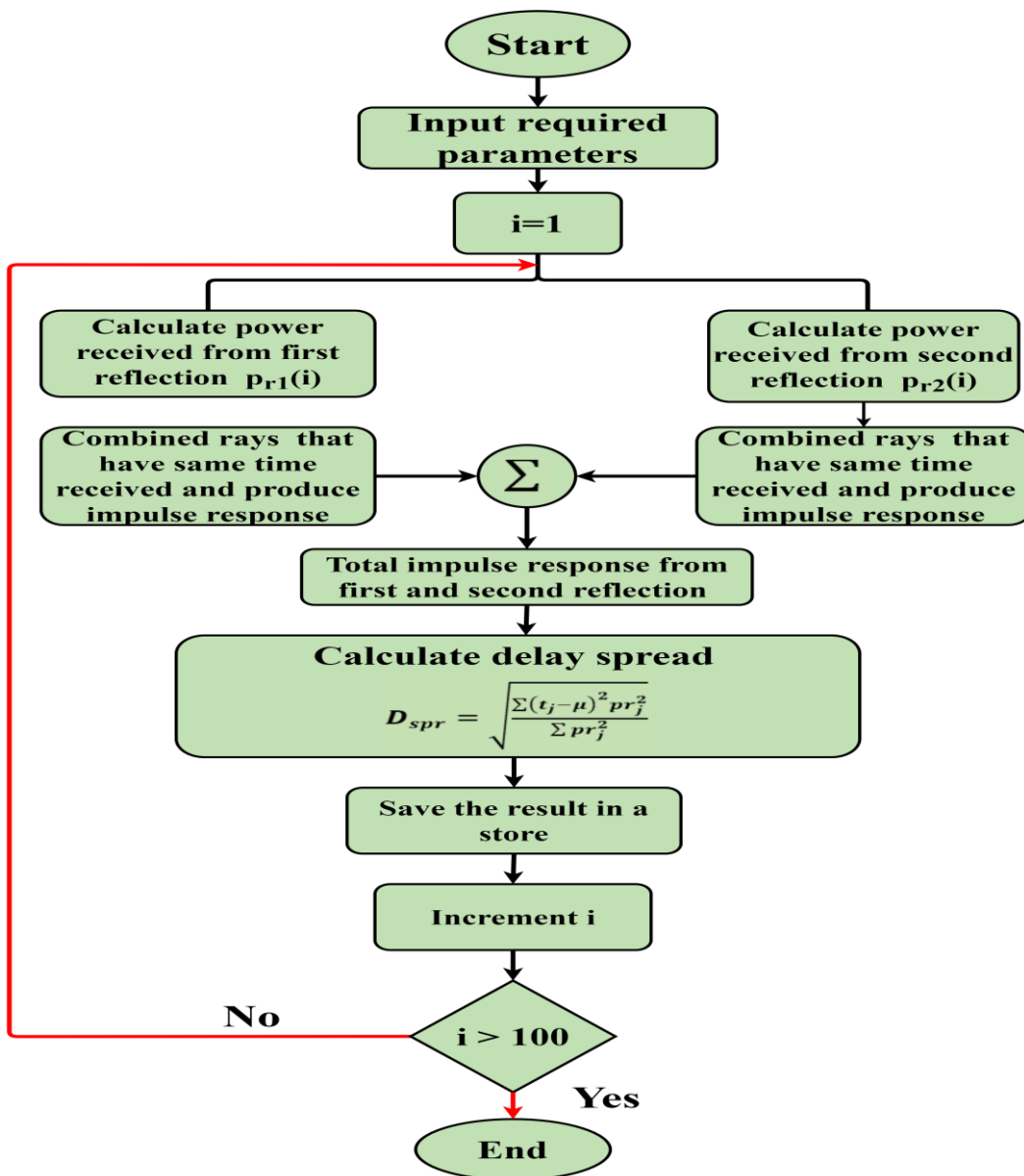


Figure (3.7): Flowchart for calculating the delay-spread.

5. The path loss calculated is the same as the steps used in the delay-spread except that in step 2 the equation used in calculating path loss is (2.32) as shown in figure (3.8).

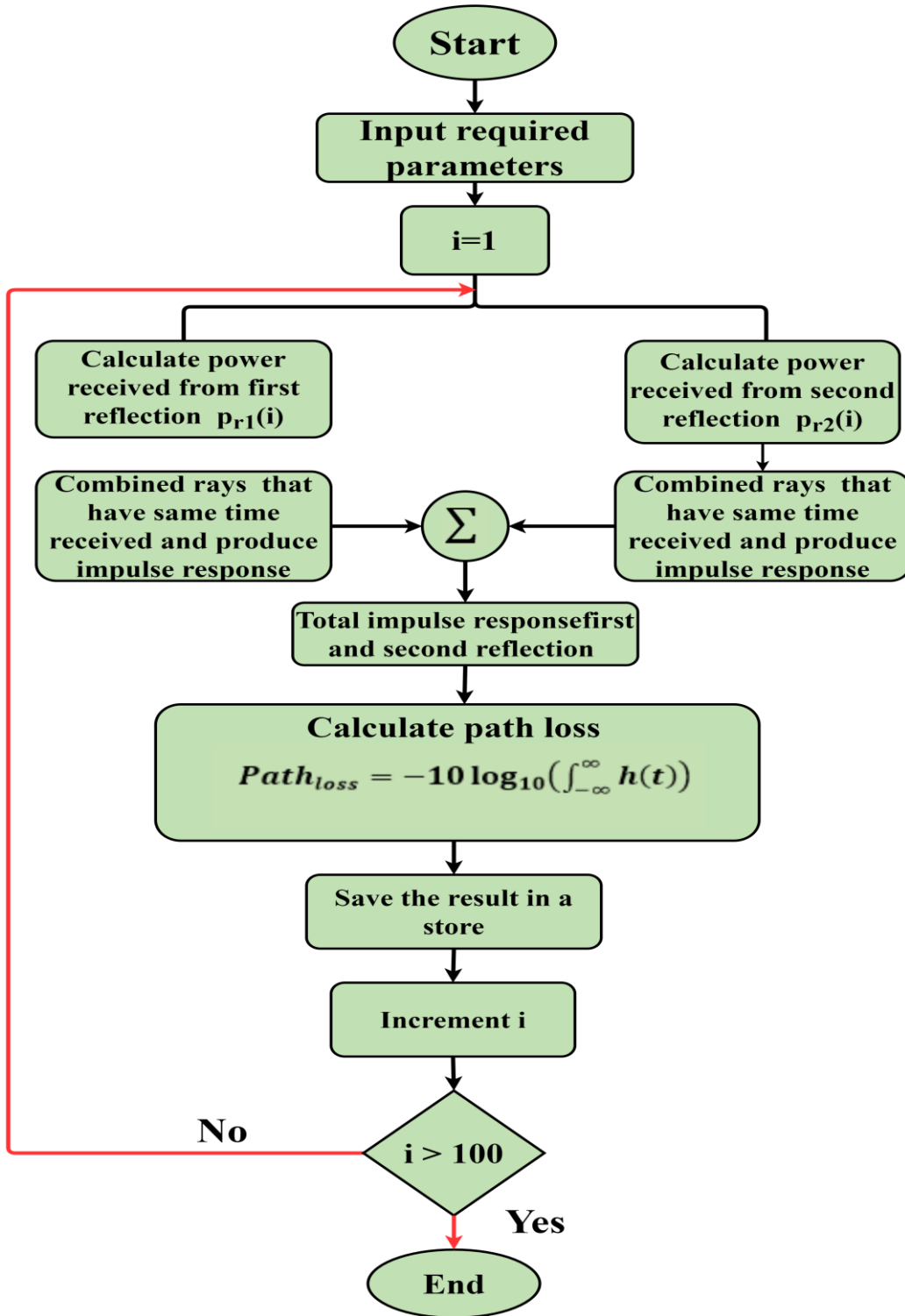


Figure (3.8): Flowchart for calculating path loss.

3.4.3 Flowchart for Calculating Channel Bandwidth

To calculate the channel's bandwidth and learn how much data may be transferred, follow the same steps of calculating delay-spread and path loss except that in step 2 the equation used in calculating channel bandwidth is (2.33) as shown in figure (3.9).

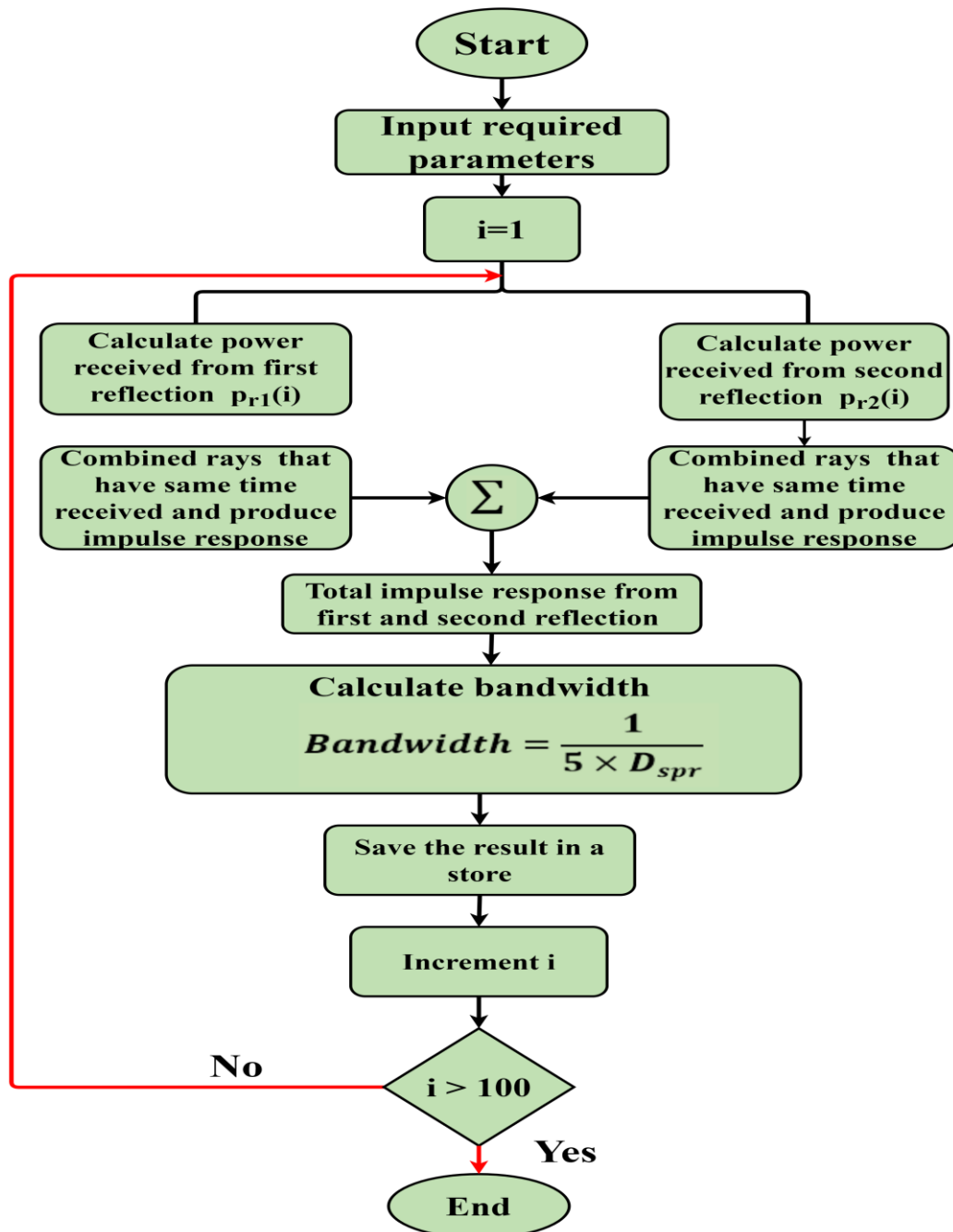


Figure (3.9): Flowchart for calculating channel bandwidth.

3.4.4 Calculation of Noise Power

In order to find the S/N by using MATLAB, we first need to write a code to find the background noise from the direct path, first and second reflections. The next sub subsections contain the flowcharts and the steps to calculate background noise.

3.4.4.1 Direct Path Noise Power

Figure (3.10) depicts the flowchart for finding the direct path noise power from each lamp.

1. Input the required parameters and note that the power of each lamp is 65w and the mode number is $n_{lamp}=33.1$. (x_{lamp} , y_{lamp} , z_{lamp}) represent the location of the lamp.
2. Calculate R_{dir} that represent the distance between the lamp and RX.
3. Find all the angles ϕ_l is a representation for the angle formed by the lamp's normal and the reflected ray R_{dir} and δ displays the angle between the incident ray R_{dir} and the RX normal.
4. Calculate the inverse of δ ($\text{acos}(\delta)$) that is represented by the receangle.
5. Compare the value of the receangle with the FOV.
6. If the receangle is less than or equal to FOV, calculate the received noise power (used equation 2.25) of the first lamp.
7. Sum the noise power with the previous noise power.
8. Repeat the steps from 2 to 7 to find the noise power for each lamp by incrementing x_{lamp} and y_{lamp} .

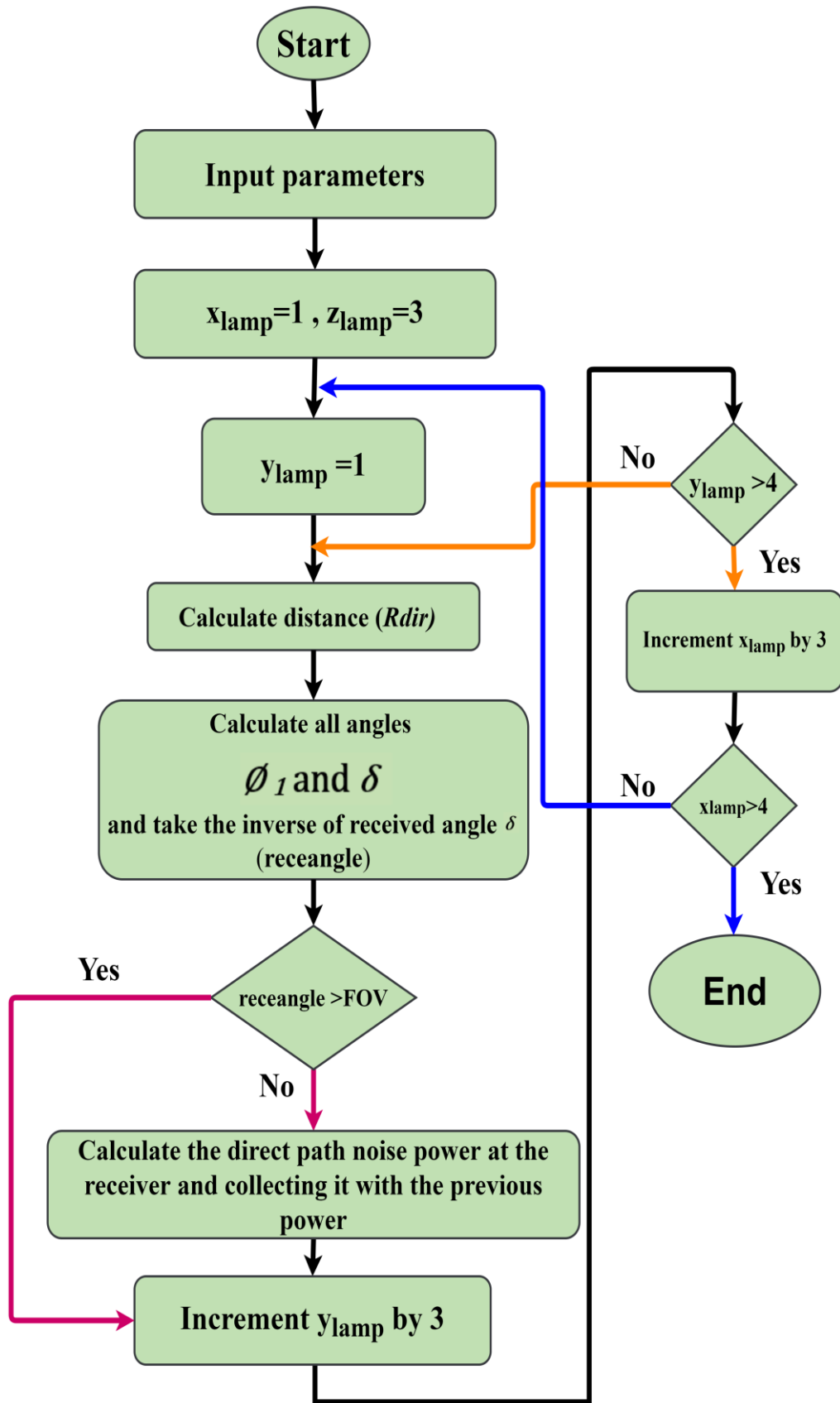


Figure (3.10): Flowchart for calculating direct path noise power.

3.4.4.2 First Order Reflection Noise Power

In the first order reflection, there is no reflection from the ceiling because the lamps are positioned on the ceiling, so only the reflection from four walls is calculated by following these steps:

1. To calculate the noise reflected power from the first wall, put $y_1=0$ and x_1 is changed in steps.
2. Calculate R_1 and R_2 .
3. Calculate the angle ϕ_1 is a representation for the angle formed by the lamp's normal and the reflected ray (R_1); ϕ_2 represents the angle between the incident ray (R_1) and the reflecting element's normal; β_1 represents the angle between the normal of the reflection element and reflected ray (R_2), and δ represents angle formed between incident ray (R_2) and the RX's normal.
4. Calculate the inverse of δ ($\text{acos}(\delta)$) that is represented by the (receangle).
5. Compare the value of the rectangle with the FOV.
6. If the receangle is less than or equal to FOV, calculate the received noise power of the first lamp (using equation (2.23)).
7. Sum the noise power with the previous noise power.
8. Repeat the steps from 2 to 7 to complete the tracing of the first wall by incrementing x_1 and z_1 as shown in figure (3.11).
9. Repeat the steps from 2 to 8 to find the noise power from all lamps for the first wall by incrementing x_{lamp} and y_{lamp} as shown in figure (3.11).
10. To calculate the noise reflected power from the second wall, put $y_1=5\text{m}$, x_1 and z_1 are changed in steps, and repeat the steps from 2 to 9.

11. To calculate the noise reflected power from the third wall, put y_1 instead of x_1 and change y_1 in steps and $x_1=0$. Repeat the steps from 2 to 9.

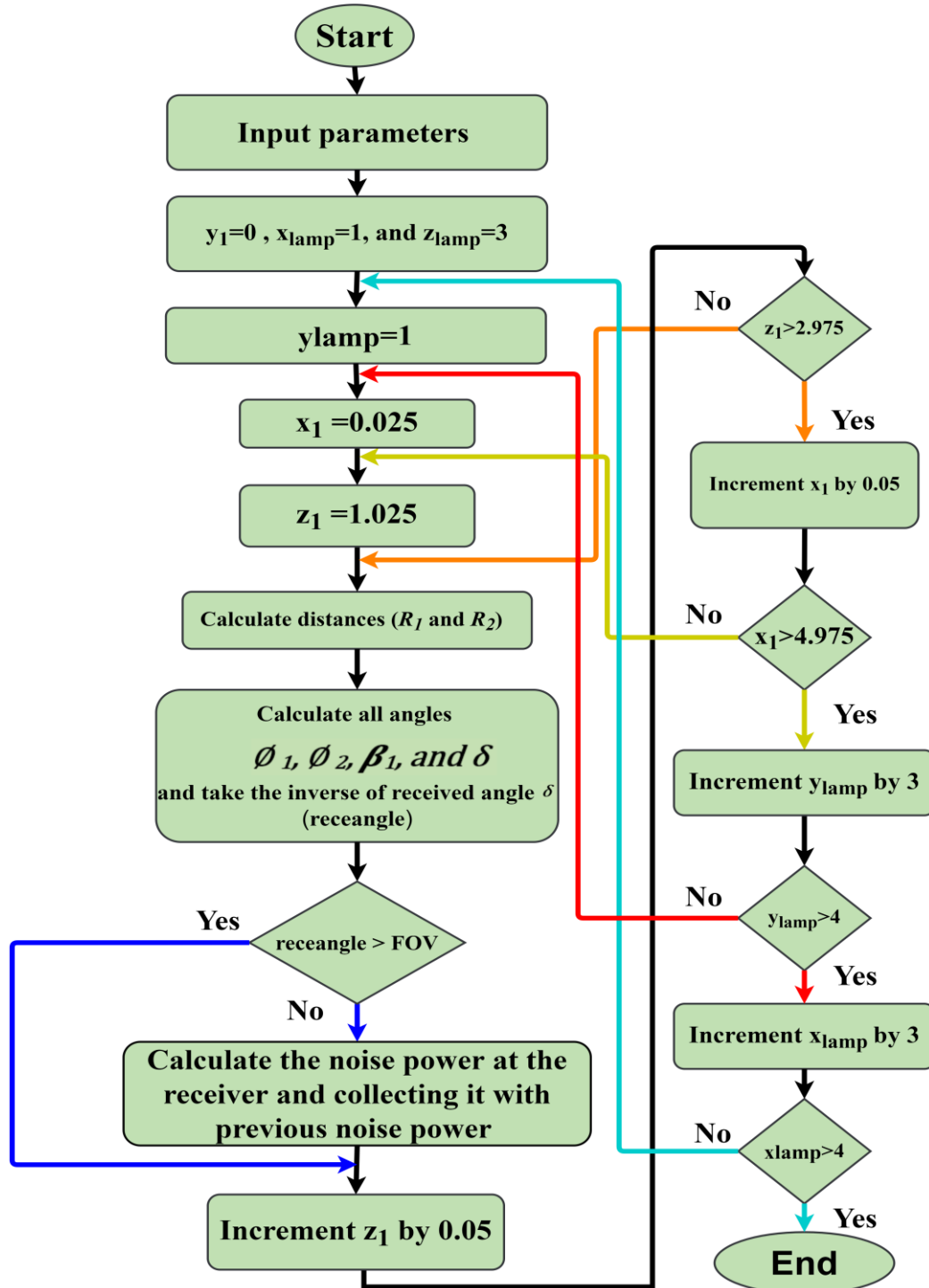


Figure (3.11): Flowchart to calculate the noise power of the first reflection from the first wall.

12. To calculate the noise reflected power from the fourth wall, put $x_1=5\text{m}$ and y_1 instead of x_1 and changed in steps. Repeat the steps from 2 to 9.

3.4.4.3 Second Order Reflection Noise Power

In the second order reflection, there is no first reflection from the ceiling because the lamps are positioned on the ceiling, so only the reflection from four walls is calculated, but there is a reflection from the ceiling in the second order reflection. By following these steps, the noise power can be calculated.

1. After the calculation of noise power from the first-order reflection and direct path is completed, we continue to calculate the second-order reflection. We start by calculating the first reflection from the first wall. Instead of reaching the rays to the RX, it reaches the second reflecting element (ceiling) and then reaches the RX. As shown in the flowchart that is represented in figure (3.12), we have (six for-loops): two for-loops to trace all lamps, two for-loops to trace the first reflection elements and two to trace the second-order reflection elements.
2. We start the calculation of the first lamp by putting $y_1=0$ and x_1 and z_1 are changed in steps and; $z_2=3\text{m}$ and x_2 and y_2 are changed in steps.
3. Calculate R_1 and R_3, R_4 .
4. Calculate the angle $\phi_1, \phi_2, \alpha_1, \alpha_2, \beta_2$, and δ .
5. Calculate the inverse of δ ($\text{acos}(\delta)$) that represent by (receangle).
6. Compare the value of receangle with the FOV.
7. If the receangle less than or equal to FOV calculate received noise power of the lamp using equation (2.24).
8. Sum the noise power with the previous noise power.

9. Repeat the steps from 3 to 8 to complete the tracing of the second-order reflection of the ceiling for first location of the first reflection from first wall by increment x_2 and y_2 as shown in figure (3.12).
10. Repeat the steps from 3 to 8 to complete the tracing of the second-order reflection of the three walls for first locations of the first reflection from first wall and take the change of x_2 , y_2 , and z_2 into consideration.
11. Repeat the steps from 3 to 10 to complete the tracing of the second-order reflection of the other three walls and ceiling for all locations of the first reflection from first wall and take the change of the x_1 , y_1, z_1 , x_2 , y_2 , and z_2 into consideration.
12. Repeat the steps from 3 to 11 to find noise power reflect from other lamps by incrementing in x_{lamp} and y_{lamp} .
13. Repeat the steps from 2 to 12 to calculate the first reflected noise power from the second wall and by putting $y_1=5m$ and $y_2=0$.
14. Repeat the steps from 2 to 12 to calculate the first reflected noise power from the third wall by putting y_1 instead of x_1 where is change in steps and $x_1=0$ and $x_2= 5m$.
15. To calculate the noise reflected power from the fourth wall, repeat the step 14 and put $x_1=5m$ and $x_2= 0$.
16. Finally, after all the calculations of noise power from direct path, first, and second order reflections, we sum these powers to get a single value that represents total background noise (p_{t_noise}).

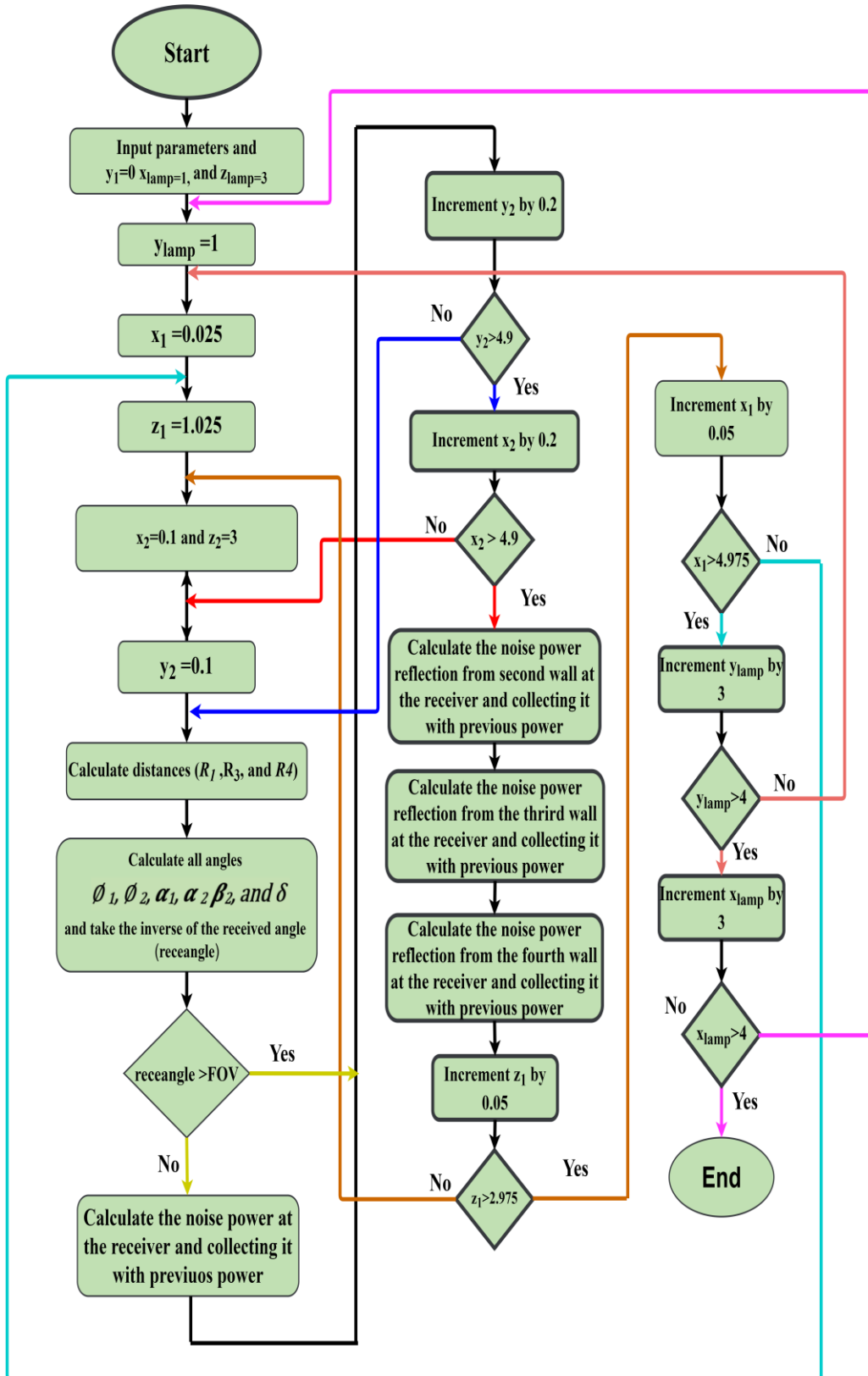


Figure (3.12): Flowchart to calculate the noise power of the first reflection from the first wall and second reflection from ceiling.

3.4.5 S/N and BER Calculation Flowcharts

The steps to compute S/N are shown in Figure (3.13).

1. Calculate the received power from 1st and 2nd order reflection by following all the steps found in subsection (3.4.1).
2. Calculate the background noise as shown in subsection (3.4.4) and calculate σ_{bn} .
3. Other noise, such as preamplifier noise σ_{pre} , should be calculated.
4. Find p_{s1} and p_{s0} and find noise associated with the signal σ_{sj} .
5. Find the S/N in ratio.
6. Find S/N in dB by taking a logarithm of it.
7. In the store, save the S/N value.
8. Repeat all the steps 1 to 7 for all RX locations.
9. Same steps of S/N from 1 to 5 and apply equation (2.31) to find BER as shown in figure (3.14).
10. Save the value in the store.
11. Repeat all the steps for all RX locations.

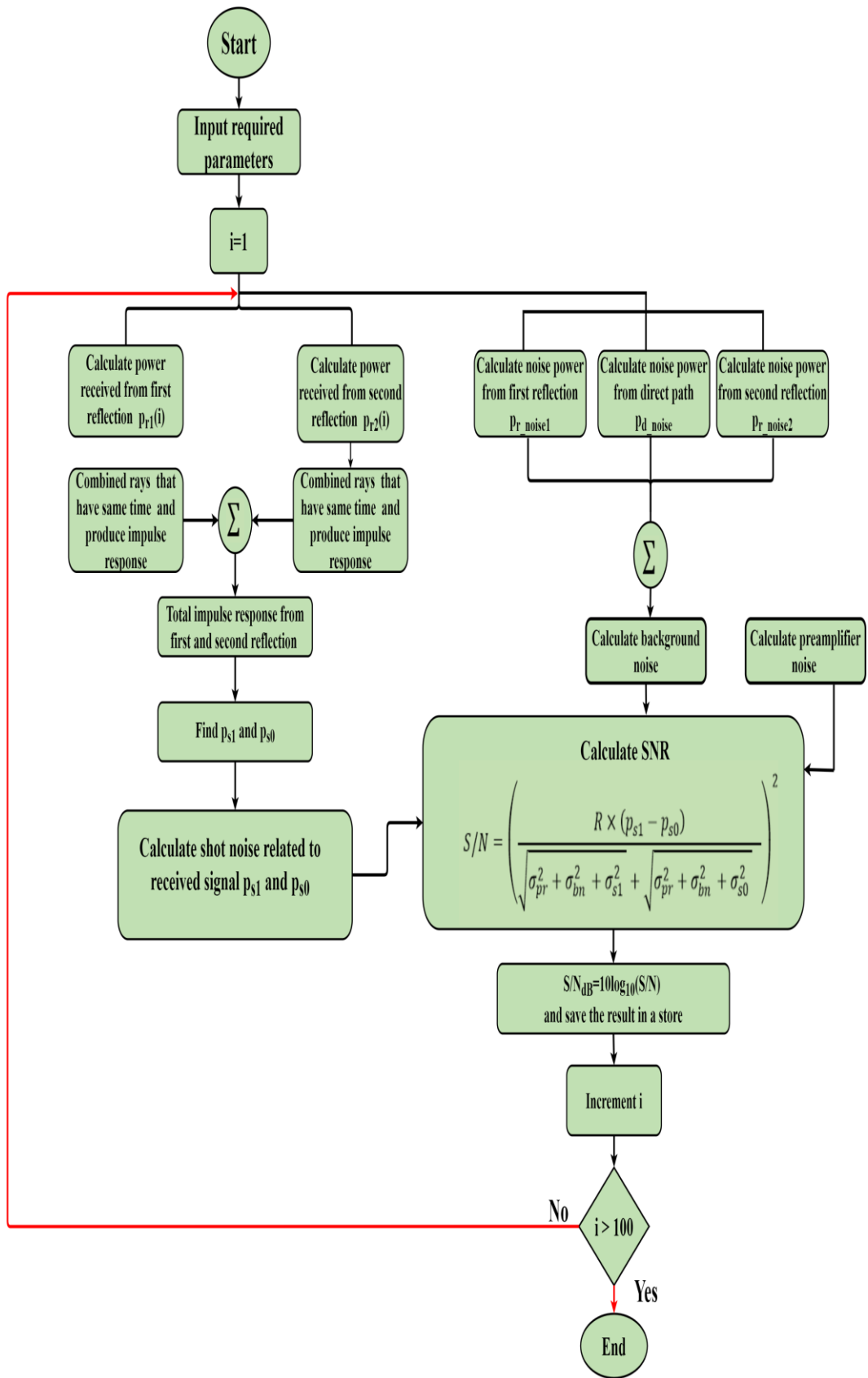


Figure (3.13): Flowchart of the S/N.

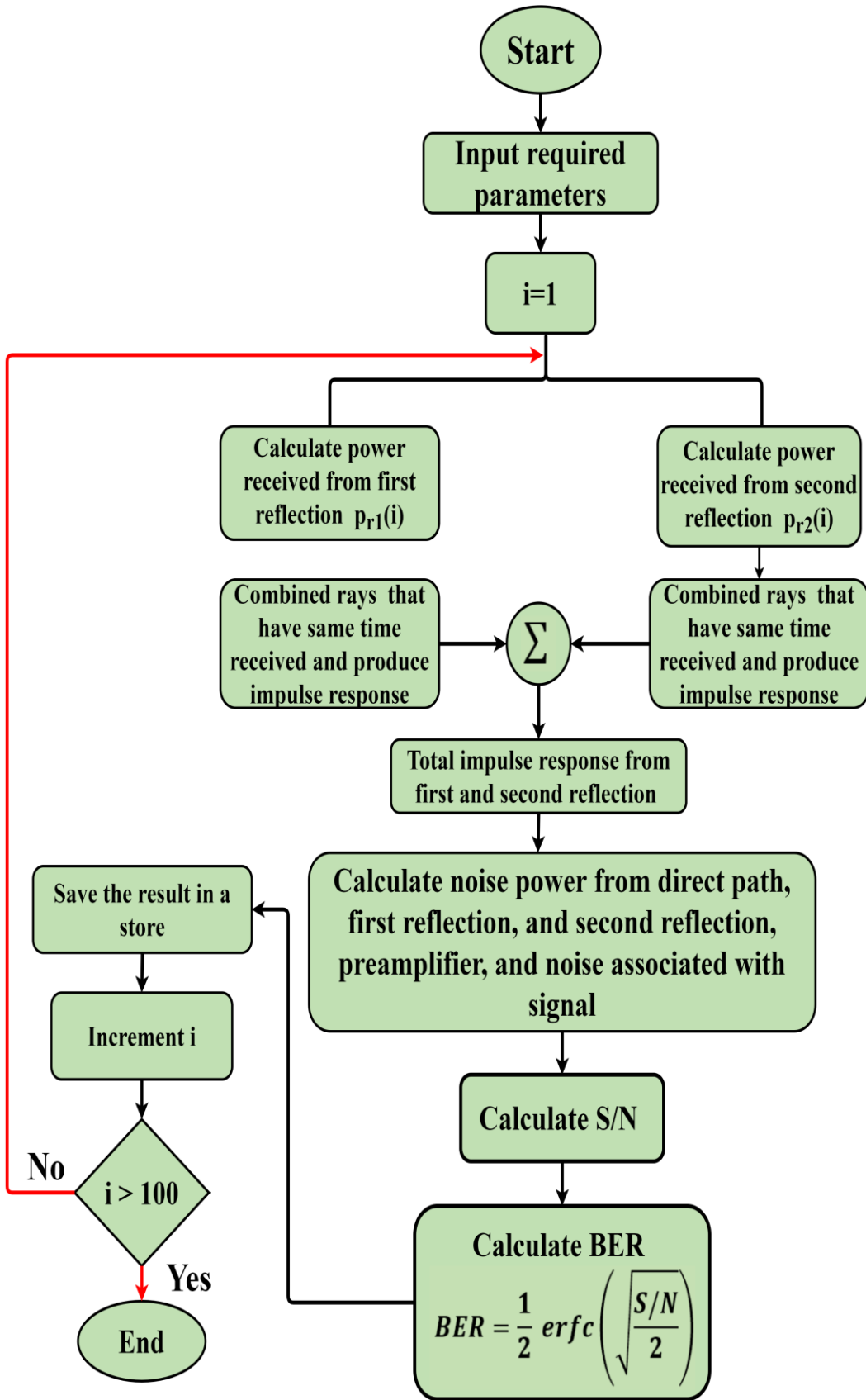


Figure (3.14): Flowchart of the BER.

3.5 Results of the Proposed System

The effectiveness of a suggested system in the presence of background noise, mobility, and multi-path is investigated. We considered many FOVs of the optical RX (FOV = 90°, FOV = 60°, FOV = 30°, and FOV = 10°). The TX was positioned in the center of the room (2.5m,2.5m,1m), and to get an accurate result, we assumed 100 random locations of the RX to give an overview of the system's performance, where x and y axes are variable randomly and z is constant at z=1m, and at each location, the impulse response was obtained. In addition, we used the impulse response to find the R.M.S delay-spread, channel bandwidth, path loss, BER, and S/N.

3.5.1 Impulse Response

To show the effect of the FOV of the RX on the system's work, the impulse response of the system was obtained for each change when the sender is in the center of the room (2.5m, 2.5m, 1m) and the RX is positioned in two separate positions in the room, one in the center (2.5m, 2.5m, 1m) and another on the side (1m, 1m, 1m), as shown in figures (3.15), and (3.16), respectively. As the RX is situated in the center of the room, the maximum power received is 0.15781 μW for FOV =90°, and 1.782 μW for FOV = 10°. On the other hand, as the RX is placed in the room's corner, the maximum power received is 0.1161 μW for FOV = 90° and 0.2816 μW for FOV = 10°. When the TX and RX are in the middle of the room, the maximum received power is related to the shortest distance between them; as a consequence, the rays travel a short path to reach the RX.

The figures also demonstrate that when the FOV decreases, the power received is increased. The R.M.S delay-spread decreases (represented by the narrow width of the pulse) because the range of rays that can be accepted by

the RX is limited and this lead to the possibility of increasing the transmission data.

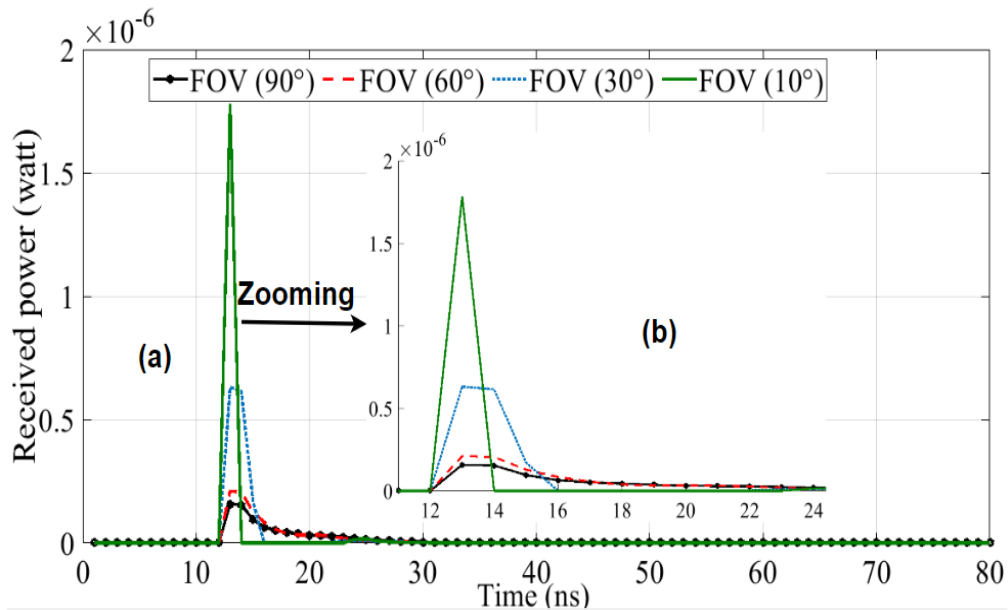


Figure (3.15): (a) Impulse response when the TX and RX positioned in the middle of the room; (b) Zooming of the impulse response of (a).

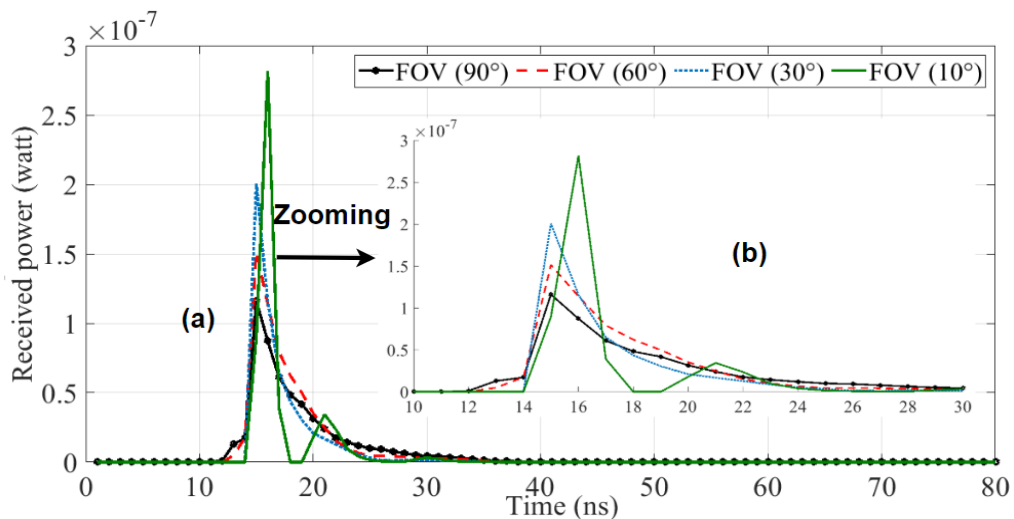


Figure (3.16): (a) Impulse response when the TX positioned in the middle of the room and RX placed in the corner; (b) Zooming of the impulse response of (a).

3.5.2 R.M.S Delay-Spread

Additional details on the geographic distribution of characteristics like RMS delay-spread, S/N, path loss, BER, and channel bandwidth may be obtained using CDF. The comparison is performed for several FOVs (90° , 60° , 30° , and 10°). Place the TX at the center of the room (2.5m, 2.5m, 1m) and the RX at 100 different locations chosen randomly on the communication floor ($z=1$ m). Because of multi-path reflection, the rays arrive at the RX through multiple pathways and different times, causing the pulse to spread. Figure (3.17) shows how R.M.S delay-spread may be measured with the CDF function and compared with different FOVs. The statistics show that the change in FOV has an impact on the R.M.S delay-spread.

When $FOV = 90^\circ$, the delay-spread for all RX locations exceeds 2 ns, reaching 2.297 ns for 60% of the entire location, whereas it can reach 0.637 ns when the FOV is set to 10° for 60% of the entire location. The delay-spread for all RX locations is less than 1.5 ns when $FOV = 10^\circ$. This implies that when the FOV becomes narrow, the delay-spread decreases because the reception rejects the rays that travel a lengthy trip to arrive at the destination

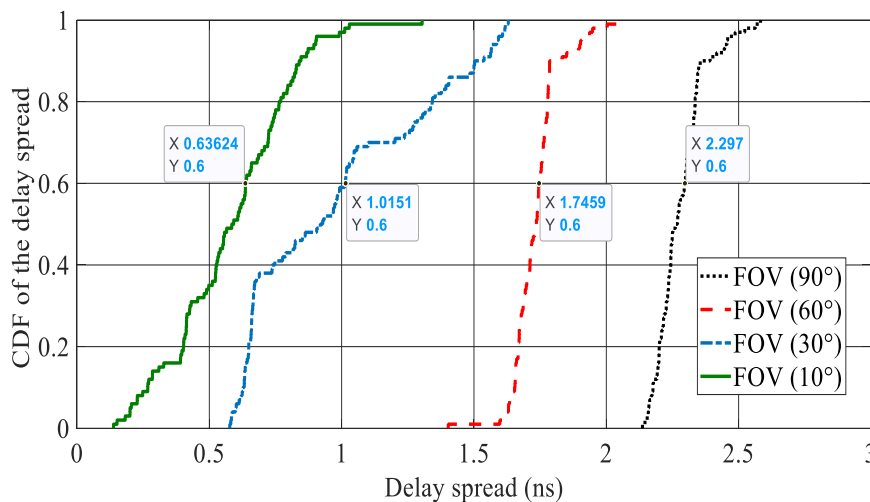


Figure (3.17): CDF of the delay-spread.

and fall at an angle larger than the FOV. The increase in channel capacity is because of the improvement in R.M.S delay-spread performance. From the figure, some locations have a high delay-spread and others have a lower delay-spread regardless of the value of FOV. This is because the distance between TX and RX leads to decreased delay-spread when it is short and vice versa.

3.5.3 S/N Analysis

The ambient light-induced shot noise weakens indoor OWC communications significantly. The most basic modulation method for the OWC system is O.O.K. A rectangular pulse of the same length as the bit period is used by O.O.K. Convolution of the impulse response with a rectangular transmitted pulse of 3 ns produced the pulse response. This corresponds to a bit rate of 308 Mbps. Furthermore, the pulse responses were evaluated across the whole communication floor. We employed a TIA developed in [97], and a noise current is $2.5 \text{ pA}/\sqrt{\text{Hz}}$. The CDF S/N result is shown in Figure (3.18), where the effect of the change in FOV has a significant impact on S/N when the system is operating under the effect of surrounding noise sources, RX noise, mobility, and multi-path dispersion.

When the FOV is reduced, the S/N improves. For 80 percent of total location, S/N reaches 4.91 dB for FOV of 90° , while S/N reaches 16 dB when FOV equals 10° . The reason for the low S/N is that the effect of noise on the signal is very high when the RX is beneath the lamps and away from the TX, whereas other locations have a high S/N due to two factors: first, the spacing between the TX and the RX is shortest (at this RX location) compared to other regions, resulting in a strong received signal. Second, because the RX is not illuminated, the noise effect is extremely low. The figure shows that when FOV becomes narrow, S/N is improved because the narrow FOV rejects more rays of the background noise at all locations of the RX. Also

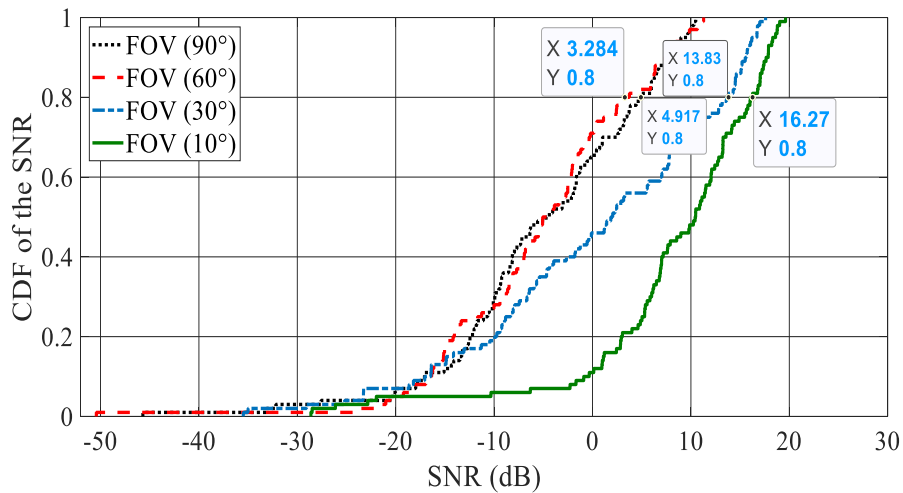


Figure (3.18): CDF of the S/N.

note that the S/N for both FOV 90° and 60° is overlapping because the angle for both of them is large enough to receive background noise where in some locations the effect of the spotlights is very high for one of the FOV and low for the other FOV and vice versa.

3.5.4 Bit Error Rate

The BER is related to the S/N where the rate of receiving error bits is decreasing as the S/N increases and this leads to the possibility of increasing the transmission data rate. Figure (3.19) shows that when FOV is decreased, S/N is increased consequently BER decreases. When the FOV is 90 degrees BER for 50% of the entire RX site reaches 0.273, while when the FOV is 10 degrees, the BER reaches 4.4×10^{-4} . The lowest BER that is available when the FOV is adjusted to 10°. As a result, FOV must be reduced to achieve a minimum BER and increase in the transmitted data rate.

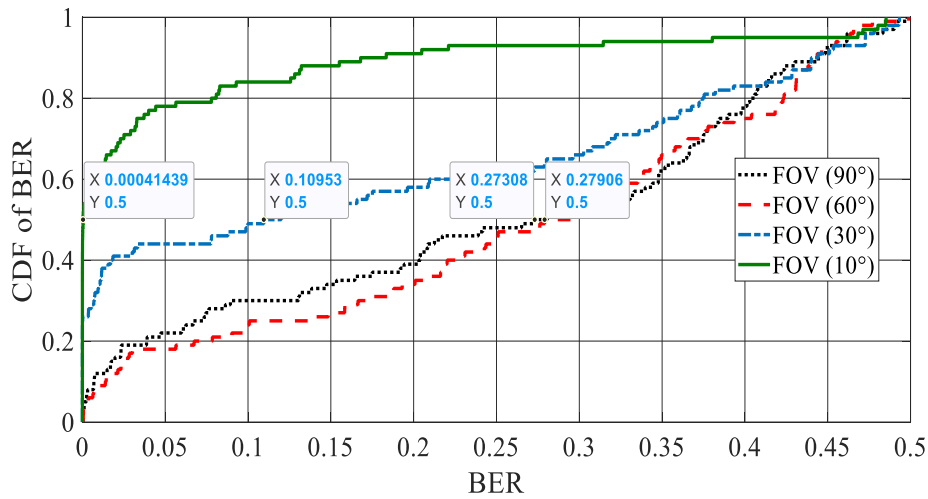


Figure (3.19): CDF of the BER.

3.5.5 Channel Bandwidth and Path Loss

Channel bandwidth determines the amount of the data rate that can be transmitted, so the wider the bandwidth channel, the more data can be transmitted. According to figure (3.20), when the FOV is at 90°, the channel bandwidth hits 89 MHz for 60% of the whole RX location, whereas it reaches 378.07 MHz when the FOV is at 10°. When FOV drops, bandwidth increases because R.M.S delay-spread is minimized as a result of refusing to accept

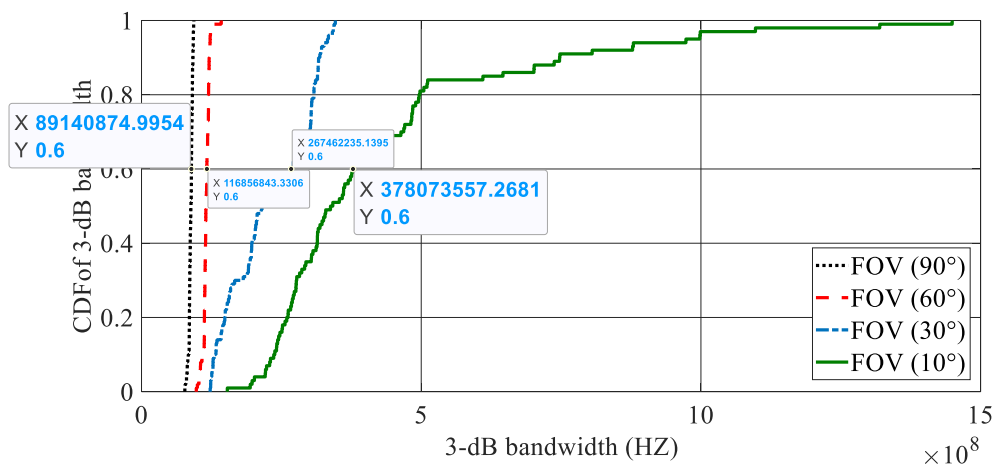


Figure (3.20): CDF of the channel bandwidth.

the rays that take the lengthy path to reach the RX, there is an inverse relationship between bandwidth and delay-spread.

Path loss is a measure of the amount of the attenuated signal due to the path that it takes to reach the RX. The more path loss, the less power is received. Path loss affected by FOV variation; figure (3.21) shows that for 50% of the total RX location when $FOV = 90^\circ$, path loss reaches 61.9 dB, and 61.32 dB when $FOV = 10^\circ$. We notice from the figure that the path losses for different FOVs overlap because the receiving power of a particular FOV is close to the receiving power of another FOV.

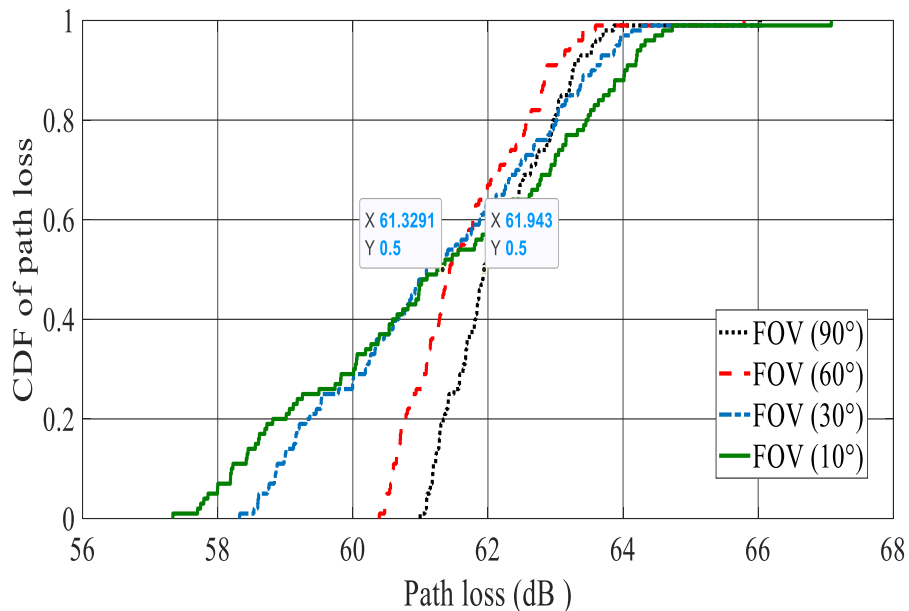


Figure (3.21): CDF of the path loss.

CHAPTER FOUR

ANGLE DIVERSITY RECEIVER (MULTI DETECTORS) FOR INDOOR OWC SYSTEM

4.1 Introduction

One of the best methods for combating the negative effects of multi-path dispersion and ambient light noise is diversity receiver. The detectors of ADR can spatially exclude unwanted signals, lowering the effects of ambient light noise and multi-path dispersion considerably [91]. The signal gathered from each branch detector is processed independently in an optical RX with numerous branches to create the final output electrical signal. For the sake of simplicity, SBC is used to process the generated electrical signals [12].

This chapter includes flowcharts that assist in calculating the parameters and comparing the proposed system utilizing ADR and CDS system while taking into account ambient noise and multi-path dispersion when the RX is traveling along the x-axis at $y = 1\text{ m}$ and 2 m .

4.2 The Proposed System Configuration

To investigate the effects of using wide beam transmission with ADR on the performance of the indoor OWC system and compare it with CDS. Simulations were created using a room with a dimension of $5\text{ m} \times 5\text{ m}$ (length and width) with a 3 m height ceiling for the configuration as seen in figure (4.1), where the reflectivity of the walls and ceiling is 80%. Previous studies have demonstrated that plaster walls reflect light rays in a Lambertian function-like pattern [87]. As a result, Lambertian reflectors were used to represent reflecting elements. The reflecting elements were created by splitting the room's reflecting surfaces (walls and ceiling) into a series of

square-shaped reflection elements of equal size. These elements were represented as Lambertian reflectors ($n = 1$) and operated as secondary emitters. According to earlier studies, the received optical power is only a little affected by third-order and higher reflections [87], [88] As a result, this study considers reflections up to the second order.

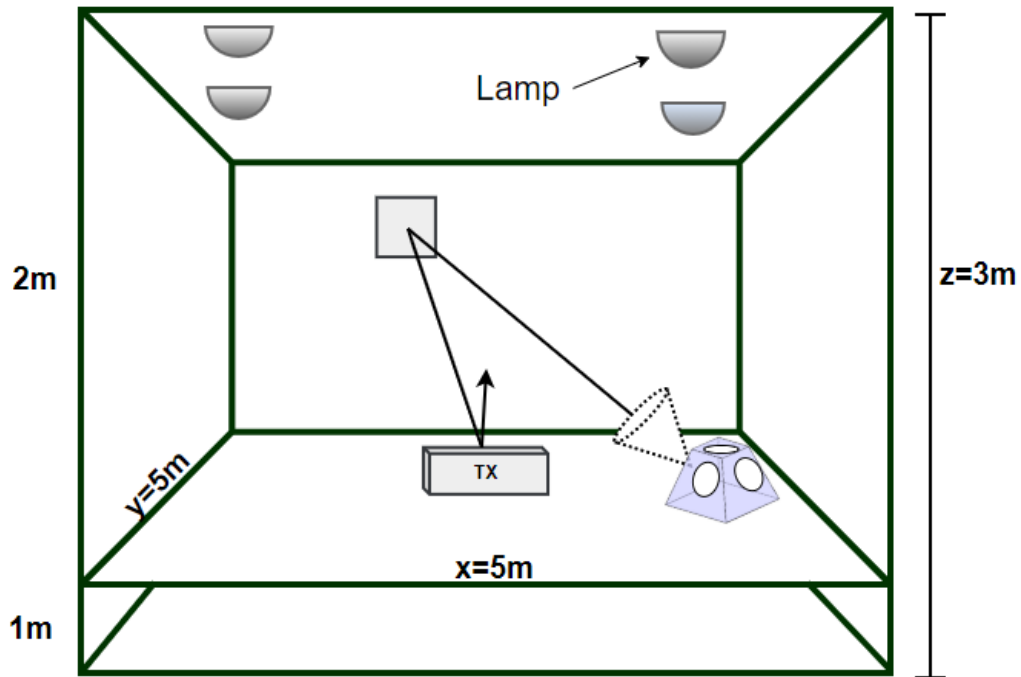


Figure (4.1): Dimension of the modelled room.

For the configurations studied, 5 cm x 5 cm surface elements for first-order reflections (dA_1) and 20 cm x 20 cm surface elements for second-order reflections (dA_2) were employed (CDS and our proposed system). These parameters were chosen to keep the computation within a suitable duration and measurement range. The TX was located in the central of the room on the communication floor (2.5m, 2.5m, 1m), aimed upwards, and it generates (1 W) total optical power with a perfect Lambertian radiation pattern to preserve skin and eyes when simulating both the CDS and the proposed system. Because the TX and RX are both on the communication floor. The direct path is absent between them, so only reflected rays reach the RX, so the received signal is affected by the multi-path. The ADR is positioned in

different places. As a result, the experiment will be conducted under the impact of mobility, background noise, and multi-path dispersion.

The detectors are installed on the square pyramid frustum faces, as seen in figure (4.2). The square pyramid frustum detector diversity system consists of five detector branches. Each ADR and CDS detector has a photosensitive area of 10 mm^2 and an $R=0.5 \text{ A/W}$. The area of the photodetector is chosen to be small in order to increase the bandwidth of the

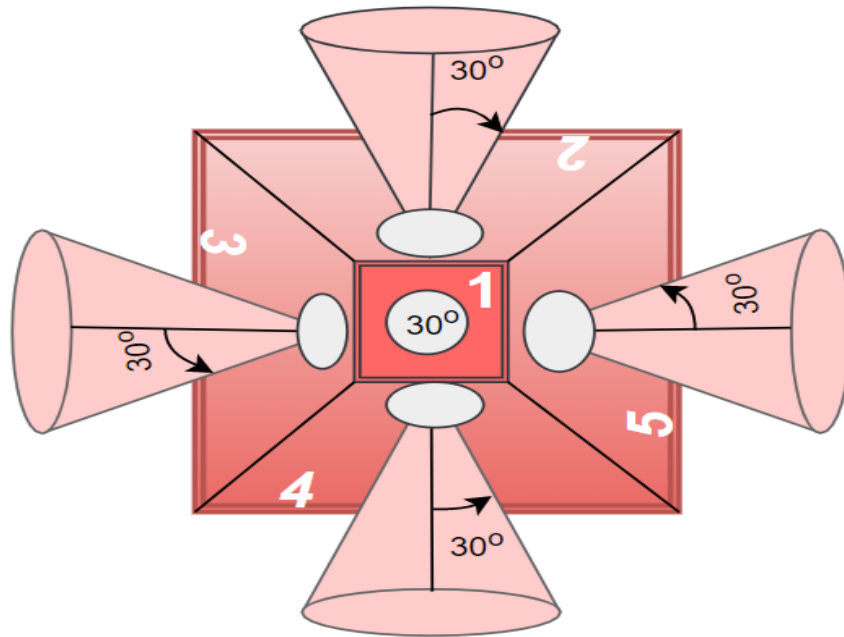


Figure (4.2): Structure of the angle diversity receiver.

RX, which leads to increased data transmission because there is an inverse relationship between the area of the photodetector and bandwidth. When the area is increased, the capacitance of the photodetector also increases. As a consequence, the bandwidth is decreased, as seen in the equation that is present in section (3.3). Each branch follows a specific path that may be identified by two angles: (Az) and (El) angles. Four detectors were distributed among the four square pyramid sides; hence the azimuth angles of the detectors were determined by dividing 360 by 4. As a result, the Az angles for the detectors were $AZ_1=0^\circ$, $AZ_2=90^\circ$, $AZ_3=180^\circ$, $AZ_4=270^\circ$, and

$AZ_5=360^\circ$. The photodetectors' EL was optimized and configured to generate a high S/N, with $EL_1=90^\circ$, $EL_2=65^\circ$, $EL_3=55^\circ$, $EL_4=65^\circ$, and $EL_5=55^\circ$. For a fair comparison, any three narrow FOV photodetectors of an ADR are selected, which when combined produce the same FOV and coverage area as a single detector RX (FOV = 90°). As a result, all photodetectors' FOVs were set to FOV = 30° .

In our systems, four spotlights PAR38 are used as noise sources to explore the influence of background noise on the intended signal, assess the system's S/N, and look into the benefits of having an ADR to reduce this effect. Each lamp radiates a (65 w) optical power in the form of a narrow beam-width, which is represented as a Lambertian radiant intensity of order $n_{lamp}=33.1$ for $h_{psa}=11.7^\circ$ [30]. The spotlights are situated at (1 m, 1 m, 3 m), (4 m, 1 m, 3 m), (1 m, 4 m, 3 m), and (4 m, 4 m, 3 m) on the ceiling. These bulbs produced a bright environment. For comparison, the same bulbs are used in CDS. This work does not account for the impact of sunlight coming in via windows.

4.3 Calculations in ADR

In ADR, we have five detectors, and each detector will calculate its parameters for each location and compare the results to choose the detector that has the best value. The next subsections contain flowcharts for calculating impulse response, 3dB channel bandwidth, S/N, delay-spread, and BER.

4.3.1 Flowchart for Calculating Impulse Response

The steps used to calculate received power from 1st and 2nd order reflections and produce impulse response are the same as those described in chapter three (subsection (3.4.1)) but using equations (2.43) and (2.44). Where the impulse response for each detector is calculated (as shown in

figure (4.3)) and the detector with the highest received power is chosen. This calculation is for one location of RX and TX. When the RX or/and TX changes its locations, all the steps shown in figure (4.3) are repeated.

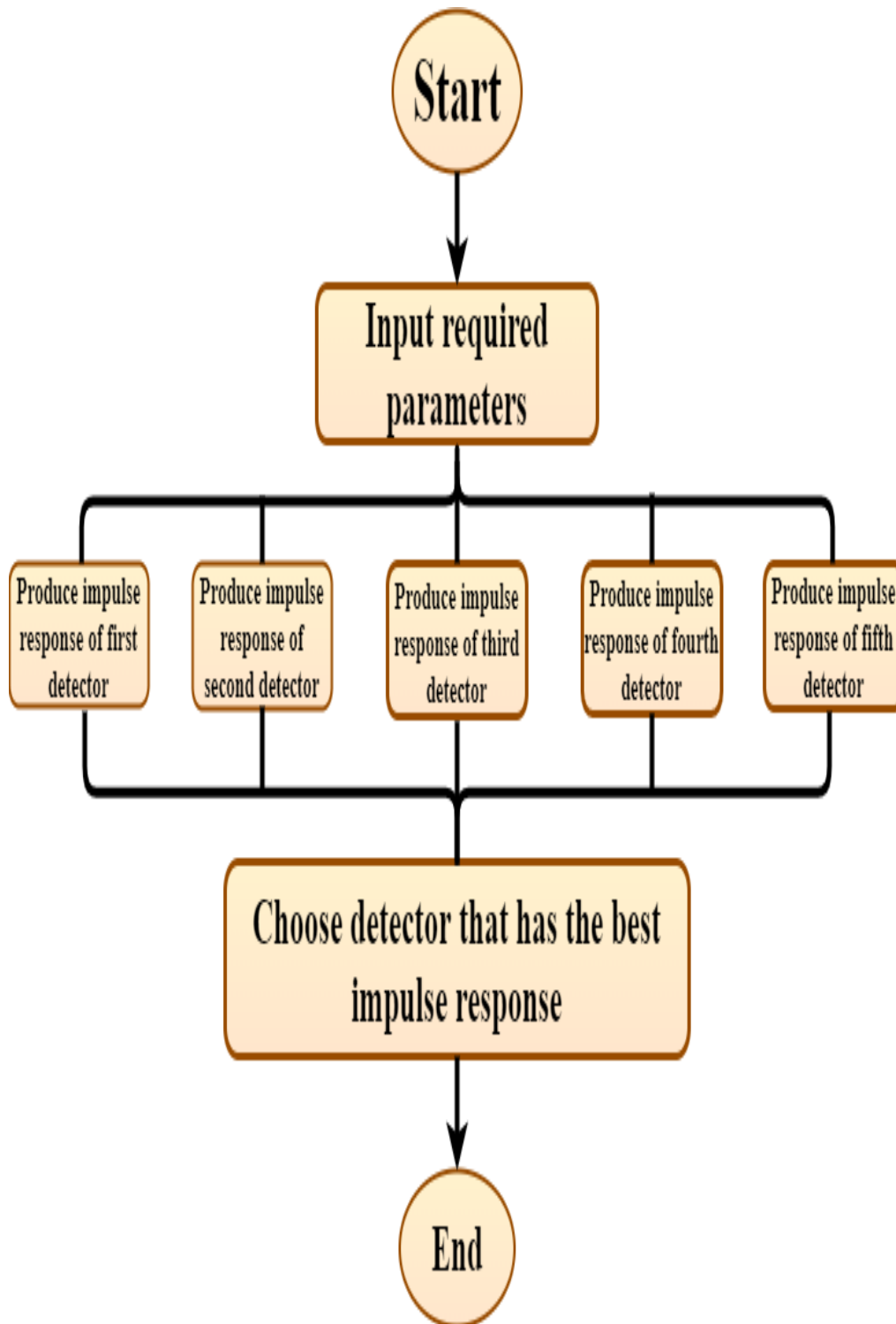


Figure (4.3): Flowchart for calculating the impulse response.

4.3.2 Flowcharts for Delay-Spread and Path Loss Calculation

To find the minimum delay-spread and path loss at all locations of the RX, follow these steps as shown in figures (4.4) and (4.5) respectively.

1. Using the procedures in subsection (3.4.1), determine the received power of first-order and second-order reflection for the first detector.

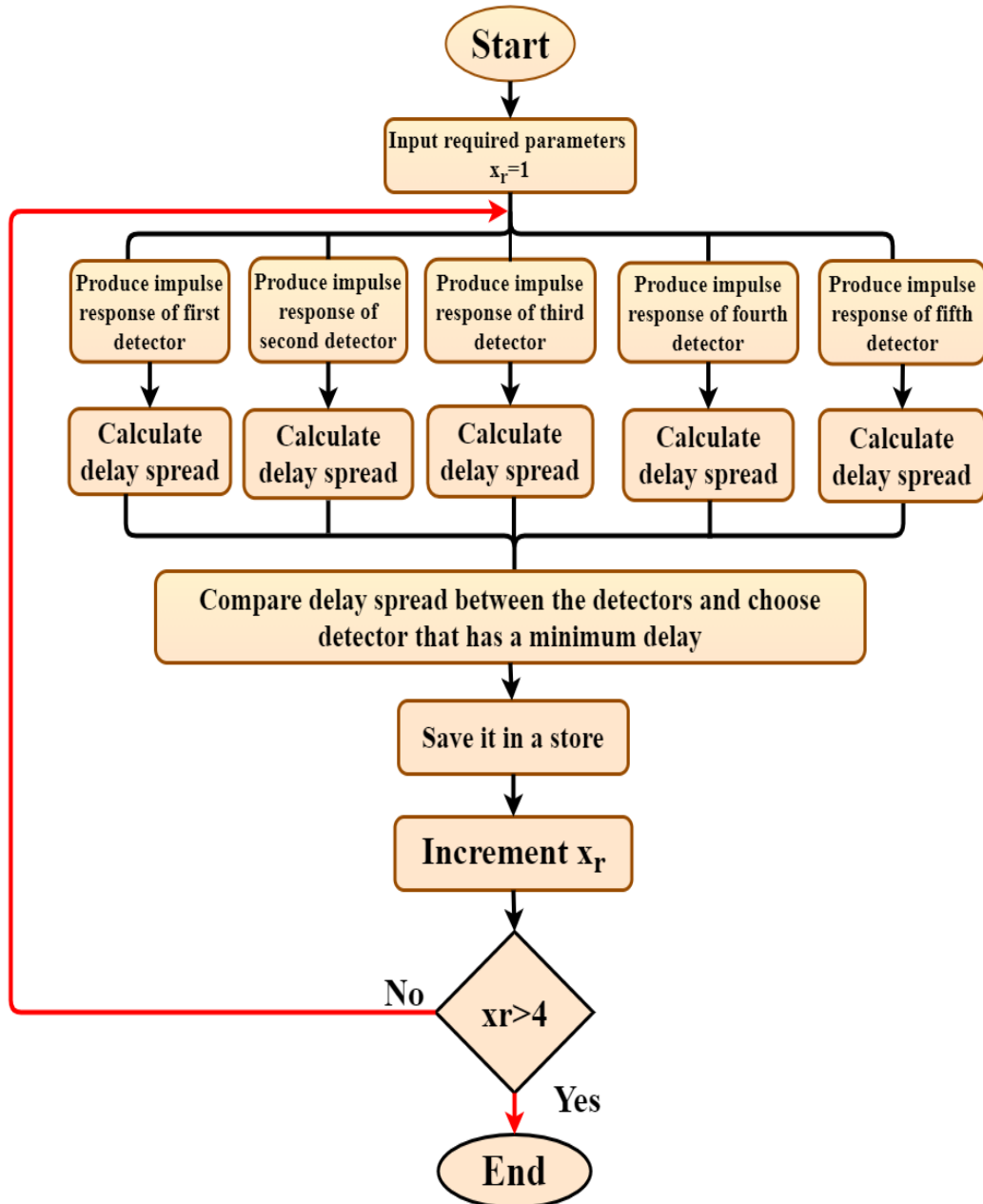


Figure (4.4): Delay-spread flowchart.

2. Collect the received power that have same time and produce an impulse response.
3. By using equation (2.21), the delay-spread is calculated and saved it in a store.
4. Repeat the steps from 1 to 3 for the other four detectors.

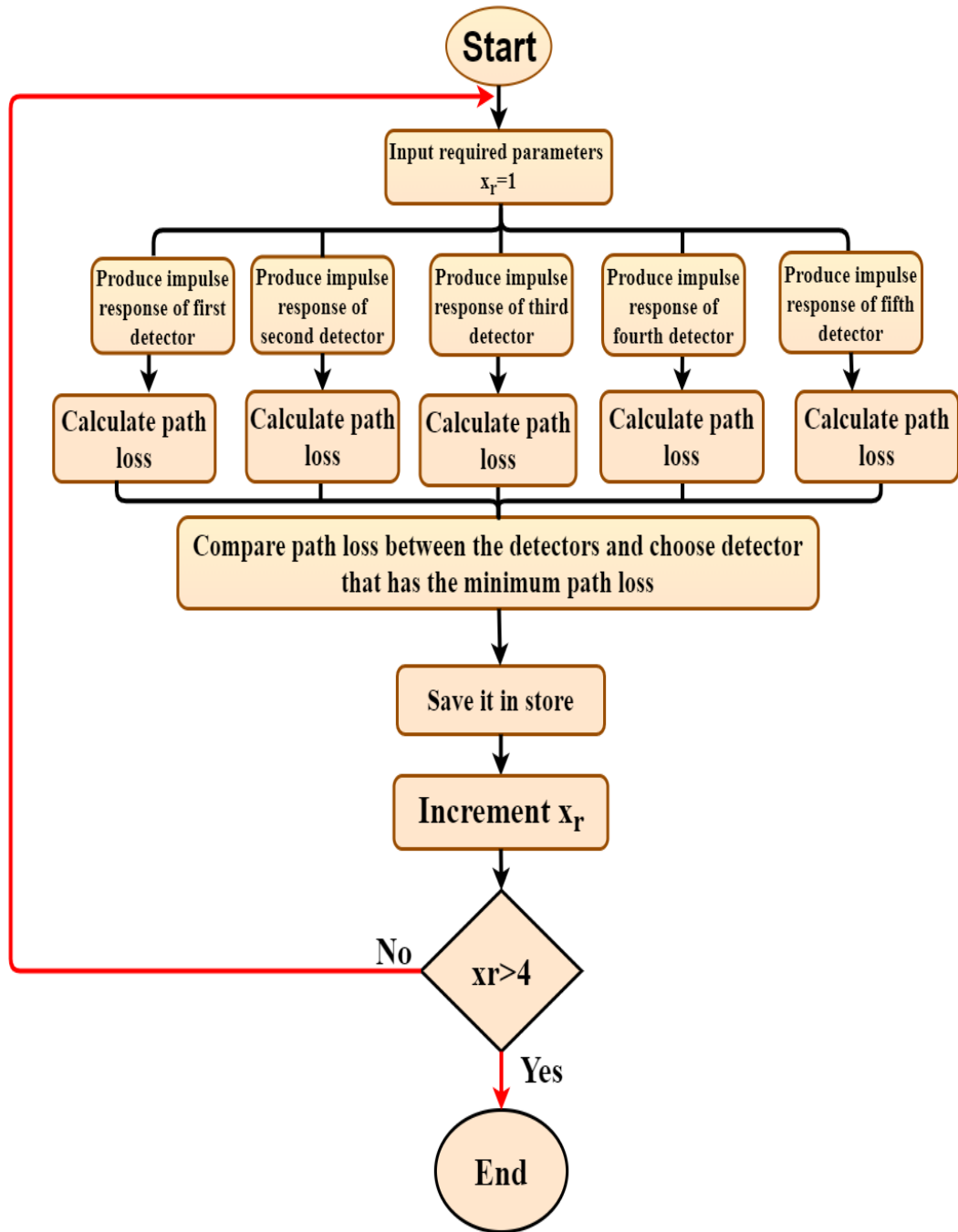


Figure (4.5): Flowchart for calculating path loss.

5. Compare the delay-spread of the five detectors and choose the detector that has the minimum delay-spread for this location.
6. Save the value in a store.
7. Repeat the steps from 1 to 6 for all locations of the RX.

To find the minimum path loss at all locations of the RX, the same steps of delay-spread are followed, except step 4 using equation (2.32) as shown in figure (4.5).

4.3.3 Flowchart for Calculating 3-dB Channel Bandwidth

Use the procedures in figure (4.6) to determine the maximum 3-dB channel bandwidth that will result in an increase in transmission rate at all RX locations.

1. Calculate the received power of first-order and second-order reflection for the first detector by following all the steps outlined in subsection (3.4.1).
2. Collect the received power that have same time and produce an impulse response.
3. Calculate the channel frequency response using the Fourier transform and a 3-dB channel bandwidth can be used by using equations (2.45) and (4.46) respectively.
4. Repeat the steps from 1 to 3 for the other four detectors.
5. Compare the results of the five detectors and choose the detector that has the maximum 3-dB bandwidth.
6. Save it in a store.
7. Repeat the steps from 1 to 6 for all locations of the RX.

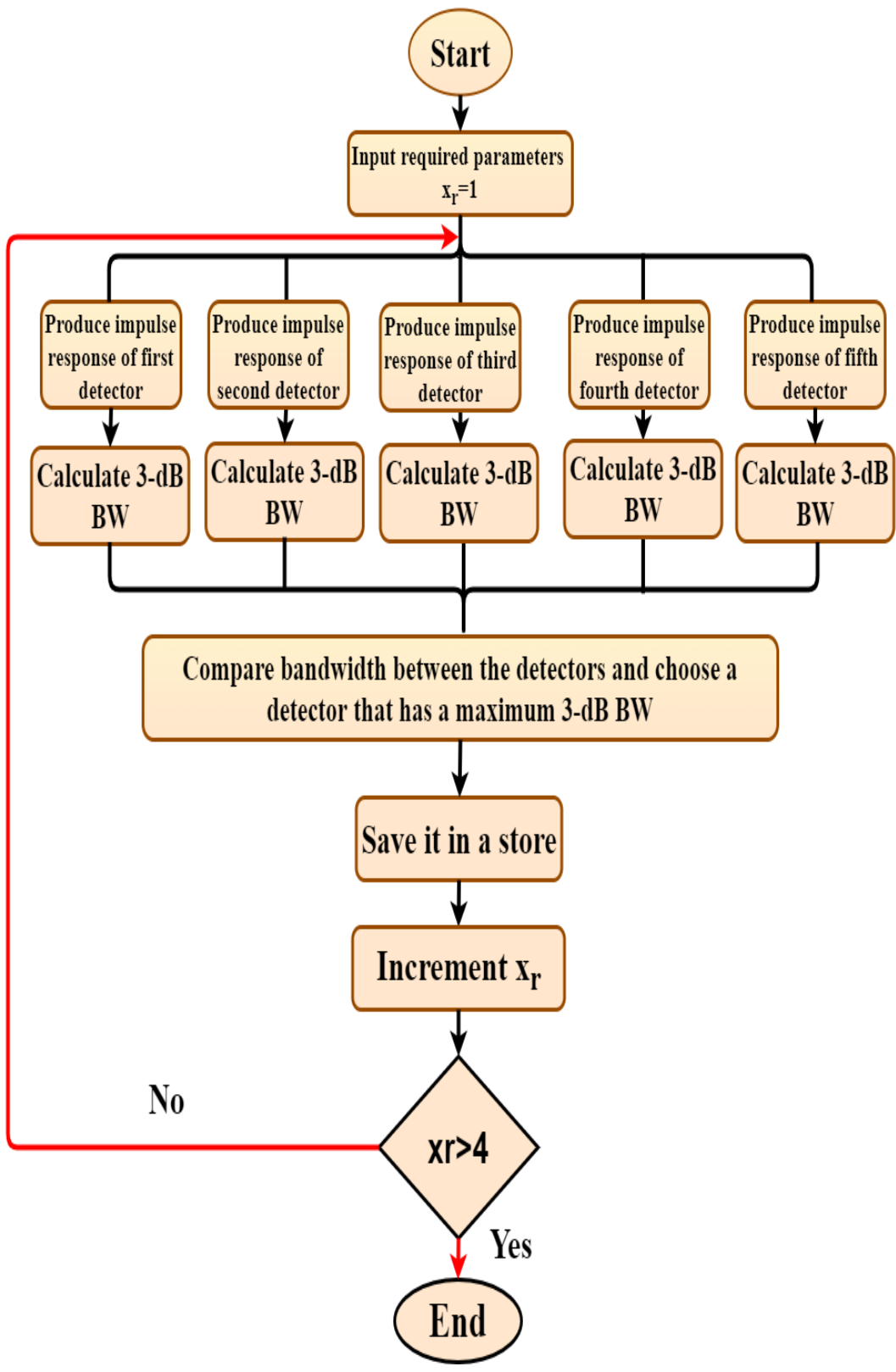


Figure (4.6): Flowchart for calculating 3-dB bandwidth.

4.3.4 Flowcharts for S/N and BER Calculation

S/N can be determined by using select the best combination to select the detector with the highest S/N. Follow these steps to calculate S/N_{SBC} as shown in figure (4.7).

1. Calculate the S/N of the first detector by using the steps in subsection (3.4.5) and save it in a store.
2. Repeat step 1 for the other four detectors.
3. Selecting the best combining technique is used to choose the detector that has a high S/N.
4. Calculate S/N in dB.
5. Save the value in a store.
6. Repeat the steps from 1 to 5 for all locations of the RX.

BER can be found by following these steps as shown in figure (4.8).

1. Calculate the S/N of the first detector by using the steps in subsection (3.4.5) and save it in a store.
2. Repeat step 1 for the other four detectors.
3. Using select the best combination to choose the detector that has a high S/N.
4. Calculate BER.
5. Save the value in a store.
6. Repeat the steps from 1 to 5for all locations of the RX.

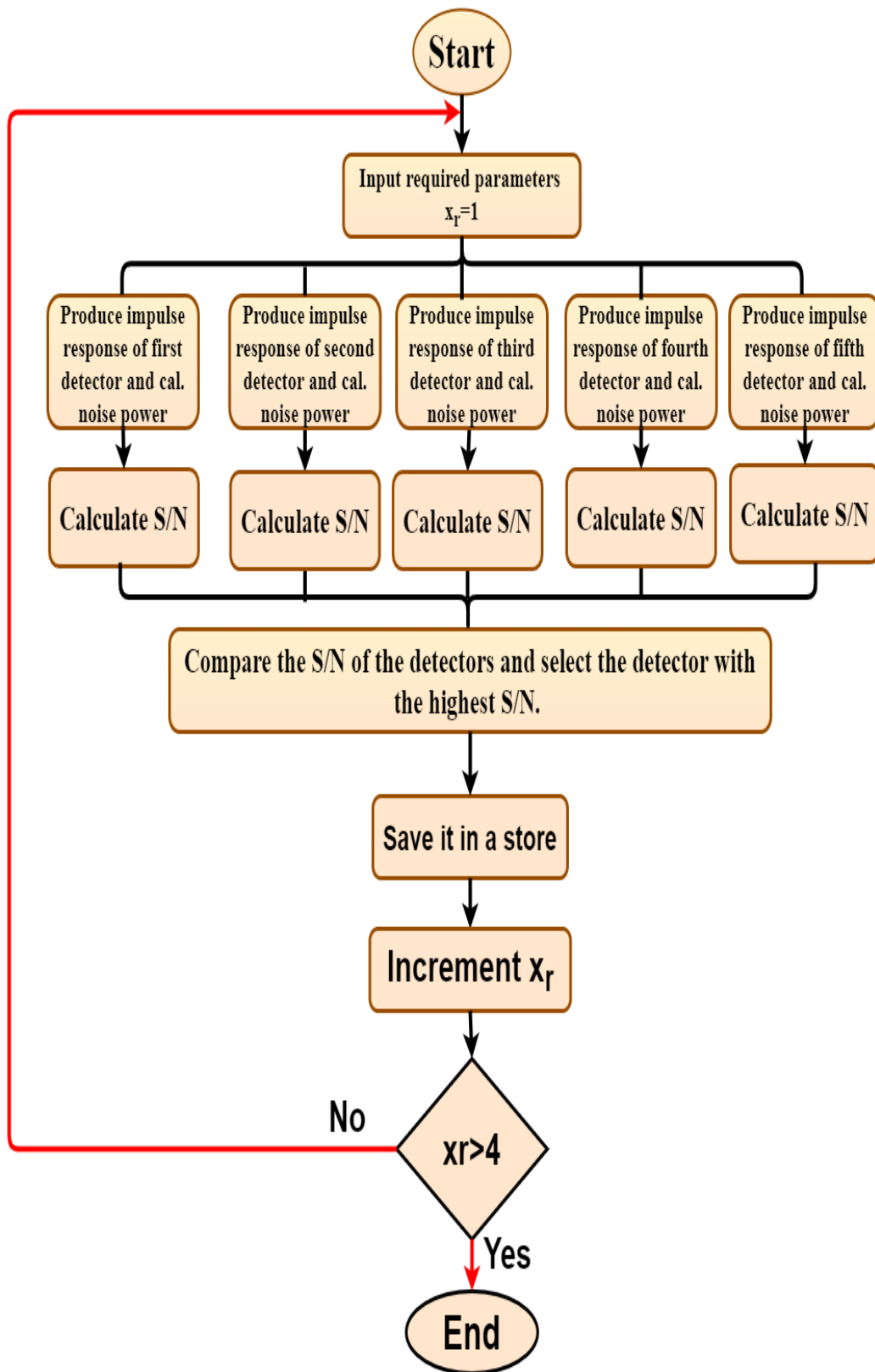


Figure (4.7): Flowchart for calculating S/N.

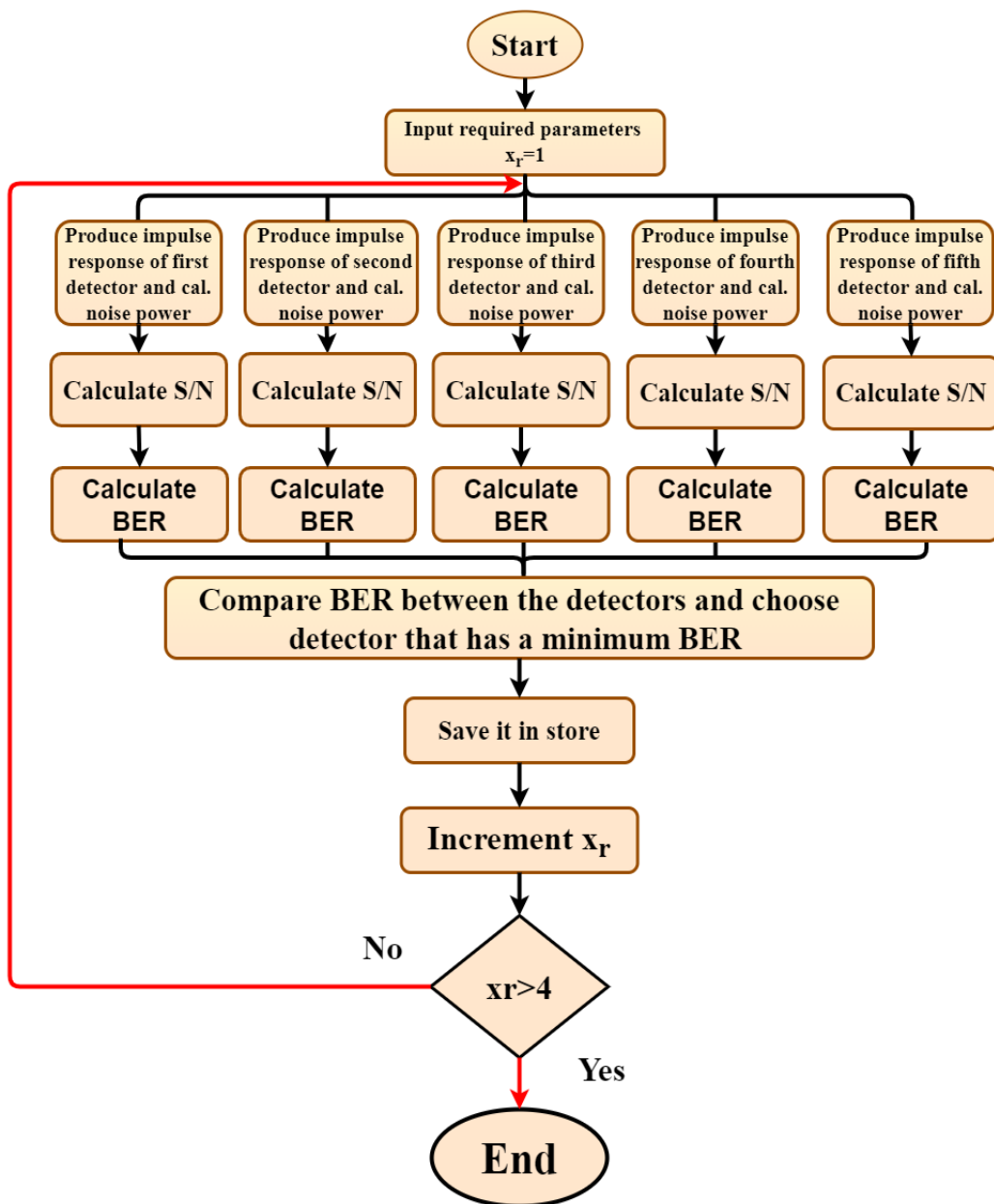


Figure (4.8): Flowchart for calculating BER.

4.4 Simulation Results and Discussion

The effectiveness of the proposed system is examined in this section in the presence of background noise and multi-path (because of the absence of a direct path between TX and RX) when the TX is always placed on the communication floor in the center of the room (2.5m, 2.5m, and 1m), as well

as mobility when the RX is moved along the x-line (1m, 2m, 3m, and 4m) at $y=1\text{m}$ and $y=2\text{m}$. The CDS results and our recommended system results will be compared. Impulse response, 3-dB channel bandwidth, BER, path loss, and R.M.S delay-spread were used to represent our findings and will be explained in the next subsections.

4.4.1 Impulse Response

The received optical power from multi-path reflection can be specified using the channel impulse response. The OWC system's impulse response is continuous in practice; we combined the received power using a time bin (1ns duration) into a single received power to limit the effect of subdividing reflecting surfaces (ceiling and walls) into small elements, resulting in the smoothness exhibited in the impulse response. To show the impulse response for both CDS and wide beam TX with ADR, the impulse response of the system is obtained when the sender is in the center of the room (2.5m,2.5m,1m) and the RX is positioned in two separate positions in the room, one on the side (1m, 1m, 1m) and another in the center (2.5m,2.5m,1m), as shown in figures (4.9) and (4.10), respectively. These

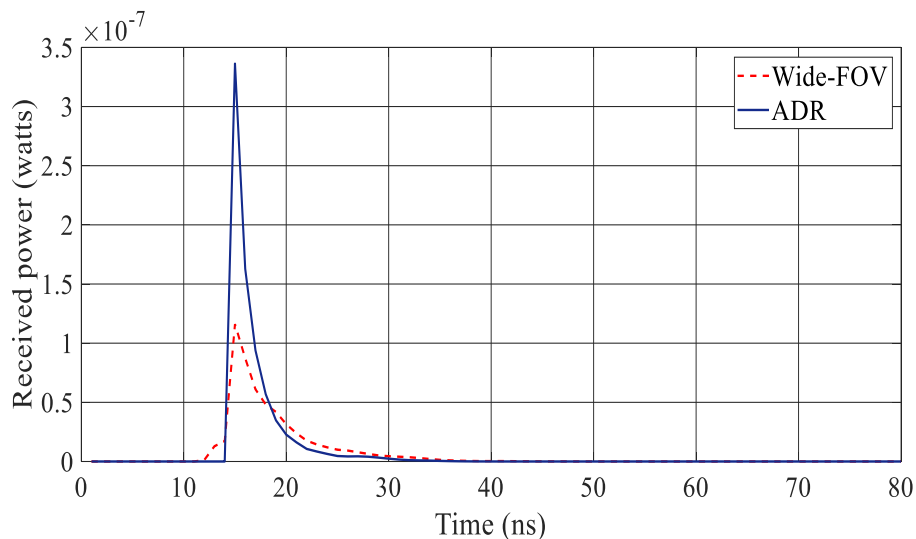


Figure (4.9): Impulse response when the TX in the center of the room and RX in the corner.

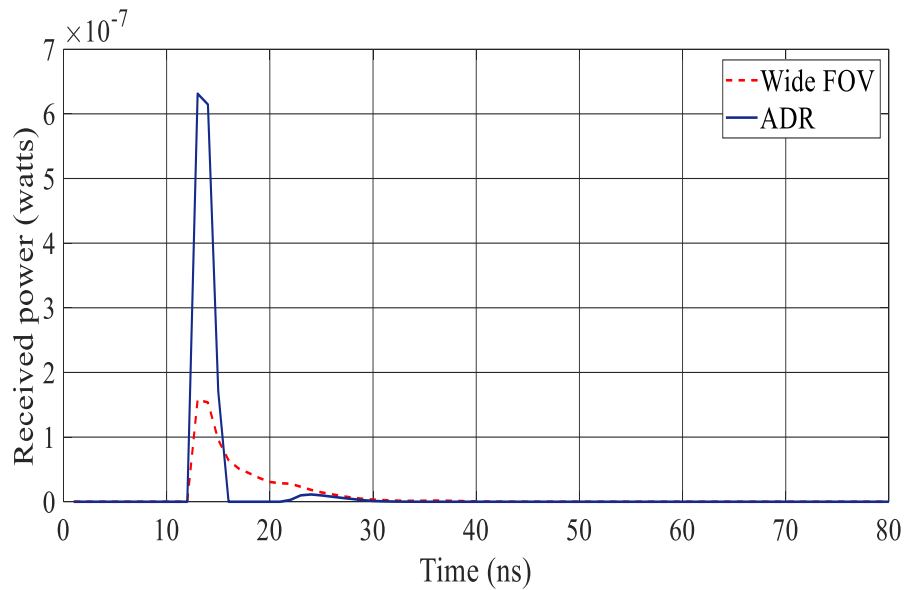


Figure (4.10): Impulse response when the TX and RX in the center of the room.

positions of the RX represent the worst and best case scenarios of the received power.

As the RX is placed in the room's corner, the maximum power received is $0.1161 \mu\text{W}$ for the CDS system. While the maximum power received is $0.3362 \mu\text{W}$ for the ADR system. When, on the other hand, the RX is situated in the center of the room, the maximum power received is $0.15781 \mu\text{W}$ for CDS and $0.6312 \mu\text{W}$ for the ADR system. When the TX and RX are in the middle of the room, the highest received power is proportional to their close proximity; as a result, the rays travel a short distance to reach the RX.

The figures also show that when using ADR the R.M.S delay-spread decreases because the range of rays that the RX can accept is limited by $\text{FOV} = 30^\circ$, so the rays that travel a long path and fall at an angle greater than FOV are rejected.

4.4.2 R.M.S Delay-Spread

Since non-directed transmission causes multi-path dispersion in indoor OWC, ISI may arise. The pulse-spread caused by the temporal dispersion of the receiving signal can be precisely described by the R.M.S delay-spread. Because certain rays travel a great distance to reach the RX while others only travel a short distance, each ray has a different effect on the spread of the signal; thus, the R.M.S is used to calculate the delay-spread. For comparison and observation of improvements in the system while utilizing the ADR, the R.M.S delay-spread for both CDS and our proposed method is computed at each given RX position.

The comparison is presented in figures (4.11) and (4.12), where the R.M.S delay-spread when the RX is traveling along the x-axis at $y = 1\text{m}$, is 2.16 ns for CDS when the RX is at the corner (1m,1m,1m) and (4m,1m,1m), and equal to 2.29 ns when the RX is moving toward the center (2m,1m,1m) and (3m,1m,1m). The delay-spread rises when the RX is moving toward the

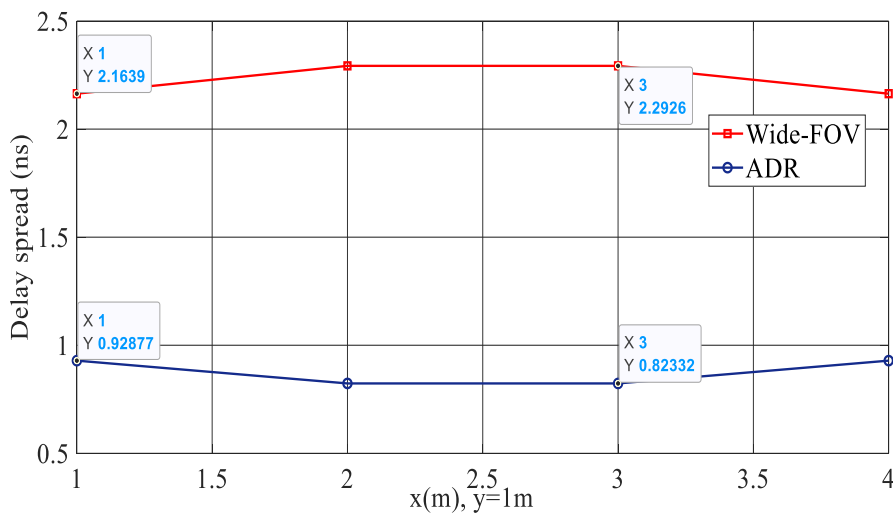


Figure (4.11): Comparison of delay-spread between CDS and ADR when the sender is placed at (2.5m,2.5m,1m) and reception is traveling along the x-axis at $y=1\text{m}$.

center because the RX accepts more rays that take a long time to reach the RX because of the wide FOV ($FOV = 90^\circ$).

The R.M.S delay-spread is reduced when a wide-FOV is replaced by ADR because of the narrow FOV being used, which rejects the rays that are incident at an angle greater than FOV ($FOV = 30^\circ$), which is equal to 0.923 ns when the RX is situated at the corner and decreases to 0.823 ns when it is situated at (2m, 1m, 1m) and at (3m, 1m, 1m).

When the RX travels along the x-axis at $y = 2m$ the delay-spread for both systems is shown in figure (4.12). The delay-spread for CDS is 2.2926 ns when the RX is at (1 m, 2 m, 1 m) and (4 m, 2 m, 1 m), while it is 0.88455

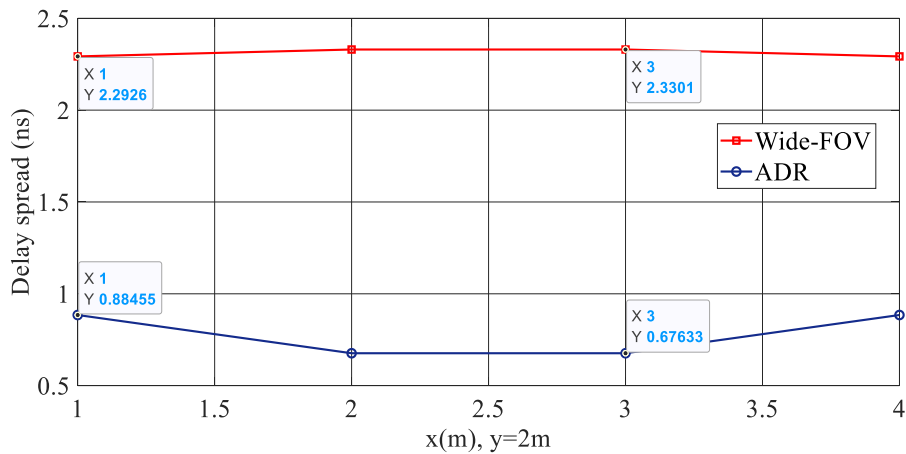


Figure (4.12): Comparison of delay-spread between CDS and ADR when the sender is placed at (2.5m,2.5m,1m) and reception is traveling along the x-axis at $y=2m$.

ns for ADR. When the RX is close to the TX, it is equal to 2.3301 ns for CDS while it is equal to 0.67633 ns for ADR. It is evident from the findings that the delay-spread for CDS increases when the RX is at $y = 2m$, because the wide-FOV RX at this location accepts more rays that travel a long distance to reach the RX than it does at $y = 1m$. When ADR is used, the delay-spread is decreased because the distance between the TX and RX is

smaller than it was in the previous scenario (when $y = 1$ m), which causes the rays to travel a shorter distance to reach the RX and the narrow-FOV causes rays incident at an angle greater than 30° to be rejected.

4.4.3 S/N Performance Analysis

In OWC systems, O.O.K employs a rectangular pulse with a duration equal to the bit period (3 ns). The S/N is computed using the powers p_{s1} and p_{s0} , which correspond to logic levels '1' and '0', respectively. Indoor OWC suffers greatly from preamplifier noise, shot noise connected with the signal, and shot noise in the RX's circuitry produced by ambient light.

In the ADR, the SBC technique is used to pick the detector with the highest S/N among all detectors. The photosensitive area for both CDS and each detector in ADR is 10 mm^2 in order to enhance the photodetector's bandwidth. The bandwidth of each detectors and CDS is 308 MHz. The bit rate is 308 Mbits/sec where the bit rate and bandwidth are equivalent as in [73]. As in [97] the preamplifier employed is TIA with a noise current spectral density of $2.5 \text{ pA}/(\text{Hz})^{1/2}$.

Figures (4.13) and (4.14), respectively, show the S/N for both systems when the TX is situated in the middle of the space and the RX is travelling along the x-axis. Figure (4.13) shows the S/N for CDS and ADR and compares them. S/N equals -9.4 dB for CDS and 3.677 dB for ADR when the recipient is in the room's far corner. When the RX is moving toward the center of the room, S/N reaches 7.3328 dB for CDS, while it reaches 12.828 dB for ADR, where increased in S/N by 5dB when ADR is used because it filters out direct rays of noise from spotlights due to detectors' being inclined at a specific angle, only the reflections reach the RX, so the S/N improves. The system performance is enhanced compared with CDS when using ADR.

Where the effect of the spot lights is too severe on the desired signal, this can be seen very clearly in the CDS system depicted in the figure, which has S/N in the negative.

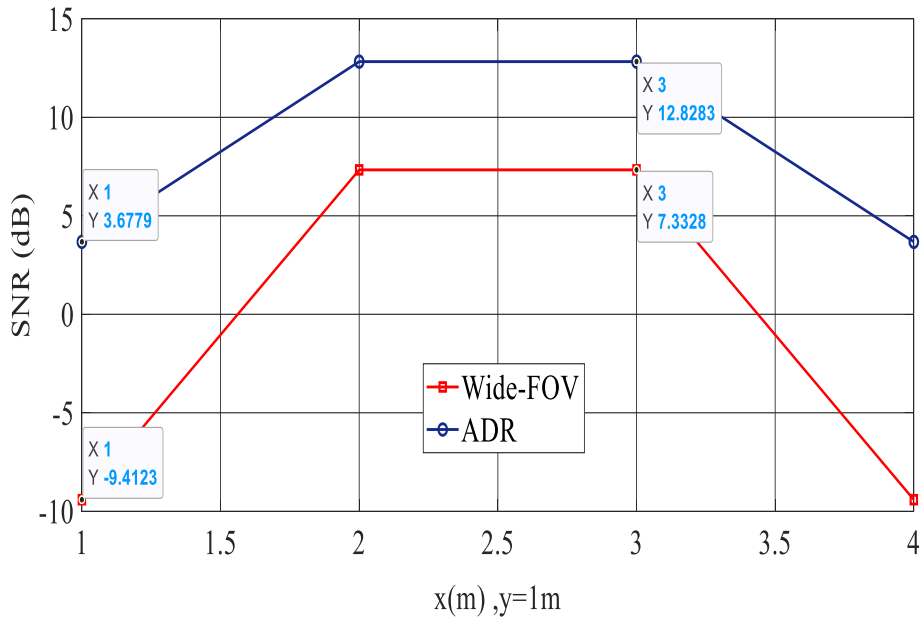


Figure (4.13): Comparison of S/N between CDS and ADR when the sender is placed at (2.5m,2.5m,1m) and reception is traveling along the x-axis at y=1m.

The case where the RX is traveling along the x-axis when $y = 2m$ is different for CDS from the previous scenario (when $y = 1m$). The S/N at the corner equals 7.3328dB and decreases to -16.3369dB when the RX is moving to be close to the TX as shown in figure (4.14). These findings are because when the RX is at the corner, a lot of rays radiated from the lamps do not reach the RX, so their effect is low on the signal. When the RX becomes closer to the TX, the effect of the four lamps is very strong. When the wide-FOV is replaced by ADR, the performance of the system is enhanced, where the S/N is equal to 9.1442dB when the RX at the corner of the room and equal to 15.5057dB when the RX becomes closer to the TX.

The improvement in S/N is greater than 30dB when ADR is utilized instead of wide-FOV and the TX and RX are closer to each other.

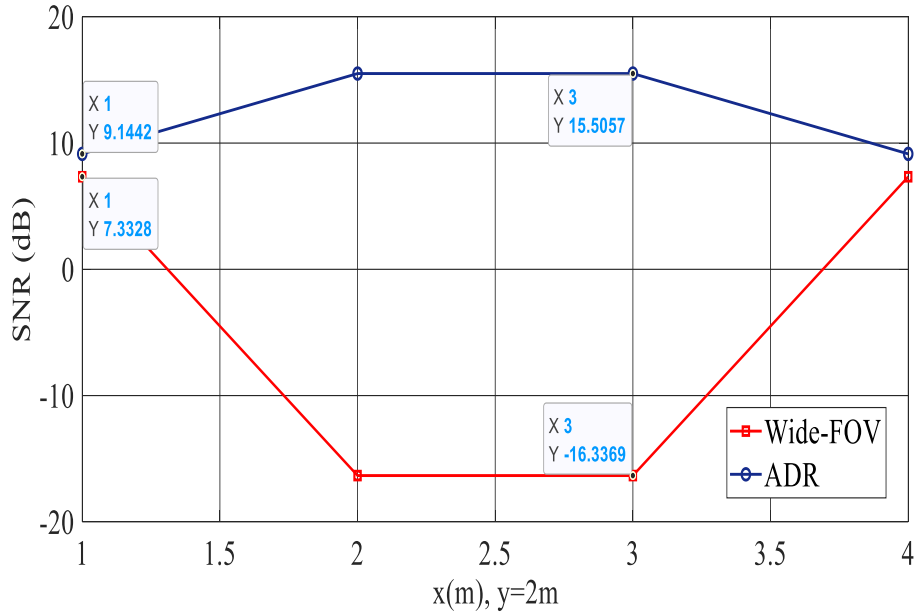


Figure (4.14): Comparison of S/N between CDS and ADR when the sender is placed at (2.5m,2.5m,1m) and reception is traveling along the x-axis at y=2m.

4.4.4 Bit Error Rate

The BER is related to the S/N where it decreases as the S/N increases and this leads to increasing the transmission data rate. BER is given for both systems when the RX is traveling along the x axis at y= 1m and y= 2m and the TX is positioned in the center of the room.

Table (4.1) show BER when the RX is moving along the x axis at y= 1m and shows that the BER decreases when the S/N grows, and ADR has a better BER than the CDS system. Because the detector was installed in a way that improves the S/N. BER is equal to 1×10^{-2} when S/N is 7.33 dB when the RX is traveling toward the middle of the room for the CDS system, while reduced to 5.9502×10^{-6} , when ADR is used. This boost in the system is due to the fact that ADR rejects direct spotlight rays, which have a severe

influence on the intended signal and distort the information. This improvement enables an increase in the transmission data.

Table (4.1): BER and S/N for both CDS and ADR when $y=1m$.

x at y=1m	Distance between sender & RX (meter)	S/N of CDS (dB)	BER of CDS	S/N of ADR (dB)	BER of ADR
1	1.5	-9.41	0.36	3.6779	6.34×10^{-2}
2	0.5	7.33	1×10^{-2}	12.8283	5.9502×10^{-6}
3	0.5	7.33	1×10^{-2}	12.8283	5.9502×10^{-6}
4	1.5	-9.41	0.36	3.6779	6.34×10^{-2}

Based on the comparison of the two tables (4.1) and (4.2), for CDS when the RX is at the corner, $y = 2m$ has better results where BER is equal to 1×10^{-2} , while $y = 1m$ is better when the RX becomes closer to the TX, where BER is equal to 1×10^{-2} , but this is not the same when ADR, where $y = 2m$ is better for all the positions.

Table(4.2): BER and S/N for both CDS and ADR when $y=2m$.

x at y=2m	Distance between sender & RX (meter)	S/N of CDS (dB)	BER of CDS	S/N of ADR (dB)	BER of ADR
1	1.5	7.3328	1×10^{-2}	9.1442	2.0814×10^{-3}
2	0.5	-16.3369	0.4394	15.5057	1.2569×10^{-9}
3	0.5	-16.3369	0.4394	15.5057	1.2569×10^{-9}
4	1.5	7.3328	1×10^{-2}	9.1442	2.0814×10^{-3}

4.4.5 Path Loss

Optical power attenuation occurs due to the nature of optical signal transmission, which includes multi-path propagation, lossy reflection from the ceiling, walls, and other objects resulting in optical path loss, and a finite detector collecting area. As a result, poor system performance is caused by a rise in R.M.S delay-spread and path loss. The room size affects path loss, where the path loss is reduced when the room size becomes small as a result of decreasing the distance between sender and RX.

When the RX is at $y=1$ m and along the x -axis, figure (4.15) depicts the distribution of path loss for both CDS and ADR when the TX is positioned at the center of the room. The amount of path loss increases as the reception goes closer to the edges of the room when the quantity of incoming optical power drops. For the CDS setup, the path loss is equal to 62.6 dB, the

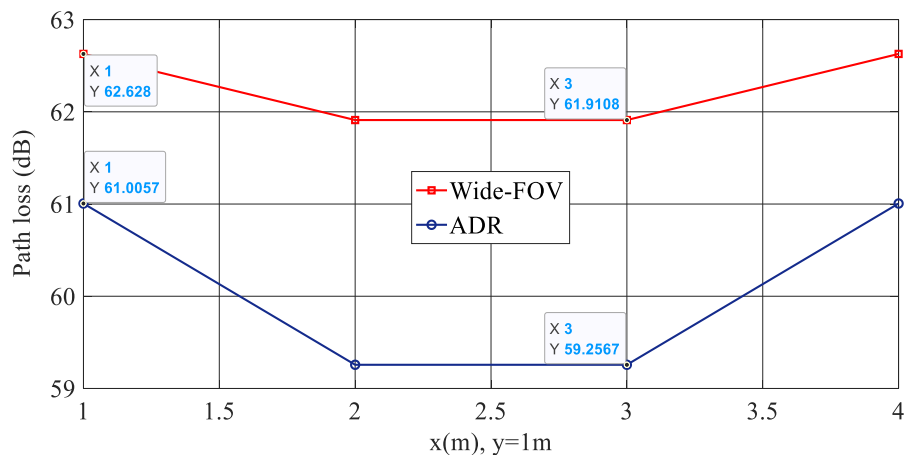


Figure (4.15): Comparison of path loss between CDS and ADR when the sender is placed at (2.5m,2.5m,1m) and reception traveling along the x -axis at $y=1$ m. signal power is minimal at the room corners due to the considerable distance between transmission and reception, and is equal to 61dB when ADR is utilized. As a result, the CDS suffers the most path loss around the room's corners. While the ADR path loss decreases because of the large received power compared to the received power in the CDS. The path loss for both

configurations is decreased when the RX is moving toward the TX as a result of decreasing the distance between them. Where path loss for the CDS system is equal to 61.91 dB and equal to 59.25 dB for ADR when the RX moves to (2m,1m,1m) and (3m,1m,1m).

When the RX changes the y-coordinate to be $y = 2\text{m}$, the path loss for both systems is improved because reducing the distance between the sender and RX where it is equal to 61.9dB when the RX is at the corner of the room and reduced to 61.2dB when the RX is moving toward the center of the room for CDS, as shown in figure (4.16). The path loss for ADR was reduced to 59.3dB at the corner and equal to 58.9dB when moving to be near the TX.

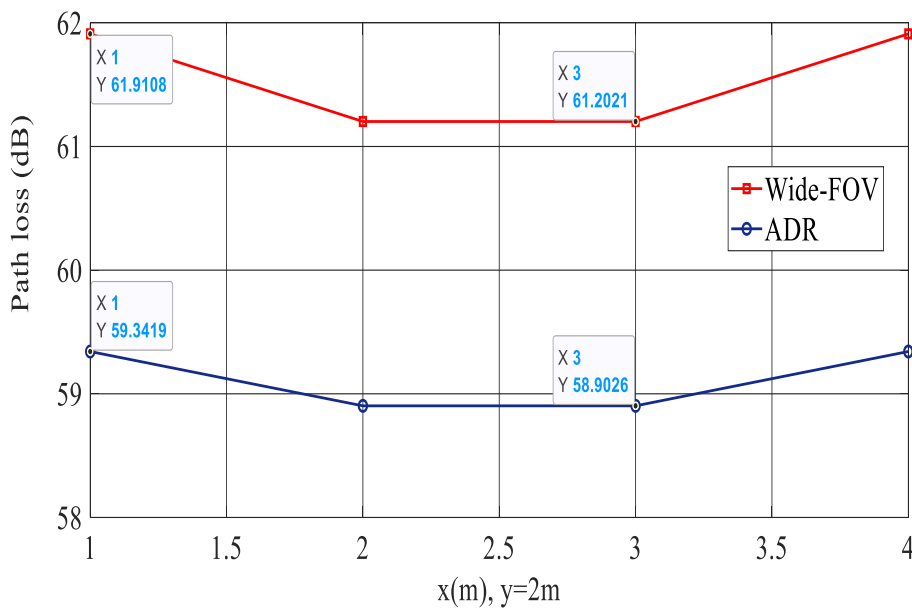


Figure (4.16): Comparison of path loss between CDS and ADR when the sender is placed at (2.5m,2.5m,1m) and reception traveling along the x-axis at $y=2\text{m}$.

4.4.6 3-dB Channel Bandwidth

As indicated in figure (4.17), the maximum bandwidth for CDS is 66 MHz when the TX is in the center of the room and the RX is positioned at

(1 m, 1 m, 1 m) and at (4 m, 1 m, 1 m), whereas the maximum bandwidth for ADR is 180 MHz when the RX is positioned at (2 m, 1 m, 1 m) and (3 m, 1 m, 1 m), this increase in bandwidth is due to a reduction in delay-spread. From the figure, we note that the highest bandwidth can be reached in the CDS system when the RX is at the ends, whereas in ADR has the highest bandwidth when the RX is close to the TX. This is because the delay-spread in the CDS system is large when the RX is close to the TX because of the large-FOV that accepts more rays that take a long path to reach the RX, so the delay-spread increases and, as a result, the bandwidth decreases. Because of the narrow-FOV in ADR that rejects the rays that travel a long path to reach the RX, the maximum bandwidth is reached when the RX is close to the center of the room.

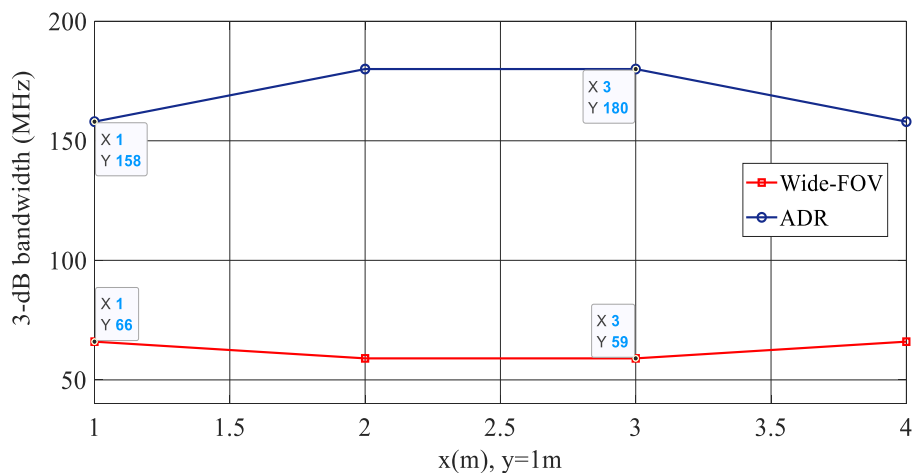


Figure (4.17): Comparison of 3-dB bandwidth between CDS and ADR when the sender is placed at (2.5m,2.5m,1m) and reception traveling along the x-axis at y=1m.

Figure (4.18) displays the 3-dB channel bandwidth when $y = 2\text{m}$. For CDS, channel bandwidth is very narrow compared with ADR. At the corner of the room, the bandwidth is equal to 59 MHz, while it decreases to 57 MHz when the RX becomes close to the RX. In contrast, in ADR, the bandwidth

is equal to 173 MHz at the corner and increases to 232 MHz when it becomes close to the center. This behavior is because, when the RX is at the corner of the room, the delay-spread is large in ADR and small in CDS.

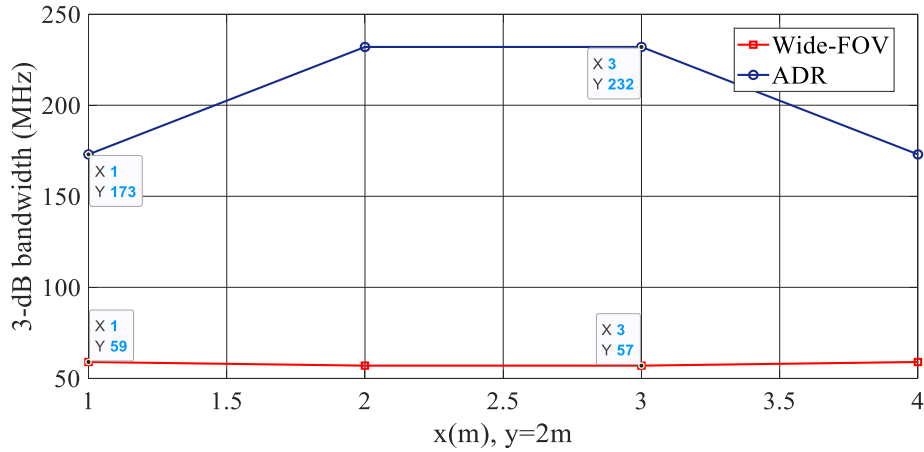


Figure (4.18): Comparison of 3-dB bandwidth between CDS and ADR when the sender is placed at (2.5m,2.5m,1m) and reception traveling along the x-axis at y=2m.

4.5 Comparison with Previous Works

In this section, our results will be compared with previous works from the point of taking into account the S/N, delay-spread, BER or not, number of detectors, area of the detector, mobility of the RX, and background noise as shown in table (4.3).

Table (4.3): Comparison between our work and previous works.

Ref.	[41]	[73]	[98]	[63]	[46]	This work
Background noise	Not considered	considered	Not consider	considered	Not considered	considered
BER	Not considered	Not considered	considered	Not considered	Not considered	considered
No. Of detectors	3	9	4	4wide-FOV RX & 4-ADR each containing from 3-detectors	4	5
Area of RX	4mm ²	1cm ²	1cm ²	20mm ²	4mm ²	10mm ²
Path loss	Not considered	Not considered	Not considered	Not considered	Not considered	considered
S/N	considered	considered	Not considered	considered	considered	considered
Delay-spread	considered	considered	Not considered	Not considered	considered	considered

CHAPTER FIVE

CONCLUSIONS AND FUTURE WORK

5.1 Research Work's Conclusions

The OWC system places a lot of emphasis on the design issues with indoor systems, including background noise, multi-path dispersion, and others. This dissertation looked into the effects of these issues on the data that was received. The Matlab program was used to implement the calculations and ray tracing procedures in this dissertation. The 3-dB channel bandwidth, path loss, BER, and S/N were the main performance metrics used to assess the OWC systems' performance. When a number of factors are considered and improve the system, such as:

1. The area of the photodetector is selected to be small (10mm^2) in order to minimize the capacitance that results in a wider bandwidth of the RX since there is an inverse connection between the size of the photodetector and bandwidth.
 2. Eye and skin safety is saved by using a diffuse TX.
 3. Changing the angle of the FOV and viewing the result for each change in order to reject the rays that travel for a long time to reach the recipient. The best FOV that improves performance by decreasing multi-path dispersion and background noise while maintaining the simplicity and low cost of the system. When the FOV becomes narrow, the R.M.S delay-spread decreased, resulting in an improved S/N and an increase in bandwidth whereas it reaches 378.07 MHz when the FOV is at 10° . S/N enhancement also contributed to a reduction in BER.
- 5.1 ADR is used to lessen the impact of noise in the background and multi-path. The findings are shown when the RX moving along the x-axis at

$y=1\text{ m}$ and 2 m , which showed an enhancement in several metrics, such as the S/N. The direct rays from the light spots are rejected by the detector tilting at a specific angle, and the improvement reaches more than 10 dB when the sender is in the middle of the room and the RX is in the corner. This improvement leads to a decrease in the BER. Due to the usage of a narrow FOV, the delay-spread was reduced to 0.823 ns, increasing the 3-dB bandwidth to 180 MHz when the RX was pointed near the center of the room at $y=1\text{ m}$ and 232 MHz when it was at $y=2\text{ m}$.

5.2 Areas of Further Investigation

There are a number of research-related topics that deserve additional investigation. The following are a few of them:

1. The calculations will take place in the real environment, and its impact on the system's performance will be investigated in both the systems (wide TX and different FOV and ADR).
2. Filters in conjunction with an ADR can be used to study its effect on the S/N.
3. Investigate the performance of the system that consists of a multi-beam TX with a ADR RX.
4. Finally, the use of a reflector and an examination of its impact on system performance and power received.

REFERENCES

- [1] A. Mahdy and J. S. Deogun, “Wireless optical communications: a survey,” in *2004 IEEE Wireless Communications and Networking Conference (IEEE Cat. No.04TH8733)*, Mar. 2004, vol. 4, pp. 2399–2404. doi: 10.1109/WCNC.2004.1311464.
- [2] O. Alsulami, A. T. Hussein, M. T. Alresheedi, and J. M. H. Elmirghani, “Optical Wireless Communication Systems, A Survey,” *arXiv preprint arXiv*, pp. 1–22, Dec. 2018, doi: 10.48550/ARXIV.1812.11544.
- [3] A. Al-Kinani, C.-X. Wang, L. Zhou, and W. Zhang, “Optical Wireless Communication Channel Measurements and Models,” *IEEE Communications Surveys & Tutorials*, vol. 20, no. 3, pp. 1939–1962, 2018, doi: 10.1109/COMST.2018.2838096.
- [4] M. Z. Chowdhury, M. T. Hossan, A. Islam, and Y. M. Jang, “A Comparative Survey of Optical Wireless Technologies: Architectures and Applications,” *IEEE Access*, vol. 6, pp. 9819–9840, 2018, doi: 10.1109/ACCESS.2018.2792419.
- [5] Z. Ghassemlooy, S. Zvanovec, M.-A. Khalighi, W. O. Popoola, and J. Perez, “Optical wireless communication systems,” *Optik*, vol. 151, pp. 1–6, Dec. 2017, doi: 10.1016/j.ijleo.2017.11.052.
- [6] R. Ramirez-Iniguez and R. J. Green, “Optical antenna design for indoor optical wireless communication systems,” *International Journal of Communication Systems*, vol. 18, no. 3, pp. 229–245, Apr. 2005, doi: 10.1002/dac.701.
- [7] Y.-L. Yu, S.-K. Liaw, H. Kishikawa, and N. Goto, “A simple beam expanded for indoor optical wireless communication with short transmission distance,” *Optics Communications*, vol. 451, no. May, pp.

- 216–219, Nov. 2019, doi: 10.1016/j.optcom.2019.06.045.
- [8] A. T. Hussein and J. M. H. Elmirghani, “10 Gbps Mobile Visible Light Communication System Employing Angle Diversity, Imaging Receivers, and Relay Nodes,” *Journal of Optical Communications and Networking*, vol. 7, no. 8, p. 718, Aug. 2015, doi: 10.1364/JOCN.7.000718.
- [9] A. T. Hussein, M. T. Alresheedi, and J. M. H. Elmirghani, “20 Gb/s Mobile Indoor Visible Light Communication System Employing Beam Steering and Computer Generated Holograms,” *Journal of Lightwave Technology*, vol. 33, no. 24, pp. 5242–5260, Dec. 2015, doi: 10.1109/JLT.2015.2495165.
- [10] A. T. Hussein, M. T. Alresheedi, and J. M. H. Elmirghani, “25 Gbps mobile visible light communication system employing fast adaptation techniques,” in *2016 18th International Conference on Transparent Optical Networks (ICTON)*, Jul. 2016, vol. 2016-Augus, pp. 1–7. doi: 10.1109/ICTON.2016.7550488.
- [11] S. H. Younus and J. M. H. Elmirghani, “WDM for high-speed indoor visible light communication system,” in *2017 19th International Conference on Transparent Optical Networks (ICTON)*, Jul. 2017, pp. 1–6. doi: 10.1109/ICTON.2017.8024797.
- [12] A. T. Hussein, M. T. Alresheedi, and J. M. H. Elmirghani, “Fast and Efficient Adaptation Techniques for Visible Light Communication Systems,” *Journal of Optical Communications and Networking*, vol. 8, no. 6, pp. 382–397, Jun. 2016, doi: 10.1364/JOCN.8.000382.
- [13] M. T. Alresheedi and J. M. H. Elmirghani, “Adaptive 10 Gbit/s Mobile Optical Wireless Systems Employing Beam Delay, Angle and Power Adaptation with Imaging Receivers,” in *2011 IEEE Global*

- Telecommunications Conference - GLOBECOM 2011*, Dec. 2011, pp. 1–6. doi: 10.1109/GLOCOM.2011.6133573.
- [14] M. T. Alresheedi and J. M. H. Elmirghani, “10 Gb/s Indoor Optical Wireless Systems Employing Beam Delay, Power, and Angle Adaptation Methods With Imaging Detection,” *Journal of Lightwave Technology*, vol. 30, no. 12, pp. 1843–1856, Jun. 2012, doi: 10.1109/JLT.2012.2190970.
- [15] F. E. Alsaadi, M. A. Alhartomi, and J. M. H. Elmirghani, “Fast and Efficient Adaptation Algorithms for Multi-Gigabit Wireless Infrared Systems,” *Journal of Lightwave Technology*, vol. 31, no. 23, pp. 3735–3751, Dec. 2013, doi: 10.1109/JLT.2013.2286743.
- [16] M. T. Alresheedi and J. M. H. Elmirghani, “Adaptive multibeam spot diffusing optical wireless system with imaging receivers,” in *2011 13th International Conference on Transparent Optical Networks*, Jun. 2011, pp. 1–7. doi: 10.1109/ICTON.2011.5971007.
- [17] F. E. Alsaadi and J. M. H. Elmirghani, “Mobile Multigigabit Indoor Optical Wireless Systems Employing Multibeam Power Adaptation and Imaging Diversity Receivers,” *Journal of Optical Communications and Networking*, vol. 3, no. 1, pp. 27–39, Jan. 2011, doi: 10.1364/JOCN.3.000027.
- [18] F. Alsaadi and J. Elmirghani, “Beam power and angle adaptation in multibeam 2.5 Gbit/s spot diffusing mobile optical wireless system,” *IEEE Journal on Selected Areas in Communications*, vol. 28, no. 6, pp. 913–927, Aug. 2010, doi: 10.1109/JSAC.2010.100815.
- [19] M. Uysal and H. Nouri, “Optical wireless communications - An emerging technology,” in *2014 16th International Conference on Transparent Optical Networks (ICTON)*, Jul. 2014, pp. 1–7. doi:

10.1109/ICTON.2014.6876267.

- [20] H. Kaushal, V. K. Jain, and S. Kar, “Overview of Wireless Optical Communication Systems,” in *Free Space Optical Communication*, New Delhi: Springer India, 2017, pp. 1–39. doi: 10.1007/978-81-322-3691-7_1.
- [21] D. Karunatilaka, F. Zafar, V. Kalavally, and R. Parthiban, “LED Based Indoor Visible Light Communications: State of the Art,” *IEEE Communications Surveys & Tutorials*, vol. 17, no. 3, pp. 1649–1678, Jul. 2015, doi: 10.1109/COMST.2015.2417576.
- [22] K. Akhavan, M. Kavehrad, and S. Jivkova, “Wireless infrared in-house communications: how to achieve very high bit rates,” in *2000 IEEE Wireless Communications and Networking Conference. Conference Record (Cat. No.00TH8540)*, Sep. 2000, vol. 2, pp. 698–703. doi: 10.1109/WCNC.2000.903939.
- [23] A. G. Al-Ghamdi and J. M. H. Elmirghani, “Optimization of a pyramidal fly-eye diversity receiver for optical wireless systems under the influence of multipath dispersion and background noise,” *Microwave and Optical Technology Letters*, vol. 36, no. 5, pp. 401–406, Mar. 2003, doi: 10.1002/mop.10776.
- [24] A. G. A.-G. and J. M. H. Elmirghani, “Performance of an Optical Pyramidal Fly-eye Diversity Receiver for Indoor Wireless Communication Systems in the Presence of Background Noise and Multipath Dispersion,” in *In Proc. London Communications Symp*, Sep. 2002, pp. 221–224.
- [25] A. G. Al-Ghamdi and J. M. H. Elmirghani, “Performance and Field of View Optimization of an Optical Wireless Pyramidal Fly-eye Diversity Receiver,” *Journal of Optical Communications*, vol. 23, no. 6, pp. 215–

222, Jan. 2002, doi: 10.1515/JOC.2002.23.6.215.

- [26] A. G. Al-Ghamdi and J. M. H. Elmirghani, "Optimization of a triangular PFDR antenna in a fully diffuse ow system influenced by background noise and multipath propagation," *IEEE Transactions on Communications*, vol. 51, no. 12, pp. 2103–2114, Dec. 2003, doi: 10.1109/TCOMM.2003.820758.
- [27] A. G. Al-Ghamdi and J. M. H. Elmirghani, "Triangular PFDR antenna optimisation under the restriction of background noise and multipath propagation in an optical wireless system," in *IEEE International Conference on Communications, 2003. ICC '03.*, May 2003, vol. 3, pp. 2013–2019. doi: 10.1109/ICC.2003.1203952.
- [28] A. G. Al-Ghamdi and J. M. H. Elmirghani, "Analysis of Diffuse Optical Wireless Channels Employing Spot-Diffusing Techniques, Diversity Receivers, and Combining Schemes," *IEEE Transactions on Communications*, vol. 52, no. 10, pp. 1622–1631, Oct. 2004, doi: 10.1109/TCOMM.2004.836509.
- [29] A. G. Al-Ghamdi and J. M. H. Elmirghani, "Line strip multibeam transmitter to combat the multipath dispersion and background noise of the indoor optical wireless links," in *IEEE Global Telecommunications Conference, 2004. GLOBECOM '04.*, Dec. 2004, vol. 6, pp. 3630–3635. doi: 10.1109/GLOCOM.2004.1379046.
- [30] A. G. Al-Ghamdi and J. M. H. Elmirghani, "Line Strip Spot-Diffusing Transmitter Configuration for Optical Wireless Systems Influenced by Background Noise and Multipath Dispersion," *IEEE Transactions on Communications*, vol. 52, no. 1, pp. 37–45, Jan. 2004, doi: 10.1109/TCOMM.2003.822160.
- [31] J. M. H. Elmirghani and A. G. Al-Ghamdi, "Spot diffusing technique

- and angle diversity performance for high speed indoor diffuse infrared wireless transmission,” *IEE Proceedings - Optoelectronics*, vol. 151, no. 1, pp. 46–52, Feb. 2004, doi: 10.1049/ip-opt:20040140.
- [32] A. G. Al-Ghamdi and J. M. H. Elmirghani, “Characterization of mobile spot diffusing optical wireless systems with diversity receiver,” in *2004 IEEE International Conference on Communications (IEEE Cat. No.04CH37577)*, Jun. 2004, pp. 133-138 Vol.1. doi: 10.1109/ICC.2004.1312467.
- [33] J. Alattar and J. Elmirghani, “An Indoor Optical Wireless System Based on Different Spot Diffusing Geometries and A Diversity Receiver,” in *LCS’05, University College London*, Sep. 2005, pp. 202–205.
- [34] J. M. Alattar and J. M. H. Elmirghani, “Multi-line Multi-Spot Diffusing Indoor OW Channel with A 7-Detectors Diversity Receiver,” in *IEEE London Commun. Symp*, Sep. 2006, pp. 37–40.
- [35] J. M. Alattar and J. M. H. Elmirghani, “Transmit Power Adaptation for a Mobile Multibeam Spot Diffusing Optical Wireless System in One and Two Planes,” in *2008 IEEE International Conference on Communications*, May 2008, pp. 5204–5208. doi: 10.1109/ICC.2008.977.
- [36] J. M. Alattar and J. M. H. Elmirghani, “Optical Wireless Systems Employing Adaptive Collaborative Transmitters in an Indoor Channel,” *IEEE Transactions on Vehicular Technology*, vol. 59, no. 1, pp. 63–74, Jan. 2010, doi: 10.1109/TVT.2009.2020427.
- [37] M. T. Alresheedi and J. M. H. Elmirghani, “Line strip multibeam spot diffusing optical wireless system employing beam delay and power adaptation with angle diversity detection,” in *2011 7th International*

- Wireless Communications and Mobile Computing Conference*, Jul. 2011, pp. 924–929. doi: 10.1109/IWCMC.2011.5982525.
- [38] M. T. Alresheedi and J. M. H. Elmirghani, “Performance Evaluation of 5 Gbit/s and 10 Gbit/s Mobile Optical Wireless Systems Employing Beam Angle and Power Adaptation with Diversity Receivers,” *IEEE Journal on Selected Areas in Communications*, vol. 29, no. 6, pp. 1328–1340, Jun. 2011, doi: 10.1109/JSAC.2011.110620.
- [39] Z. Chen, N. Serafimovski, and H. Haas, “Angle Diversity for an Indoor Cellular Visible Light Communication System,” in *2014 IEEE 79th Vehicular Technology Conference (VTC Spring)*, May 2014, pp. 1–5. doi: 10.1109/VTCSpring.2014.7022832.
- [40] R. K. Sharma, H. Kaushal, and P. K. Sharma, “Analysis of indoor FSO link under diffused channel topology,” in *International Conference on Computing, Communication & Automation (ICCCA2015)*, May 2015, pp. 1268–1272. doi: 10.1109/CCAA.2015.7148570.
- [41] A. T. Hussein and J. M. H. Elmirghani, “High-speed indoor visible light communication system employing laser diodes and angle diversity receivers,” in *2015 17th International Conference on Transparent Optical Networks (ICTON)*, Jul. 2015, pp. 1–6. doi: 10.1109/ICTON.2015.7193304.
- [42] J. Ding, C. L. I, and Z. Xu, “Indoor Optical Wireless Channel Characteristics With Distinct Source Radiation Patterns,” *IEEE Photonics Journal*, vol. 8, no. 1, pp. 1–15, Feb. 2016, doi: 10.1109/JPHOT.2015.2508420.
- [43] B. Mendoza, S. Rodríguez, R. Pérez-Jiménez, A. Ayala, and O. González, “Comparison of Three Non-Imaging Angle-Diversity Receivers as Input Sensors of Nodes for Indoor Infrared Wireless

- Sensor Networks: Theory and Simulation,” *Sensors*, vol. 16, no. 7, p. 1086, Jul. 2016, doi: 10.3390/s16071086.
- [44] R. ghahramani Negar Sendani, “Study the Effect of FOV in Visible Light Communication,” *International Research Journal of Engineering and Technology (IRJET)*, vol. 04, no. 10, pp. 759–763, Oct. 2017.
- [45] R. Sharma, M. Aggarwal, and S. Ahuja, “Channel Capacity and BER Estimation of Indoor Optical Wireless Communication System Under Receiver Mobility,” *Journal of Optical Communications*, vol. 39, no. 4, pp. 413–426, Oct. 2018, doi: 10.1515/joc-2016-0119.
- [46] O. Z. Aletri, M. T. Alresheedi, and J. M. H. Elmirghani, “Transmitter Diversity with Beam Steering,” in *2019 21st International Conference on Transparent Optical Networks (ICTON)*, Jul. 2019, pp. 1–5. doi: 10.1109/ICTON.2019.8840147.
- [47] M. K. Aljohani *et al.*, “NOMA Visible Light Communication System with Angle Diversity Receivers,” in *2020 22nd International Conference on Transparent Optical Networks (ICTON)*, Jul. 2020, pp. 1–5. doi: 10.1109/ICTON51198.2020.9203212.
- [48] M. E. Hosney, H. A. I. Selmy, and K. M. F. Elsayed, “Co-Channel Interference Reduction by Optimizing Field of View Angle of Angular Diversity Receiver in VLC Systems,” in *2020 22nd International Conference on Transparent Optical Networks (ICTON)*, Jul. 2020, pp. 1–4. doi: 10.1109/ICTON51198.2020.9203155.
- [49] M. Román Cañizares, P. Palacios Játiva, C. A. Azurdia-Meza, S. Montejo-Sánchez, and S. Céspedes, “Impact of diversity combining schemes in a multi-cell VLC system with angle diversity receivers,” *Photonic Network Communications*, vol. 43, no. 1, pp. 13–22, Feb.

2022, doi: 10.1007/s11107-022-00966-y.

- [50] J. C. Zwinkels and C. Canada, *Encyclopedia of Color Science and Technology*, no. January 2015. Berlin, Heidelberg: Springer Berlin Heidelberg, 2020. doi: 10.1007/978-3-642-27851-8.
- [51] P. N. Youssef, N. Sheibani, and D. M. Albert, “Retinal light toxicity,” *Eye*, vol. 25, no. 1, pp. 1–14, Jan. 2011, doi: 10.1038/eye.2010.149.
- [52] H. Haas, J. Elmirghani, and I. White, “Optical wireless communication,” *Philosophical Transactions of the Royal Society A: Mathematical, Physical and Engineering Sciences*, vol. 378, no. 2169, p. 20200051, Apr. 2020, doi: 10.1098/rsta.2020.0051.
- [53] D. K. Borah, A. C. Boucouvalas, C. C. Davis, S. Hranilovic, and K. Yiannopoulos, “A review of communication-oriented optical wireless systems,” *EURASIP Journal on Wireless Communications and Networking*, vol. 2012, no. 1, p. 91, Dec. 2012, doi: 10.1186/1687-1499-2012-91.
- [54] F. E. Alsaadi and J. M. H. Elmirghani, “Adaptive mobile multicarrier code division multiple access optical wireless systems employing a beam clustering method and diversity detection,” *IET Optoelectronics*, vol. 4, no. 3, pp. 95–112, Jun. 2010, doi: 10.1049/iet-opt.2009.0006.
- [55] M. Mukherjee, “Wireless communication-moving from RF to optical,” in *2016 3rd International Conference on Computing for Sustainable Global Development (INDIACom)*, Mar. 2016, pp. 788–795.
- [56] S. Qazi, “Challenges In Outdoor and Indoor Optical Wireless Communications,” in *International Conference on Wireless Networks, ICWN*, Jun. 2006, pp. 448–458.
- [57] Y. Su and T. Sato, “A key technology for standardizing outdoor optical

- wireless communications,” *ICT Express*, vol. 3, no. 2, pp. 62–66, Jun. 2017, doi: 10.1016/j.icte.2017.05.002.
- [58] G. J. Blinowski, “Practical Aspects of Physical and MAC Layer Security in Visible Light Communication Systems,” *International Journal of Electronics and Telecommunications*, vol. 62, no. 1, pp. 7–13, Mar. 2016, doi: 10.1515/eletel-2016-0001.
- [59] P. Djahani and J. M. Kahn, “Analysis of infrared wireless links employing multibeam transmitters and imaging diversity receivers,” *IEEE Transactions on Communications*, vol. 48, no. 12, pp. 2077–2088, Dec. 2000, doi: 10.1109/26.891218.
- [60] A. S. Hamza, J. S. Deogun, and D. R. Alexander, “Classification Framework for Free Space Optical Communication Links and Systems,” *IEEE Communications Surveys & Tutorials*, vol. 21, no. 2, pp. 1346–1382, Apr. 2019, doi: 10.1109/COMST.2018.2876805.
- [61] A. Shahriar, M. Chakraborty, S. Hossain, D. Halder, and N. B. Chowdhury, “Wireless infrared communication between two computers by MATLAB,” in *2014 9th International Forum on Strategic Technology (IFOST)*, Oct. 2014, pp. 60–64. doi: 10.1109/IFOST.2014.6991072.
- [62] D. O’Brien, S. Rajbhandari, and H. Chun, “Transmitter and receiver technologies for optical wireless,” *Philosophical Transactions of the Royal Society A: Mathematical, Physical and Engineering Sciences*, vol. 378, no. 2169, p. 20190182, Apr. 2020, doi: 10.1098/rsta.2019.0182.
- [63] A. S. Alhazmi, S. H. Mohamed, O. Z. Aletri, T. E. H. El-Gorashi, and J. M. H. Elmirghani, “Angle Diversity Trasmmitter For High Speed Data Center Uplink Communications,” in *2021 IEEE Conference on*

- Standards for Communications and Networking (CSCN)*, Dec. 2021, pp. 14–19. doi: 10.1109/CSCN53733.2021.9686098.
- [64] H. Elgala, R. Mesleh, and H. Haas, “Indoor optical wireless communication: potential and state-of-the-art,” *IEEE Communications Magazine*, vol. 49, no. 9, pp. 56–62, Sep. 2011, doi: 10.1109/MCOM.2011.6011734.
- [65] R. Green and M. Leeson, “The optical wireless channel,” in *Advanced Optical Wireless Communication Systems*, S. Arnon, J. Barry, G. Karagiannidis, R. Schober, and M. Uysal, Eds. Cambridge, United Kingdom: Cambridge University Press, 2012, pp. 240–272. doi: 10.1017/CBO9780511979187.010.
- [66] C. Singh, J. John, Y. N. Singh, and K. K. Tripathi, “A Review of Indoor Optical Wireless Systems,” *IETE Technical Review*, vol. 19, no. 1–2, pp. 3–17, Jan. 2002, doi: 10.1080/02564602.2002.11417006.
- [67] Z. Ghassemlooy and A. R. Hayes, “Indoor Optical Wireless Communication Systems – Part I: Review,” in *Quantum Beam Ltd. Review*, 2003, pp. 11–31.
- [68] L. Zeng *et al.*, “High data rate multiple input multiple output (MIMO) optical wireless communications using white led lighting,” *IEEE Journal on Selected Areas in Communications*, vol. 27, no. 9, pp. 1654–1662, Dec. 2009, doi: 10.1109/JSAC.2009.091215.
- [69] C. Jenila and R. K. Jeyachitra, “Green indoor optical wireless communication systems: Pathway towards pervasive deployment,” *Digital Communications and Networks*, vol. 7, no. 3, pp. 410–444, Aug. 2021, doi: 10.1016/j.dcan.2020.09.004.
- [70] C. Singh, J. John, Y. N. Singh, and K. K. Tripathi, “Indoor Optical Wireless Systems: Design Challenges, Mitigating Techniques and

- future Prospects,” *IETE Technical Review*, vol. 21, no. 2, pp. 101–117, Mar. 2004, doi: 10.1080/02564602.2004.11417136.
- [71] K.-P. Ho, “Compound parabolic concentrators for narrowband wireless infrared receivers,” *Optical Engineering*, vol. 34, no. 5, pp. 1385–1395, May 1995, doi: 10.1117/12.201664.
- [72] S. Rodríguez Pérez, B. Rodríguez Mendoza, R. Pérez Jiménez, O. González Hernández, and A. García-Viera Fernández, “Design considerations of conventional angle diversity receivers for indoor optical wireless communications,” *EURASIP Journal on Wireless Communications and Networking*, vol. 2013, no. 1, p. 221, Dec. 2013, doi: 10.1186/1687-1499-2013-221.
- [73] M. T. Alresheedi and J. M. H. Elmirghani, “Hologram selection in realistic indoor optical wireless systems with angle diversity receivers,” *Journal of Optical Communications and Networking*, vol. 7, no. 8, pp. 797–813, Aug. 2015, doi: 10.1364/JOCN.7.000797.
- [74] R. Hou, Y. Chen, J. Wu, and H. Zhang, “A Brief Survey of Optical Wireless Communication,” in *Proceedings of the 13th Australasian Symposium on Parallel and Distributed Computing (AusPDC 2015)*, Jan. 2015, vol. 163, pp. 41–50.
- [75] M. Alhartomi, “Collaborative Optical Wireless Communication Systems,” Ph.D. dissertation, University of Leeds, England, 2015.
- [76] A. E. Ibhaze, P. E. Orukpe, and F. O. Edeko, “High capacity data rate system: Review of visible light communications technology,” *Journal of Electronic Science and Technology*, vol. 18, no. 3, p. 100055, Sep. 2020, doi: 10.1016/j.jnlest.2020.100055.
- [77] C. T. Manimegalai, S. Gauni, N. Raghavan, and T. R. Rao, “Investigations on suitable modulation techniques for visible light

- communications,” in *2017 International Conference on Wireless Communications, Signal Processing and Networking (WiSPNET)*, Mar. 2017, pp. 1818–1822. doi: 10.1109/WiSPNET.2017.8300075.
- [78] A. Chaaban, Z. Rezki, and M.-S. Alouini, “On the Capacity of Intensity-Modulation Direct-Detection Gaussian Optical Wireless Communication Channels: A Tutorial,” *IEEE Communications Surveys & Tutorials*, vol. 24, no. 1, pp. 455–491, Nov. 2020, doi: 10.1109/COMST.2021.3120087.
- [79] K. Smitha, A. Sivabalan, and J. John, “Estimation of Channel Impulse Response Using Modified Ceiling Bounce Model in Non-Directed Indoor Optical Wireless Systems,” *Wireless Personal Communications*, vol. 45, no. 1, pp. 1–10, Apr. 2008, doi: 10.1007/s11277-007-9368-y.
- [80] K. Wang, A. Nirmalathas, C. Lim, and E. Skafidas, “Impact of background light induced shot noise in high-speed full-duplex indoor optical wireless communication systems,” *Optics Express*, vol. 19, no. 22, p. 21321, Oct. 2011, doi: 10.1364/OE.19.021321.
- [81] D. J. T. Heatley, D. R. Wisely, I. Neild, and P. Cochrane, “Optical wireless: the story so far,” *IEEE Communications Magazine*, vol. 36, no. 12, pp. 72–74, 79–82, Dec. 1998, doi: 10.1109/35.735881.
- [82] J. M. Kahn and J. R. Barry, “Wireless infrared communications,” *Proceedings of the IEEE*, vol. 85, no. 2, pp. 265–298, Feb. 1997, doi: 10.1109/5.554222.
- [83] R. Atpadkar, T. Gholve, and S. Gajare, “Performance Analysis Of Ambient Noise On Diffused Optical Wireless Communication Systems In Indoor Environments,” *International Journal of Engineering Research & Technology (IJERT)*, vol. 2, no. 6, pp. 496–

500, Jun. 2013.

- [84] M. A. Alhartomi, F. E. Alsaadi, and J. M. H. Elmirghani, “Collaborative multibeam transmitter and imaging receiver in realistic environment,” in *2015 17th International Conference on Transparent Optical Networks (ICTON)*, Jul. 2015, pp. 1–6. doi: 10.1109/ICTON.2015.7193305.
- [85] F. Alsaadi and J. H. Elmirghani, “Adaptive mobile spot diffusing angle diversity MC-CDMA optical wireless system in a real indoor environment,” *IEEE Transactions on Wireless Communications*, vol. 8, no. 5, pp. 2187–2192, May 2009, doi: 10.1109/TWC.2009.070857.
- [86] F. E. Alsaadi and J. M. H. Elmirghani, “Adaptive multibeam clustering angle diversity optical wireless system,” in *2010 14th Conference on Optical Network Design and Modeling (ONDM)*, Feb. 2010, pp. 1–6. doi: 10.1109/ONDM.2010.5431583.
- [87] F. R. Gfeller and U. Bapst, “Wireless in-house data communication via diffuse infrared radiation,” *Proceedings of the IEEE*, vol. 67, no. 11, pp. 1474–1486, Nov. 1979, doi: 10.1109/PROC.1979.11508.
- [88] J. R. Barry, J. M. Kahn, W. J. Krause, E. A. Lee, and D. G. Messerschmitt, “Simulation of multipath impulse response for indoor wireless optical channels,” *IEEE Journal on Selected Areas in Communications*, vol. 11, no. 3, pp. 367–379, Apr. 1993, doi: 10.1109/49.219552.
- [89] A. G. Al-Ghamdi, “Optical wireless multibeam transmitter with line strip, diamond, and uniform geometries,” *Optical Engineering*, vol. 42, no. 11, p. 3295, Nov. 2003, doi: 10.1117/1.1615992.
- [90] F. Miramirkhani, “A Path Loss Model for Link Budget Analysis of Indoor Visible Light Communications,” *Electrica*, vol. 21, no. 2, pp.

242–249, May 2021, doi: 10.5152/electrica.2021.20072.

- [91] F. Alsaadi, M. Nikkar, and J. Elmirghani, “Adaptive mobile optical wireless systems employing a beam clustering method, diversity detection, and relay nodes,” *IEEE Transactions on Communications*, vol. 58, no. 3, pp. 869–879, Mar. 2010, doi: 10.1109/TCOMM.2010.03.080361.
- [92] J. M. H. Elmirghani, R. A. Cryan, and K. L. Sterckx, “Sensitivity assessment of a three-segment pyramidal fly-eye detector in a semidisperse optical wireless communication link,” *IEE Proceedings - Optoelectronics*, vol. 147, no. 4, pp. 286–294, Aug. 2000, doi: 10.1049/ip-opt:20000609.
- [93] A. G. Al-Ghamdi and J. M. H. Elmirghani, “Performance comparison of LSMS and conventional diffuse and hybrid optical wireless techniques in a real indoor environment,” *IEE Proceedings - Optoelectronics*, vol. 152, no. 4, p. 230, Aug. 2005, doi: 10.1049/ip-opt:20045009.
- [94] M. A. Alhartomi, F. E. Alsaadi, and J. M. H. Elmirghani, “Mobile optical wireless system using fast beam Angle, delay and power adaptation with angle diversity receivers,” in *2012 14th International Conference on Transparent Optical Networks (ICTON)*, Jul. 2012, pp. 1–5. doi: 10.1109/ICTON.2012.6253885.
- [95] S. H. Younus, A. A. Al-Hameed, A. T. Hussein, M. T. Alresheedi, and J. M. H. Elmirghani, “Parallel Data Transmission in Indoor Visible Light Communication Systems,” *IEEE Access*, vol. 7, pp. 1126–1138, Jan. 2019, doi: 10.1109/ACCESS.2018.2886398.
- [96] J. Krupka, P. Kamiński, R. Kozłowski, B. Surma, A. Dierlamm, and M. Kwestarz, “Dielectric properties of semi-insulating silicon at

microwave frequencies,” *Applied Physics Letters*, vol. 107, no. 8, p. 082105, Aug. 2015, doi: 10.1063/1.4929503.

- [97] “T. INSTRUMENTS, Ultra-Low Noise, HighSpeed Operational Amplifier <http://www.ti.com/lit/ds/symlink/lmh6629.pdf>, access 20 November 2019. (2018)],,,”
Http://Www.Ti.Com/Lit/Ds/Symlink/Lmh6629.Pdf.
- [98] M. E. Hosney, H. A. I. Selmy, and K. M. F. Elsayed, “Co-Channel Interference Management in Visible Light Communication,” in *2020 29th Wireless and Optical Communications Conference (WOCC)*, May 2020, pp. 1–4. doi: 10.1109/WOCC48579.2020.9114914.
- [99] S. Hranilovic and F. R. Kschischang, “Optical intensity-modulated direct detection channels: signal space and lattice codes,” *IEEE Transactions on Information Theory*, vol. 49, no. 6, pp. 1385–1399, Jun. 2003, doi: 10.1109/TIT.2003.811928.

Publishing

- [1] Roua Muwafaq Younus, Safwan Hafeedh Younus, and Mahmud. A. Al Zubaidy, “Performance Enhancement of the OWC by Optimizing the FOV of the Optical RX,” *International Journal of Microwave and Optical Technology (IJMOT)*, Vol.17, no.4, July 2022. (Published).
- [2] Roua Muwafaq Younus, Mahmud. A. Al Zubaidy, and Safwan Hafeedh Younus, “Angle Diversity RX for Indoor Optical Wireless Communication Systems,” in *4th International Conference On Advanced Science and Engineering (4th ICOASE)*, and will be published in (IEEE Xplore Digital Library). (Accepted).

الخلاصة

نظرًا لتطور التقنيات والتطبيقات الحديثة التي تتطلب نقلًا عاليًا للبيانات ، فقد نشأت الحاجة إلى الانتقال إلى الطيف عالي التردد مثل الإتصالات اللاسلكية الضوئية. توفر هذه الإتصالات مزايا عديده ، مثل النطاق الترددي غير المحدود وغير المرخص. يحتوي نظام الإتصالات اللاسلكي الضوئي ، مثل الترددات اللاسلكية، على العديد من العيوب مثل ضوضاء الخلفية (التي تتضمن الضوضاء الطبيعية والإصطناعية على حد سواء) ، ومسار الانتشار المتعدد الذي ينتج عنه إنتشار الإشارة و تداخلًا بين الرموز (ISI) وكلها تؤدي إلى انخفاض في مستوى أداء النظام.

اقترحت هذه الرسالة نظامين لمعالجة هذه المشكلات وإنشاء نظام لاسلكي داخلي فعال. النظام الأول المقترح يغير مجال الرؤية (FOV) للكاشف الفردي لتقليل تأثير الانتشار متعدد المسيرات وضوضاء الخلفية. يتم التحقق من ذلك عن طريق كتابة كود برمجي في برنامج MATLAB. حيث يتم عرض تأثيرات كل تعديل وكل تعديل يحتوي على 100 موقع إستقبال عشوائي ، يهدف نظامنا إلى تحسين أداء النظام مع الحفاظ على سهولة إستخدامه وتكلفته غير المكلفة. يتم إستخدام دالة التوزيع التراكمي (CDF) لعرض مدى جودة عمل النظام المقترح. تجدر الإشارة إلى أنه مع تضيق مجال الرؤية ، نحصل على نتائج أفضل ، حيث يقلل من تأثير ISI عن طريق تقليل انتشار التأخير من 2.297 نانوثانية لـ $FOV = 90$ درجة ، والتي تغطي 60 ٪ من مواقع المستلم بالكامل ، إلى 0.637 نانوثانية عند ضبط FOV على 10° وتحسن نسبة الإشارة إلى الضوضاء (S/N). تبلغ S/N 4.91 ديسيبل لمجال رؤية 90 درجة تغطي 80٪ من إجمالي المواقع ، و 16 ديسيبل لمجال رؤية يبلغ 10 درجات.

بينما يستخدم النهج الثاني أجهزة كشف متعددة بدلاً من واحد لمستقبل تنوع الزوايا (ADR) لتقليل تأثير ضوضاء الخلفية. يؤدي هذا إلى زيادة S/N من 9.4 ديسيبل لنظام الانتشار التقليدي (CDS) إلى 3.677 ديسيبل عند استخدام ADR عندما يكون المستلم في الزاوية البعيدة للغرفة. يتم إجراء تحسين زاوية الارتفاع ، كما يتم استخدام مجال الرؤية الضيقة لمزيد من التحسين في أداء النظام. 232 ميگاهرتز هو عرض النطاق الترددي للقناة 3 ديسيبل (3-dB BW) الذي يمكن الوصول إليه عند استخدام ADR . إجراء تعديلات في كود الكاشف الفردي ليكون أكثر ملاءمة للنظام المقترح الثاني وإضافة بعض التعقيد إلى بنية النظام يأتي بالتضحية من أجل تحسين أداء النظام عند استخدام ADR .



وزارة التعليم العالي والبحث العلمي

جامعة نينوى

كلية هندسة الالكترونيات

قسم هندسة الاتصالات

التحقيق في تحسين أداء الإتصال اللاسلكي البصري

رسالة تقدمت بها

رؤى موفق يونس

إلى

مجلس كلية هندسة الالكترونيات

جامعة نينوى

كجزء من متطلبات نيل شهادة الماجستير

في

هندسة الاتصالات

بإشراف

أ.م.د. محمود احمد محمود الزبيدي

د.صفوان حفيظ يونس



وزارة التعليم العالي والبحث العلمي
جامعة نينوى
كلية هندسة الالكترونيات
قسم هندسة الاتصالات

التحقيق في تحسين أداء الإتصال اللاسلكي البصري

رؤى موفق يونس

رسالة ماجستير علوم في هندسة الاتصالات

بإشراف

أ.م.د. محمود احمد محمود الزبيدي

د.صفوان حفيظ يونس